Particle Image Velocimetry, Accuracy of the Method with Particular Reference to Turbulent Flows

Charlotte Elgaard Dam

Ph. D.
University of Edinburgh
1995

Abstract

In this thesis we present theoretical predictions of the error relative to sampling area when estimating turbulent parameters, such as the mean and rms value, from Particle Image Velocimetry (PIV) measurements. These results emulate similar time-domain analyses for Laser Doppler Velocimetry (LDA). Homogeneous and shear turbulent flow regimes are considered.

The key analysis parameter, the mean square error, leads to an expression for the normalized standard error. The correlation coefficient is a prominent factor in the result and the error is evaluated for three distinct forms of this in one and two dimensions.

Furthermore the results are simplified to yield general expressions for the error relative to sampling area given the integral lengthscale and rms turbulence level of the flow. The results are applicable, not only to PIV, but to any measurement method that produces results on a spatial domain.

Results from PIV measurements of homogeneous isotropic grid turbulence in air and water are presented. The usefulness of the technique is discussed in terms of; the shape of the curve of the correlation coefficient, the resolution obtained relative to the turbulent lengthscales and coherent structures in the flow, and are, whenever possible, compared to LDA measurements. One of the measurements have been performed as a time series, and a number of vector and velocity plots show both the temporal and spatial development of the flow.

In order to verify the theoretical predictions, several measurements of the same flow has been collected and a range of subareas of the total accumulated area has been defined. The relevant parameters and normalized standard error have been calculated for each of the sets of subareas. Given the required factors can be provided, we find the experimental and theoretical results in good agreement, proving this to be a useful result.

Acknowledgements

Thanks must first of all go to my supervisor Professor Clive Greated and Dantec Electronics, especially Christian Caspersen, for inspiration, encouragement and support over the years I have worked on this thesis.

I should also very much like to thank my collegues at University of Edinburgh for their competent, and often patient, help and assistance. First I want to thank Denise McCluskey whose expertise and friendship has been truly invaluable, and many thanks also go to Frank Morris, David Skyner, Callum Gray, Francis Barnes and Tom Bruce. I should also like to thank Jerry Westerweel at University of Delft.

My warmest thanks go to all my friends who made my stay in Edinburgh such a special time, most of all to Cathe Redford.

Finally I should like to extend my gratitude and love to my husband Mads, who, over these years, has shown great endurance and devotion.

I was financially supported with grants from Dantec Electronics, the Danish Research Academy and Lauritzen Fonden.

Declaration

This thesis has been composed by myself and, except where stated, the work contained is my own.

Charlotte Elgaard Dam

Charlotte Elgaard Dam

Contents

Chapter 1

Introduction

The primary objective of the work presented in this thesis has been to investigate the performance of the flow measurement technique, Particle Image Velocimetry (PIV), when applied to turbulent flows.

Two distinct approaches are presented; firstly the accuracy with which certain turbulent parameters can be calculated for results, such as these from PIV, which are given on a spatial domain, has been established. Secondly, the technique has been used to measure turbulent flows in air and water. The results have been analysed, compared with expected values and results from measurements of the same flow situation using other techniques. These measurement results have above all formed the base for experimental verification of the theoretical results.

Turbulent flows are very complex and thus challenging to measure. The general turbulence concepts are discussed in chapter 2, along with homogeneous isotropic and shear turbulence, both of these in terms of randomness and coherent structures.

Particle Image Velocimetry is a non-intrusive, full field, laser measurement technique, that gives simultaneous velocity information at several points over a plane in the flow. The technique is presented and discussed in chapter 3, as are the various methodologies employed to realize the technique.

In chapter 4 we present the fully automated PIV analysis system developed at The University of Edinburgh. This is the analysis system that has been used for all the mentioned results.

The theoretical analysis and estimates of the normalized standard error relative to sampling area are given in chapter 5. Here are presented formulae for the error when calculating the mean velocity, correlation function, mean square and rms over finite sets of the velocity maps gained from the PIV measurements described in chapter 6. The experimental results are analysed and discussed in terms of length scales, coherent structures and the resolution obtained, and they have been used as a means to corroborate the above-theoretical predictions.

Chapter 2

Turbulence concepts.

As many naturally occuring flows are turbulent in nature, it is a widely studied field of fluid dynamics. It is, however, complicated if not impossible to give an exact formal definition of what constitutes a turbulent flow. A common preconseption about turbulent flows is that they are totally random flows, this is not the case, the random features may be dominant but organized motion is also present. Hinze [39] states:

> Turbulent fluid motion is an irregular condition of the flow in which the various quantities show a random variation with time and space coordinates, so that statistically distinct average values can be discerned.

From this we can conclude that although turbulent flows may be predominantly random in nature, it is possible to describe, though not define, the flow from statistical values. Several examples of different types of turbulent flows exist.

2.1 Homogeneous isotropic turbulence.

Homogeneous isotropic turbulence where the statistical properties are rotational and translational invariant, is not an in reality existing type of flow. Considerable turbulence research is centered round this type since it is a turbulent flow that is relatively easy to describe theoretically. Furthermore it is possible to generate a close approximation to homogeneous isotropic turbulence in the laboratory. The most common way of producing this type of flow is by generating grid turbulence, the fluid is led through a periodic grid and at a certain distance behind the grid the resulting flow is homogeneous and near isotropic turbulence, Corrsin [19].

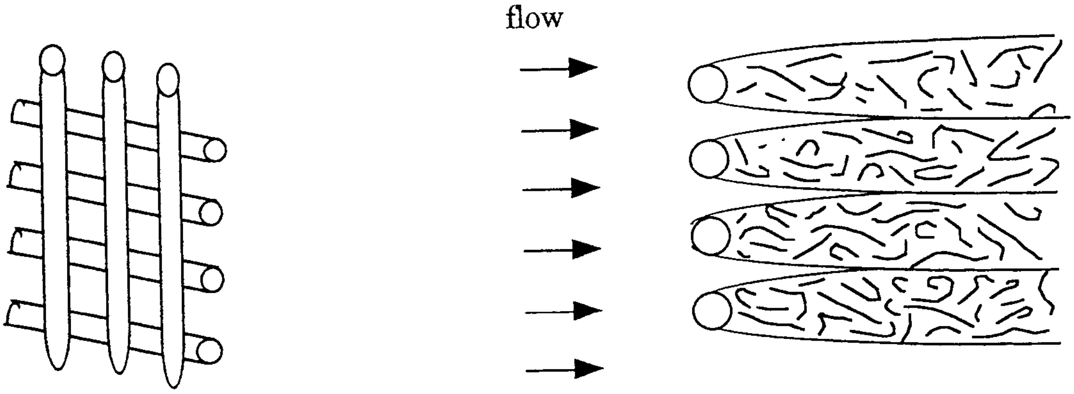

Figure 2.2. Grid generated homogeneous isotropic turbulence.

Immediately behind the grid there is very strong turbulent energy and this carries on as the flow moves away from the grid and develops, the flow then smoothes out and become increasingly isotropic. Generally a distance of 20 x M, where M is the grid spacing, is the distance that must be reached from the grid before fully developed homogenous near-isotropic grid turbulence is present. In the final stages furthest away from the grid the flow decays gradually.

2.2 Shear turbulence.

Shear turbulence is a naturally occuring turbulent flow type. These flows cannot be described by simple means, but vary in time and space in the manner described above. Free turbulent shear flow, are turbulent flows that exist far from boundaries, an example is the turbulent wake after a cylinder.
A cylinder is placed in a non-turbulent flow far from boundaries. A turbulent wake is produced after the cylinder increasing in width with distance downstream from the cylinder. There is an interface between the turbulent wake and the non-turbulent surrounding flow, this takes the form of a sharp edge but with an irregular shape. At any fixed point in the flow there will be random oscillations between turbulent and non-turbulent flow, the fraction of time that the flow is turbulent is called the intermittency factor γ, such that at the centre of the wake $\gamma = 1$, outside the wake $\gamma = 0$. Generally over a significant part of the wake, the intermittency factor will be less than 1, turbulent and non-turbulent flow alternate.

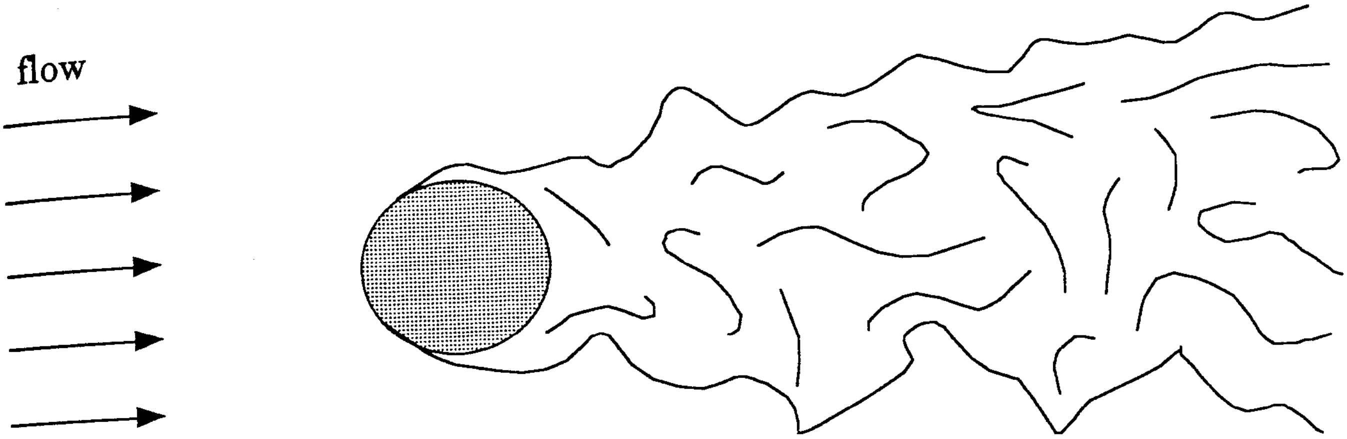

Figure 2.2. The turbulent wake.

2.3 The energy cascade and lenght scales.

The energy cascade is a process in turbulent flows whereby energy is transferred from large scales to eddies to smaller scales. In, for example, grid-generated turbulence, energy is fed into the flow as the turbulence is generated by the grid; this energy goes mainly into producing the larger eddies. From the larger eddies smaller eddies are generated by inertial effects, and from these still smaller ones and the whole process continues until the length scales are so small that the effect of viscosity becomes more important and finally takes over. From theoretical investigations of the process a range of length scales have been defined related to the various factors of the energy cascade.

It is as the turbulence is generated that the largest structures are found in the flow. One important length scale is to a certain extend a measure of the length over which some kind of correlation persists in the flow; it is called the macro or integral length scale L, and is defined as follows:

$$L = \int_0^\infty f(x)dx$$

where $f(x)$ is the longitudinal correlation function. It is equally common to define the integral length scale L in terms of the transverse correlationfunction $g(x)$. The integral length scale can be taken as a measure of the largest eddies in the flow, not necessarily, however, where the majority of the energy of the flow is contained. The largest eddies have a non-negligible part of the total energy, but the eddies that have the maximum kinetic energy correspond to a length scale smaller than L.

The range of eddies that makes the main contribution to the total energy is called the range of energy containing eddies. There is a lenghtscale associated with the range of energy containing eddies, this is also called a macroscale and denoted by l_e; l_e is smaller than L but of the same order of magnitude. A suitable choice for l_e where grid turbulence is concerned is the grid spacing M.

As the energy cascade proceeds and smaller and smaller eddies are generated, the dissipation by viscous effects increases. There are two main length scales, called microscales, associated with this range, namely, Taylor,s microscale and the Kolmogorov microscale.

Taylor's micro or dissipation length scale λ is defined in terms of the one-dimensional correlation functions.

$$\frac{1}{\lambda_g^2} = -1/2 \left[\frac{\partial^2 g(x)}{\partial x^2}\right]_{x=0}$$

$$\frac{1}{\lambda_f^2} = -\left[\frac{\partial^2 f(x)}{\partial x^2}\right]_{x=0}$$

The value of λ can be determined by assuming that the correlation functions are parabolic at the origin, [75]. Alternative methods for measuring this parameter is suggested by Hinze [39].

In relation to the energy cascade it can be shown that the dissipation of kinetic energy into heat by viscous effects are governed by the factor $\overline{[\partial u/\partial x]^2_{x=0}}$; this is again directly proportional to the second derrivative of the one-dimensional correlation function used above. Hence, the dissipation or Taylor microscale λ may be taken as a measure of the average dimension of the eddies that are mainly responsible for dissipation.

The transfer of energy to yet smaller eddies and increasing dissipation continues until we reach the smallest dissipative eddies. The length scale associated with these eddies is called the Kolmogorov microscale η and is defined in terms of the kinematic viscosity ν and the rate of turbulent energy dissipation ϵ.

$$\eta = \left(\frac{\nu^3}{\epsilon}\right)^{1/4}$$

Together with Taylor's microscale, the Kolmogorov microscale marks the region of the flow where the viscous effects are very strong.

Relations between the different length scales makes it possible to estimate one from the other. We can define two Reynold numbers, one relating to the macroscale, or range of energy containing eddies, and one relating to the microscale or range of maximum dissipation.

$$Re_\lambda = \frac{u'\lambda_g}{\nu} \quad Re_l = \frac{u'l_e}{\nu}$$

where $u' = \sqrt{u^2}$ is the intensity of the turbulence. From Hinze [39] we find that the total dissipation can be expressed as:

$$\epsilon = 15\nu\frac{u'}{\lambda^2}$$

This is equal to the work done by the energy containing eddies, which again is the energy supplied to the smaller eddies. This can be expressed as:

$$\epsilon = A\frac{u'^3}{l_e}$$

where A is a constant of order unity. From this we can deduce the relations:

$$\begin{aligned}
Re_l &= \frac{A}{15}Re_\lambda^2 \\
\frac{\lambda}{\eta} &= 15^{1/4}Re_\lambda^{1/2} \\
\frac{l_e}{\lambda} &= \frac{A}{15}Re_\lambda \\
\frac{l_e}{\eta} &= 15^{-3/4}ARe_\lambda^{3/2}
\end{aligned}$$

2.4 Vorticity.

The vorticity of a flow is defined as:

$$\vec{\omega} = curl\ \vec{u}$$

For a two-dimensional flow it is the third component of the curl of the velocity that is considered, the third component of the vorticity.

$$\omega_z = \frac{\partial v}{\partial x} - \frac{\partial u}{\partial y}$$

where $\underline{r} = (x, y, z)$ and $\underline{u} = (u, v, w)$.

The vorticity corresponds to the rotation of the flow, but indicates not only rotation but also the sense of rotation. Flows without vorticity are called irrotational flows.

2.5 Coherent structures.

As was mentined above there has been a tendency to link turbulent flows with randomness. Recently, however, a different view has emerged. Theories suggesting some kind of ordered motion in turbulent flows have been put forward, and the larger scale structures have become known as coherent structures. Coherent structures play an important role in the transport of heat, mass and momentum through the fluid. There are at the moment still discussions as to the exact definition of coherent structures and some of the prevailing trends are presented below.

Hussain[44,45] defines coherent structures as follows: "A coherent structure is a connected turbulent fluid mass with an instantaneously phase-correlated vorticity over its spatial extend". By this is meant a kind of ordered underlying vorticity in the flow, and the flow can be divided into coherent structures and incoherent turbulence. As an example for free shear flows the coherent structures have a size comparable to the lengthscale l_e for the flow. Coherent structures of a size comparable to Taylors microscale are called coherent substructures. Although this picture might concur with an intuitive picture of coherent structures, it has to be noted that coherent structures defined as above cannot always be visualized.

A technique that relies more on individually visually identifiable structures is put forward by Mumford [62,63]. Here the correlation function and velocity of the flow is used to identify a range of different eddy type structures. In a flow measurement result a flow pattern is selected by inspection. A form of pattern recognition method is then employed to modify the initially guessed pattern to the actual pattern and the correct position and shape of the structure can be determined.

Instead of dividing the flow area into coherent structures and incoherent turbulence Hunt et.al. [42] proposed a different view, in which the flow plane is divided into regions associated with certain average properties of the flow. The different zones are defined as follows:

Eddy (E) zones: Areas where the irrotational straining is small compared with the vorticity, furthermore the pressure field inside the body of the zone should be independent from the field outside the zone. These are, as we have suggested vortical regions.

Convergence (C) zones: These are defined as regions where there is irrotational straining motion and where there is strong convergence or divergence of streamlines, hence the irrotational straining must be large compared with the vorticity. Convergence zones tend to be round or square in shape and they usually have a stagnation point in the zone.

Streaming (S) zones: In these zones the flow is fast; they are 'highways' for fluid or particles transported with the flow. A criteria is that the velocity in the zone must be higher than some threshold value. The streaming zones tends to be elongated zones leading to convergence regions.

There are several other applications of coherent structure theories, most similar to or based on one of the above[41, 25, 64].

Chapter 3

PIV: a non-intrusive, full-field laser measurement technique.

Perhaps one of the simplest ways of observing flows is to introduce tracers or similar small particles into the flow and simply follow how these move with the flow. There are a number of measurement techniques based on this relatively simple scheme, particle tracing and streak photography to mention just two. These basically flow visualization techniques give valuable information about the qualitative nature of the flow and have been used extensively.

Quantitative flow measuring techniques,such as pitot-static tubes, measuring mainly the velocity of the flow, reveal other aspects of the flow situation. But can attenuate the flow as probes have to be introduces directly into the flow itself. An optical technique such as LDA, Laser Doppler Velocimetry, which also relies on small particles being introduced into the flow, is non-intrusive and gives very accurate measurements of the velocity at a given point in the flow.

PIV, Particle Image velocimetry, is a full-field, non-intrusive laser measurement technique. When applying PIV to a flow situation it is possible to gain simultaneous velocity information at a number of points over a plane in the flow field, which in itself serves as a type of visualization of the flow. Since PIV is an optical technique, it is not necessary to introduce probes into the flow, however, optical access is required. All of these aspects of PIV make it a very valuable flow measurement tool, which complements the other well known techniques mentioned above.

PIV is a later development of a technique initially called Scattered Light Speckle, SLS, first developed as a means to measuring deformation of solid bodies. Later LSV, Laser Speckle Velocimetry, and a separate mode of this PIV, was introduced. The difference between the speckle and PIV modes will be discussed in later sections.

Over the later years PIV has rapidly developed into a very sophisticated flow measurement technique, with a variety of recording and analysis methods. PIV have been applied, very successfully, to a wide range of flow situations [6,10, 33, 51, 54, 60, 70, 83]

A historical review and account of the develpment of the technique can be found in [22].

3.1 PIV flow recording.

As mentioned above the basic principles of recording PIV measurements involves:

- Seeding the flow with suitable scatterers.
- Illuminating a slice of the flow with a sheet of laser light. Then pulse or chop the light beam to create a series of illuminations of the flow plane.
- Record a multiple exposure record of the flow on photographic film or digital CCD camera.

When a plane in the flow is illuminated the scatterers will show up as bright spots; this is what is recorded onto the film. Assuming the particles follow the flow accurately, the recording sequence is as follows. The flow plane is illuminated for a short period of time, the light beam is chopped and the particles move with the flow (the velocity is assumed constant for the relative short period of time between illuminations), and the flow is illuminated again. When this sequence is recorded onto for, example, photographic film it will look in priciple as shown in Figure 3.1.

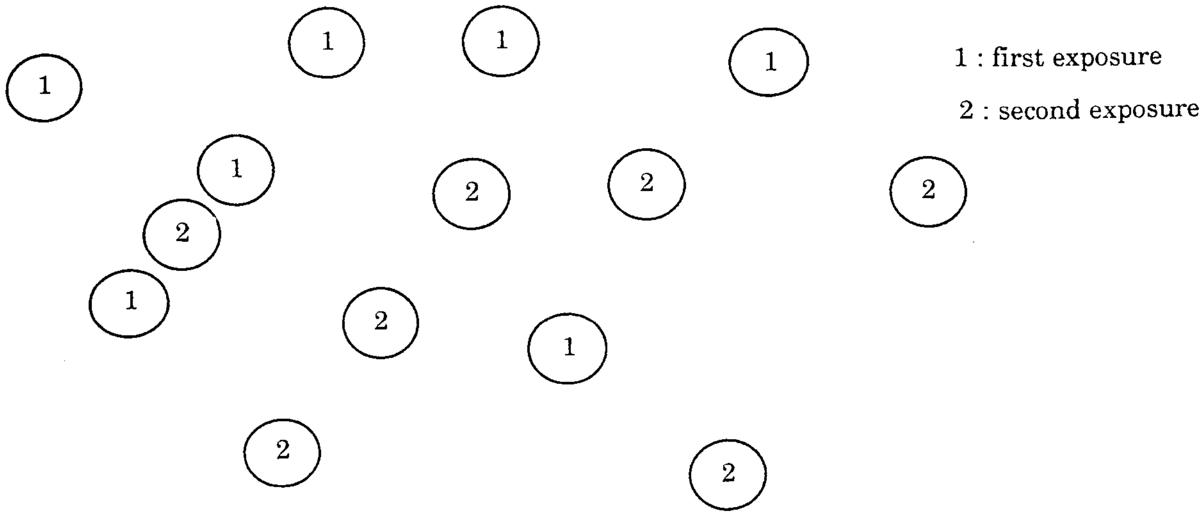

Figure 3.1 A small section (enlarged) of a PIV recording.

It is thus clear, that given the time separation between the illuminations, it is in principle possible to measure the distance between the particle images, relate this to the actual displacement in the flow and calculated the velocity at that point, *distance & time* $\Rightarrow$ *velocity* .

$$v = \frac{d_s}{MT}$$

Where: v is the velocity of the fluid element containing the particles.
d_s is the separation of the particle images.
M is the magnification of the recording.
T is the time between consecutive illuminations.

It is uncommon to analyse the PIV recording by directly measuring the separation of the particle images on the film, more sophisticated analysis methods have been developed and will be discussed in detail later.

3.2 Seeding the flow.

Finding suitable scatterers is an important, and often non-trivial part of PIV measurements. It is in the nature of the recording method that a number of requirements for the scatterers can be put forward:

- The scatterers should preferably be spherical.
- They should follow the flow accurately, be neutrally bouyant.
- They should scatter light well.

There can be a conflict between the last two requirements. How efficiently the particles scatter light is dependent upon their size, the larger particles, in general, scatter more light than smaller ones. On the other hand, if the particles are too large they cannot be assumed to follow the flow accurately, small scale features are lost and errors are introduced into the velocity measurement. Adrian and Yao [7,8] have studied the scattering power of seed materials and concluded that for PIV the optimum particle diameter was $d_p \simeq 10\mu m$ for polystyrene particles in water, and $d_p \simeq 5\mu m$ for oil or glass particles in air. The most common seeding materials are [24]:

atomized oil	$1 - 5\mu m$	: low velocity air flows
titanium dioxide	$0.5 - 5\mu m$	: airflows
latex particles	$0.25 - 5\mu m$	: airflows and waterflows
conifer pollen	$70\mu m$	: waterflows

Consistent with the requirement of being able to accurately follow the flow, the scattering particles should be chosen as large as possible to make the most effective use of the illuminating light.

We have mentioned that two distinct modes exist, LSV and PIV. Generally it can be said that LSV has high seeding concentrations and produces a speckle pattern in the image plane. PIV has low seeding densities and individual particle images are resolved in the image plane. The analysis of the two modes are similar. The concentration of the seeding particles in the flow is generally chosen with a view to optimizing the subsequent analysis of the recorded negative. Most analysis methods employs an approach where the actual analysis of the PIV recording is performed over small sub-areas of the total recorded area, these small areas being called interrogation areas. Keane and adrian [47,48,49] suggests that the number of particle image pairs within the interrogation region should exceed 10-20. Furthermore the source density $S.D.$ is defined as [8]:

$$S.D. = \frac{C \Delta z \pi d_b^2}{4M^2}$$

where:

C is the volume concentration of the particles.

Δz is the thickness of the light sheet.

d_b is the diameter of the interrogation area.

M is the magnification of the recording system.

In order to observe individual particle images in the recording, we must have $S.D. < 1$. If $S.D.$ is significantly larger than one, then speckle patterns are observed.

It can often be difficult to adjust or measure the seeding concentration in order to achieve the optimum settings listed above. It is thus more common to choose Δz, M and d_b accordingly to get the correct number of particle images in the interrogation area.

3.3 Illumination methods.

Although PIV measurements can, and have been, performed using white light, the overwhelming majority are performed using coherent light, lasers. Continuous wave lasers or pulsed lasers are employed, resulting in three main methods.

3.3.1 Illumination with pulsed lasers.

As PIV is employed to investigate flows with increasingly higher speeds and possibly seeded with very small particles (in the order of $\sim 1\mu m$), pulsed lasers are really the only type of laser powerful enough to give the required intensity of illumination. The optical arrangement is shown in Figure 3.2.

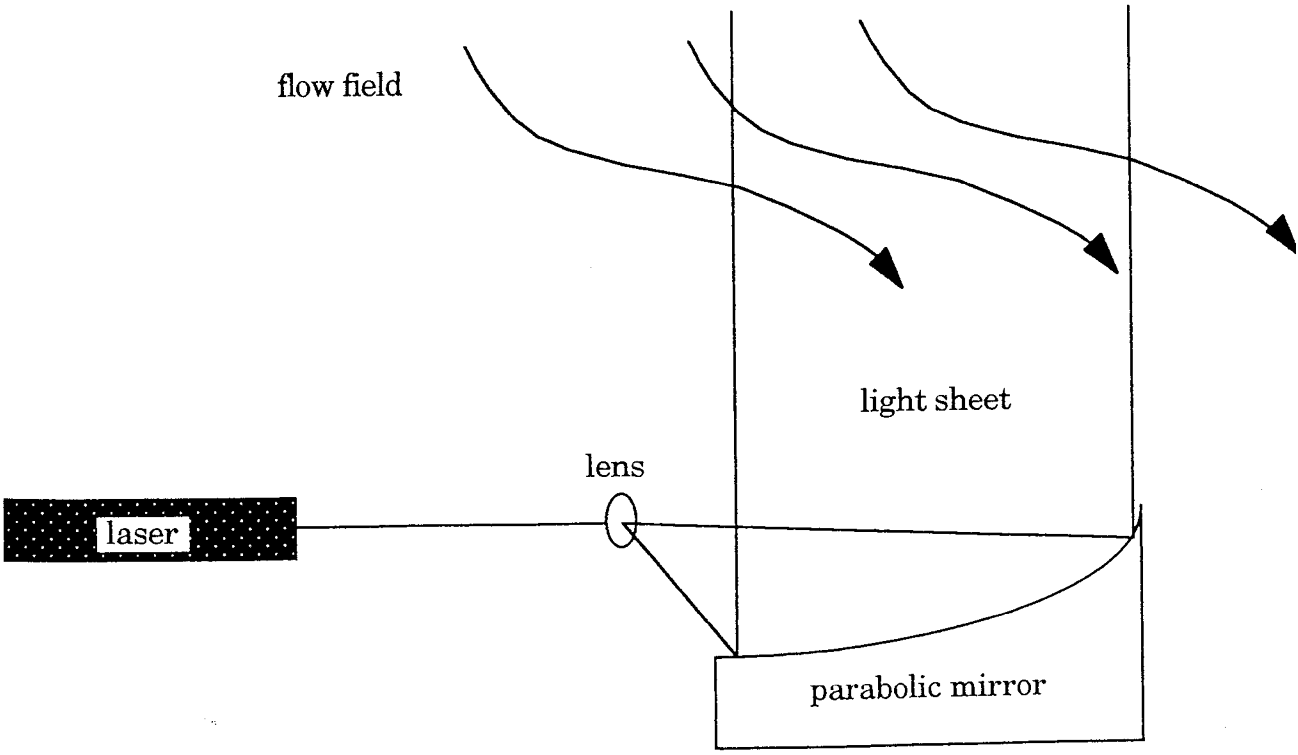

Figure 3.2 Pulsed laser (or expanded beam) illumination method.

The pulsed laser beam is expanded into a sheet using a cylindrical lens, collimated and deflected into the flow using a parabolic mirror.

Stringent safety measures are essential when working with pulsed lasers, as these can be extremely dangerous. Other disadvantages includes the limited range of pulse separations available for pulsed lasers. This problem can be overcome by using two pulsed lasers in parallel; such an arrangement is the most powerful PIV illumination method available, but is also very expensive.

3.3.2 Expanded beam method.

This is the original illumination method using continous wave CW lasers. The optical arrangement is similar to the one shown for pulsed lasers in Figure 3.2. The laser beam is expanded into a sheet using a cylindrical lens and deflected via a parabolic mirror into the flow. The laser beam is chopped mechanically or electro-optically to form pulses and the subsequent illuminations of the flow. A wide range of illumination intervals is thus available. This is a frequently used and compared to the pulsed laser method,it is relatively inexpensive but only applicable to low speed flows and flows where the region of interest is small. This is due to the fact that the modulation of the beam results in only part of the laser light being used to illuminate the flow, resulting in inefficient use of the laser light, and since the light intensity is crucial to many, especially high speed, applications, other methods must be employed to ensure results.

3.3.3 The scanning beam method.

This is an alternative illumination method using CW lasers [34]. The optical arrangement for this method is shown in Figure 3.3.

A laser beam is directed onto a rapidly rotating mirror which has several facets. Successive facets in turn reflect the beam through an arc of $4\pi/N$, where N is the number of facets on the mirror. The beam is then deflected onto a parabolic mirror and the result is a linear scan through the flow, the scan being so fast that it resembles a pseudo light sheet. The scan is repeated every $T = 1/(FN)$ seconds , where F is the rotation frequency of the miror.

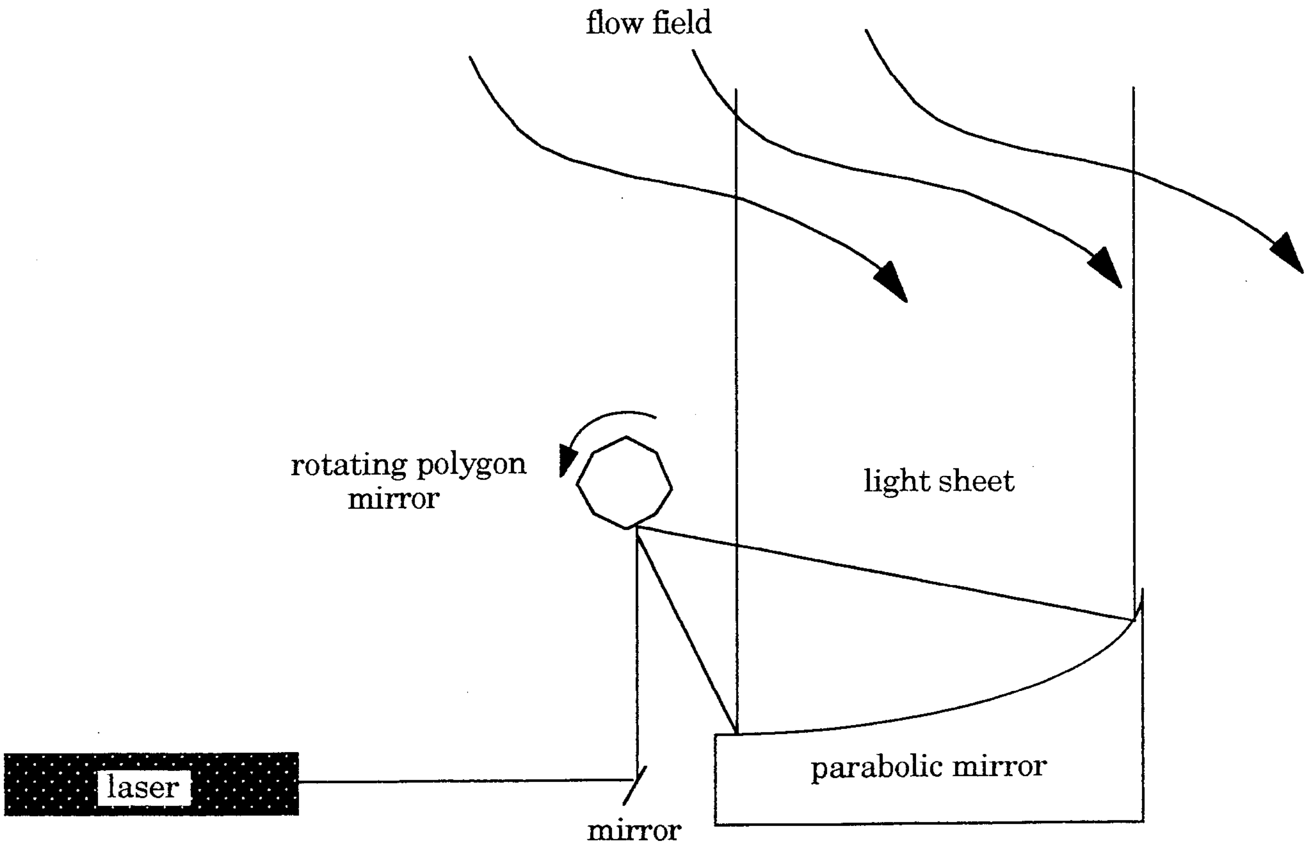

Figure 3.3. The scanning beam illumination method.

As the beam scans the flow, a scatterer in the flow is illuminated as the beam passes, then moves with the flow and is illuminated again with the repeating of the scan after time T. The resulting picture is almost identical to the one produced using the expanded beam method, a multiple exposure of the particles.

One of the main advantages with this illumination technique is the efficient use of the laser light, all the light being concentrated in the beam rather than spread out over the whole flow area. The time interval between illuminations is readily changed by adjusting the frequency of the rotating mirror.

As all of these methods are essentially two-dimensional techniques that are in most circumstances employed to investigate flows that are to some extend three-dimensional, an error are introduced. If the particles have a large component of velocity across the light sheet they can move outwith the sheet between illuminations. This fact also causes the phenomena of parallax described below.

If the flow has significant three-dimensionality, it is recommended that the time between exposures T and the thickness of the light sheet Δz be chosen [47] such that:

$$\frac{v_z T}{\Delta z} \leq 0.25$$

Where v_z is the velocity component perpendicular to the illuminating light sheet.

3.4 Photographic and video recording.

The PIV measurements are recorded using a camera with photographic film, or lately video cameras. The camera is mounted parallel to the illuminating light sheet. Assuming that the particles do not move during the time they are illuminated, the image diameter on the recorded film is [7]:

$$d_i = \left(M^2 d_p^2 + d_{spot}^2 + d_r^2\right)^{1/2}$$

d_p is the seeding particle diameter.
M is the magnification.
$d_{spot} = 2.44(1 + M) f_{no} \lambda_l$ where f_{no} is the f-number of the recording lens and λ_l is the wavelength of the illuminating light.
d_r is the grain size of the film.

It is of course essential that the images are resolved by the recording medium. This has so far been the major problem when using digital techniques such as CCD cameras, their resolution have been too poor. This is an area, however, that is under rapid development and digital techniques are increasingly being used for PIV measurements [83].

3.4.1 Dynamic range.

The dynamic range is a measure of the range of velocities it is possible to capture for a given experimental PIV set-up. In the image plane the separation of subsequent particle images are given by:

$$d_s = MvT$$

The lower limit on the dynamic range is dependent on the image diameter. It is desirable to have the two particle images distinct, that is not overlapping. This implies that the minimum image separation is equal to the image diameter d_i.

$$\underline{\Rightarrow} \; Mv_{min}T = d_{s_{min}} = d_i$$

The upper limit on the image separation is dependent on the diameter of the interrogation area d_b. It is recommended that the relationship should be [47]:

$$Mv_{max}T = d_{s_{max}} \leq 0.25d_b$$

So the limits on the dynamic range are:

$$v_{min} = \frac{d_{s_{min}}}{TM} = \frac{d_i}{MT} \quad v_{max} = \frac{d_{s_{max}}}{TM} \leq \frac{0.25d_b}{MT}$$

3.4.2 Parallax.

Parallax is the name of the error that is introduced when recording an object through a lens and the object has a component of velocity parallel to the axis of the camera. The magnitude of the error is directly related to the distance of the viewed object from the axis of the lens. The error is introduced in the two-dimensional image recording on the film, and shows up as an added in-plane velocity, most prominent at the edges of the recording plane.

3.5 PIV analysis techniques.

In the following we will assume that the PIV measurement is recorded using photographic film, the analysis of digital PIV images being described in [83]. The PIV negative displays particle images that are double or multiple exposures of scatterers in the flow. There are several methods that can be employed to extract the velocity information from these negatives. Generally the negative is divided into smaller interrogation areas and the average velocity within that area is established.

3.5.1 Particle tracking.

Particle tracking can be employed when the seeding density is very low and the individual particle images clearly resolved. The interrogation region is captured on a CCD camera, digitized and the position of the individual particle images established. A particle tracking algorithm is employed to determine which particles corresponds to doublets or multiple exposures of a given particle. The average velocity over the interrogation region can then be calculated.

3.5.2 The Youngs fringes method.

Over a small area of the PIV negative, where the velocity can be assumed constant, the particle images consist of two (or multiple) sets of particle images each displaced by an amount corresponding to the velocity of the flow at that point. The most reliable way of determining the displacement, and thus the velocity, of the particle images is to calculate the autocorrelation of the images over the small area. The autocorrelation from a double exposure measurement will look, in principle, as the one shown in Figure 3.4, with a large central self-correlation peak and two displacement peaks.

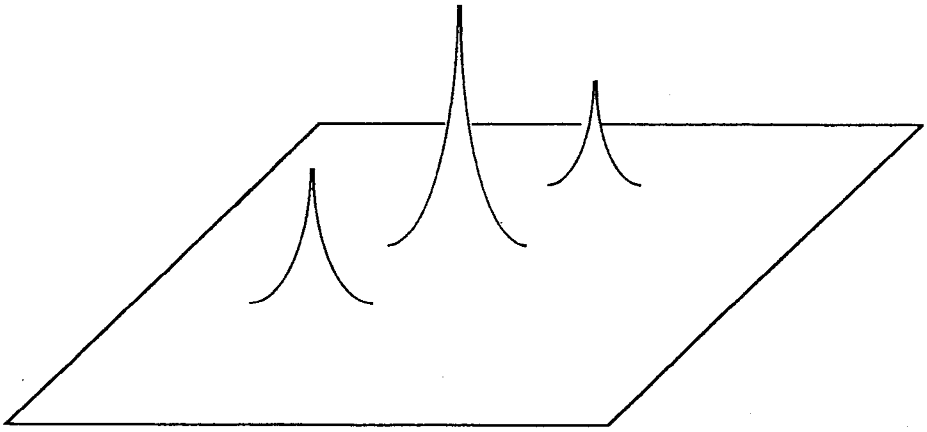

Figure 3.4 The autocorrelation plane of a double exposure PIV measurement.

The reason for there being two displacement peaks is due to the fact that there is a 180^o ambiguity in photographically recorded PIV measurements. For two particle images it is impossible to discern, without prior knowledge, which belongs to the first and which to the second exposure, as illustrated in figure 3.5.

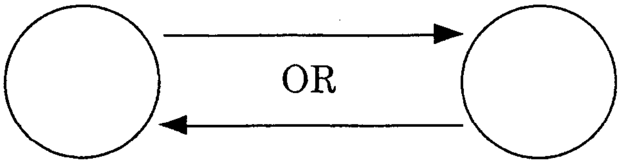

Figure 3.5 Directional ambiguity in PIV.

For Youngs fringes analysis a small area of the negative is probed with a laser beam, the intensity pattern is passed through a Fourier transforming lens and the resulting Youngs fringes pattern is captured on a CCD camera and digitized. The spacing of the Youngs fringes is inversely proportional to the separation of the particle images, and the orientation of the fringes perpendicular to the direction of motion of the particles. The separation and direction of motion of the particles could thus be evaluated directly from the Youngs fringes, but more accurate results can be obtained employing the autocorrelation, or Wiener-Khinchin theorem, which states that the autocorrelation of a signal is the Fourier transform of the power spectrum of that signal.

The Youngs fringe pattern described above is the power spectrum of the intensity distribution of the particle images in the interrogation region. The Youngs fringes can be captured on a CCD camera, digitized and a Fourier transform performed on them, resulting in the autocorrelation function of the distribution of particle images in the interrogation region. The central self-correlation peak is removed and the displacement of the particle images determined from the secondary displacement peaks. The Youngs fringes analysis is illustrated in figure 3.6.

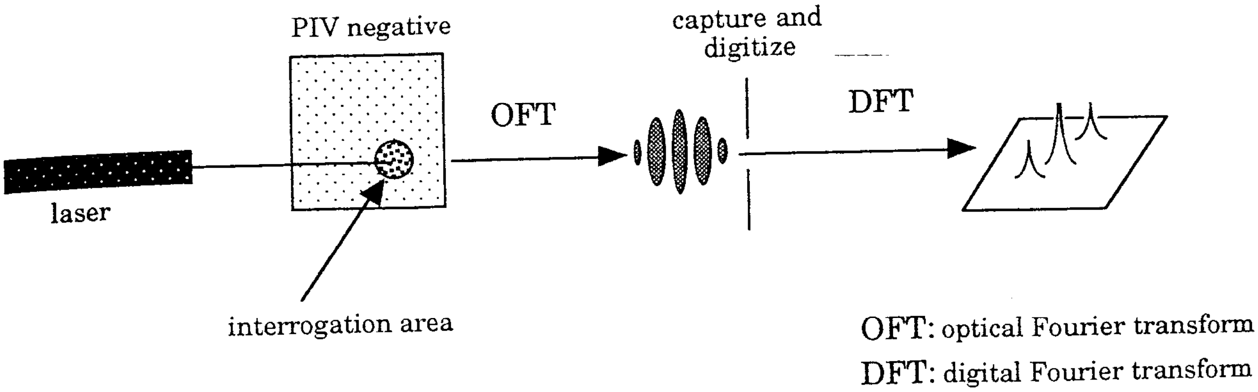

Figure 3.6. The Youngs fringes analysis method.

3.5.3 2D autocorrelation method.

Instead of accquiring the power spectrum via an optical Fourier transform, as in the Youngs fringes method, this can be achieved computationally. As for the Youngs fringes method, a small area of the negative is probed using a collimated beam of light. In this case it is not necessary that the beam is coherent. The intensity pattern of the particle images in the interrogation area is captured and digitized using a CCD camera and a frame grabber. After collection, the captured data is transformed to the power spectrum using a complex two-dimensional Fourier transform. The autocorrelation is obtained as above by performing a Fourier transform on the power spectrum and displacement of the particle images is found as for the Youngs fringes method. The 2D autocrrelation method is illustrated in figure 3.7.

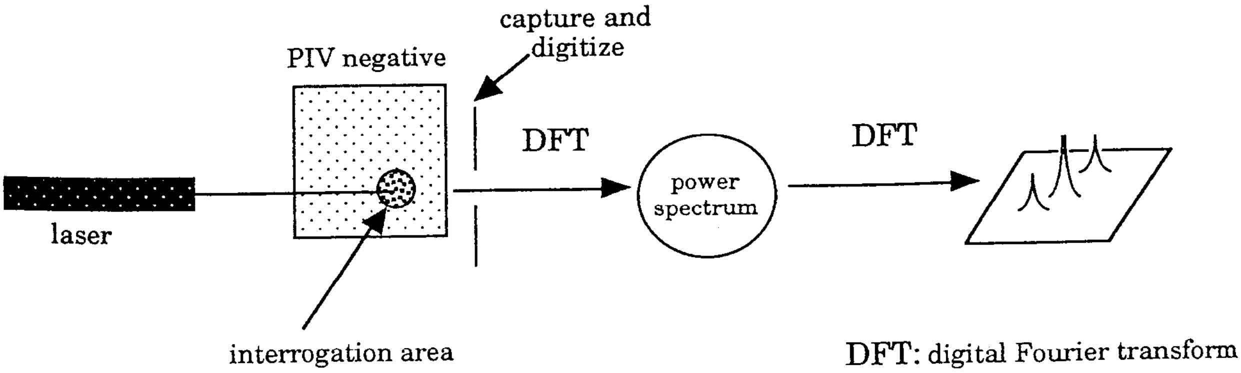

Figure 3.7. The 2D autocorrelation analysis method.

Orthogonal compression and other methods are often used to make the 2D autocorrelation method more effective.

3.6 Other aspects of PIV.

3.6.1 Directional ambiguity in PIV.

As mentioned above, there is , inherent in the PIV technique, a 180° ambiguity. Various methods can be employed to solve this dilemma, these methods are described in the internal report on ways to resolve directional ambiguity in PIV measurements, included as appendix A.

3.6.2 3D techniques.

PIV is no longer limited to two dimensions; 3D techniques are being developed and amongst these two main trends are emerging.

Stereoscopic techniques.

In principle this technique is similar to the way human vision works. The method utilizes the fact that the out-of-plane component of velocity, if it is not exactly on the optical axis of the camera, adds an error to the measurement of in-plane velocities. The stereoscopic method uses two cameras to image the flow from two distinct directions. There are thus two, instead of one, negatives for each measurement. The three components of the velocity are found from their projections on the photographic film and the characteristics of the stereoscopic set-up.

Holographic 3D PIV.

The seeded flow is traversed by a parallel beam travelling through the field to the holographic plate. A small part of the light is diffused by the scatterers in the flow and combined with the non-diffused light giving rise to the hologram. By placing the hologram in the same laser beam, the image of the field can be found and the 3D position of the particles determined. For double pulsed PIV, two sets of images are formed, the holograms being superimposed. If the particles have been moving between exposures, as we assume they have with constant velocity, the two resulting positions can be found and the velocity determined. No simple automatic way of analysing the holograms have yet been devised constituting a major problem with this technique.

Chapter 4

The fully automated PIV analysis system.

The analysis system used for analysis of all results described later in this thesis, the analysis system at the Fluid Dynamics Unit University of Edinburgh, has evolved over a number of years. The research in the group has covered a wide range of topics in the field of PIV and the automated analysis system has been developed through the demands of the varied applications.

The system is based on the Youngs fringes principle of analysis described in Chapter 3. The system is fully automated in the sense that after mounting and alignment of the negative, no further action need be taken; the negative is analysed automatically.

There have been few changes in the basic principles of the analysis system from the first version. There has, however, been significant upgrading of the equipment and software, resulting in increased speed of the analysis process. The automated PIV system is showed schematically in Figure 4.1.

A laser beam from a 1mW Helium-Neon laser is passed through a spatial filter producing a beam with a Gaussian profile. The beam is then collimated and passed through a 1mm aperture. The laser beam probes a small area of the negative, the interrogation area. It is possible to produce a beam with different widths or other outlines than circular, but for the applications presented here, the circular beam with 1mm diameter is used. The intensity of the interrogating beam can be adjusted, this is useful as the contrast of the different PIV negatives may vary and it is desirable to change the intensity of the interrogating beam in order to produce optimum clarity of the fringes.

The negative is mounted on a micro-translational stage so that it is the negative

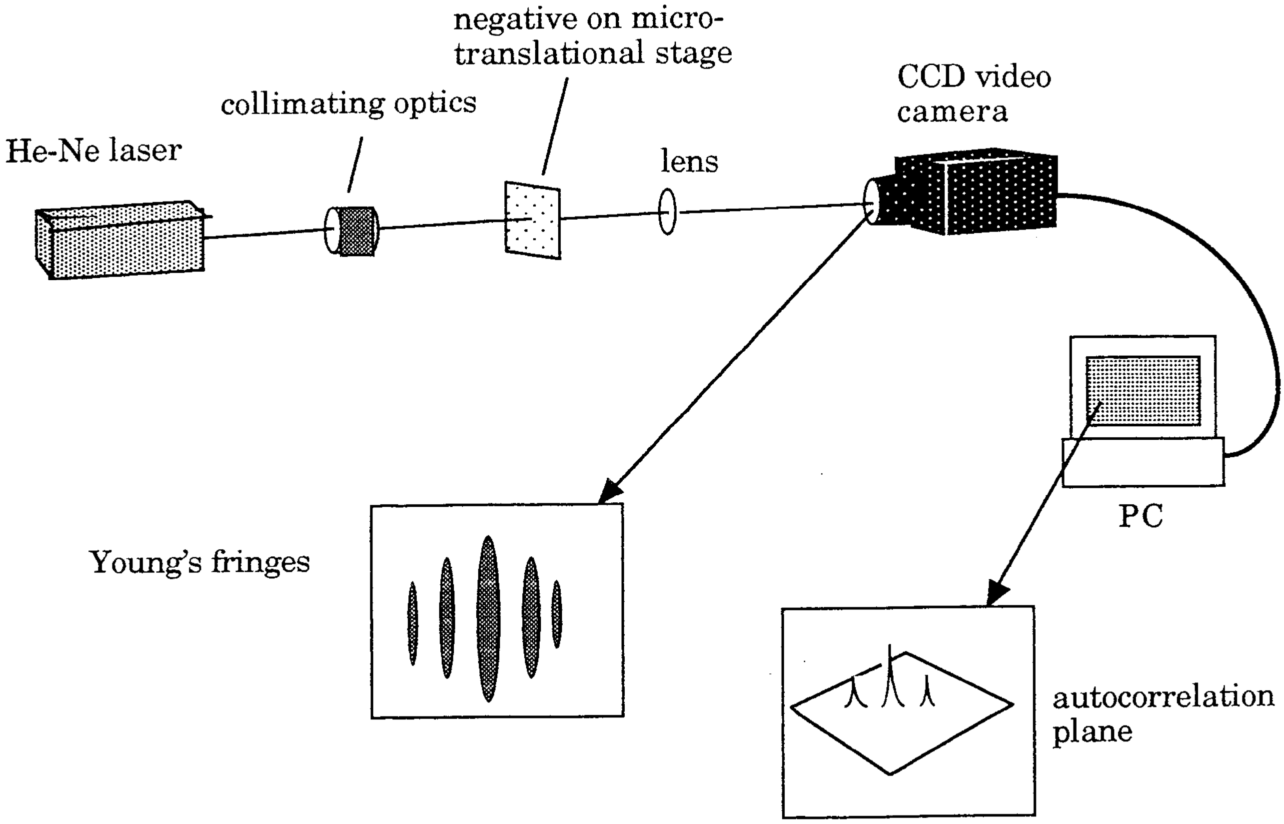

Figure 4.1: Schematic diagram of the automated PIV analysis system at The University of Edinburgh.

that moves in front of the laser. The size of the steps, in which the negative is analysed, can be selected and also whether the negative should be analysed on a regular square grid, or on a circular grid.

When the laser beam probes the negative the Youngs fringes are formed in the back focal plane of a lens and captured using a CCD camera. The fringe information is sent to a microcomputer via a framestore that digitises the image. Once the image is captured and digitised the microtranslational stage can move the negative to the next position. Processing the digitised power spectrum using a Fast Fourier Transform, produces the auto-correlation of the particle images in the interrogation region. Figure 4.2 shows a typical Youngs fringes power spectrum and its corresponding auto-correlation plane (the central self-correlation peak has been removed).

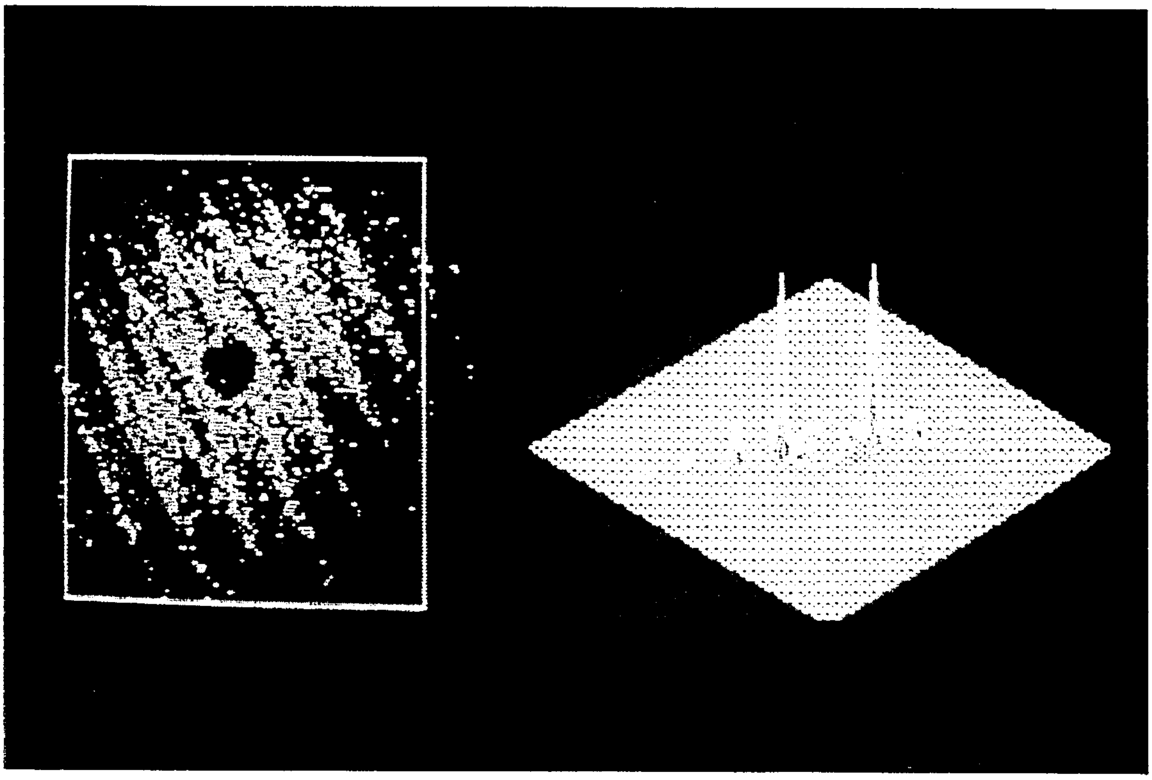

Figure 4.2: Typical Youngs fringes and corresponding auto-correlation plane.

When the actual time separation between illumination of the flow plane and the magnification has been supplied, it is possible to relate the separation of the particle images calculated from the fringes to the actual flowplane velocity in m/s. The visibility of the fringes (often used for filtering purposes), is calculated as the ratio of the volume of the displacement peaks to the volume of the surrounding

noise.
The whole process is repeated until the entire selected field on the negative is analysed.

It is often required to perform some kind of post-processing on the raw velocity data. Filtering is often employed to 'edit' the velocity data. Naturally it can be necessary to remove any single, obviously erroneous, values, bearing in mind that this analysis technique will produce a velocity vector value at every point, regardless of the presence of fringes or not. Other full-field transformations may be performed such as shifting the velocity values by addition or subtraction of a constant velocity value. This is necessary when employing the image shifting technique. Further information concerning the flow field such as vorticity o flow field statistics can also be extracted using post-processing software [24]

Chapter 5

Accuracy of flow parameters obtained from PIV measurements

We are interested in establishing a formula for the error involved when calculating the mean velocity, correlation function, mean square and rms over finite sets of the results of PIV measurements. We have emmulated work done for LDA measurements [23,26,27,]. The statistical evaluations are based on work presented by Bendat and Piersol in their book 'measurement and analysis of random data'[16], but the results have been transposed to a spatial as opposed to temporal domain, which involves new definitions of statistical functions, furthermore the results have been extended to 2D.

5.1 Preliminaries

The standard PIV measurement result takes the form of a two-dimensional velocity map, that is a set of the form $\{x, y, u(x, y), v(x, y)\}$, basically a finite set of discrete velocity values on a spatial domain.

We will for the time being assume that we have sufficient points in the set for it to be reasonable to assume a continous record for the purpose of integration.

When we calculate turbulent parameters from the PIV record we sample in either one or two dimensions, that is either over rows (or columns), or over areas of the resulting vector velocity map. In order to derive the form of the error involved when estimating the above parameters over finite samples on a spatial domain we have to redefine the statistical quantities, ergodicity and stationarity on the same domain.

Definition: Spatial stationarity.
For a random process or ensemble of sample functions $\{u(\underline{x})\}$ we define the mean value $\mu_u(\underline{x})$ and the correlationfunction $R_u(\underline{x}, \underline{x}+\underline{r})$ as follows,

$$\mu_u(x_1, y_1) = \lim_{K\to\infty} \frac{1}{K} \sum_{k=0}^{K} u_k(x_1, y_1)$$

$$R_u(x_1, y_1, x_1 + r_1, y_1 + r_2) = \lim_{K\to\infty} u_k(x_1, y_1) u_k(x_1 + r_1, y_1 + r_2)$$

This is the mean and correlationfunction computed over various samples $u_1(x_1, x_2), u_2(x_1, y_1), \ldots, u_K(x_1, y_1)$. For stationarity we require that these do not vary according to starting place (x_1, y_1), but only for R on distance $\underline{r}$.

$$\mu_u(x_1, y_1) = \mu_u$$

$$R_u(x_1, y_1, x_1 + r_1, y_1 + r_2) = R_u(r_1, r_2)$$

This imposes the criteria of homogeneity on the flow record and hence the flow. In the following we will consider homogeneous flows with a stationary flow record and return to the non-stationary case later.

Definition: Ergodic random process on a spatial domain.
Consider the k^{th} sample function for the random process $\{u(\underline{x})\}$. This could be chosen as one or several complete rows (or columns) or areas of the PIV record, or it can be chosen as the entire record letting another measurement record be another sample. For the chosen k^{th} sample, the mean value $\mu_u(k)$ and the correlationfunction $R_u(\underline{r}, k)$ are given by:

$$\mu_u(k) = \lim_{N_1\to\infty} \frac{1}{N_1} \int_0^{N_1} u_k(x) dx$$

$$R_u(r, k) = \lim_{N_1\to\infty} \frac{1}{N_1} \int_0^{N_1} u_k(x, y) u_k(x + r, y) dx$$

in 1D (over one or several rows).

$$\mu_u(k) = \lim_{N_1\to\infty} \lim_{N_2\to\infty} \frac{1}{N_1} \frac{1}{N_2} \int_0^{N_1} \int_0^{N_2} u_k(x, y) dy dx$$

$$R_u(r_1, r_2, k) = \lim_{N_1 \to \infty} \lim_{N_2 \to \infty} \frac{1}{N_1} \frac{1}{N_2} \int_0^{N_1} \int_0^{N_2} u_k(x, y) u_k(x + r_1, y + r_2) dy dx$$

in 2D (over areas $N_1 \times N_2$ of the map).

For ergodicity in the spatial domain we require that μ_u and R_u as defined above does not differ when computed over different sample functions, and that they are equal to the ensemble values.

$$\mu_u(k) = \mu_u$$

$$R_u(\underline{r}, k) = R_u(\underline{r})$$

The error we will be considering stems from estimating a parameter such as the mean velocity over finite samples, to this purpose we consider *the mean square error* or MSE, defined as the expected value of the square of the deviation of the estimate from the true value. Say we want to estimate the parameter Φ, where Φ is the true value of the parameter and $\hat{\Phi}$ is an estimate of Φ obtained from a measurement on a finite interval, we then find:

$$MSE = E[(\hat{\Phi} - \Phi)^2] = E[(\hat{\Phi} - E[\hat{\Phi}])^2] + E[(E[\hat{\Phi}] - \Phi)^2]$$

We find that the MSE of the estimate of the parameter Φ is equal to the variance of the estimate plus a bias factor $b^2[\hat{\Phi}]$.

$$var[\hat{\Phi}] = E[(\hat{\Phi} - E[\hat{\Phi}])^2] = E[\hat{\phi}^2] - E^2[\hat{\Phi}]$$

$$b^2[\hat{\Phi}] = E[(E[\hat{\Phi}] - \Phi)^2]$$

Leading to :

$$MSE = var[\hat{\Phi}] + b^2[\hat{\Phi}]$$

Note that if the expected value of the estimate of the parameter is equal to the true value of the parameter we have what we call an unbiased estimate, and the MSE is equal just to the variance of the estimate.

5.2 Mean velocity estimates.

5.2.1 2D estimates.

We have a sample velocity record of a homogenoues flow. The sample mean velocity value calculated over an area of the flowmap $N_1 \times N_2$, can be estimated as

$$\hat{\mu}_u = \frac{1}{N_1}\frac{1}{N_2}\int_0^{N_1}\int_0^{N_2} u(x,y)dydx$$

Where the true mean is $\mu_u = E[u(x,y)]$.
The expected value of the estimate $\hat{\mu}_u$ is

$$E[\hat{\mu}_u] = \frac{1}{N_1}\frac{1}{N_2}\int_0^{N_1}\int_0^{N_2} E[u(x,y)]dydx = \mu_u$$

showing this to be an unbiased estimate. Thus we find the mean square error to be

$$MSE = var[\hat{\mu}_u] = E[(\hat{\mu}_u - \mu_u)^2] = E[\hat{\mu}_u^2] - \mu_u^2 \tag{5.1}$$

Define the 2D correlationfunction R_u for $\underline{r} = (r_1, r_2)$and $\underline{x} = (x, y)$ as follows

$$\begin{aligned} R_u(r_1,r_2) &= \overline{u(x,y)u(x+r_1,y+r_2)} \\ \Rightarrow R_u(\underline{r}-\underline{x}) &= \overline{u(x,y)u(r_1,r_2)} \\ &= E[u(x,y)u(r_1,r_2)] \end{aligned}$$

From this we find the covariance C_u

$$\begin{aligned} C_u(\underline{r}) &= R_u(\underline{r}) - \mu_u^2 \\ \Rightarrow C_u(\underline{r}-\underline{x}) &= R_u(\underline{r}-\underline{x}) - \mu_u^2 \\ &= E[u(x,y)u(r_1,r_2)] - \mu_u^2 \end{aligned}$$

The normalized version of the covariance is called the corelation coefficient K_u.

$$\begin{aligned} K_u(\underline{r}) &= \frac{C_u(\underline{r})}{\overline{(u(\underline{r}) - \mu_u)^2}} \\ &= \frac{C_u(\underline{r})}{\sigma_u^2} \end{aligned}$$

where σ_u^2 is the variance of the sampled values.
Note that $K_u(0,0) = 1$ and that $K_u(\underline{r}) \to \infty$ as $\underline{r} \to \infty$.

We return to the calculation of the mean square error for mean velocity estimates over a finite sampling area $N_1 \times N_2$.

$$
\begin{aligned}
MSE &= var[\hat{\mu}_u] = E[\hat{\mu}_u^2] - \mu_u^2 \\
&= \frac{1}{N_1^2}\frac{1}{N_2^2}\int_0^{N_1}\int_0^{N_2}\int_0^{N_1}\int_0^{N_2} E[u(r,s)u(k,t)]dtdkdsdr - \mu_u^2 \\
&= \frac{1}{N_1^2}\frac{1}{N_2^2}\int_0^{N_1}\int_0^{N_2}\int_0^{N_1}\int_0^{N_2} \left(E[u(r,s)u(k,t)] - \mu_u^2\right) dtdkdsdr \\
&= \frac{1}{N_1^2}\frac{1}{N_2^2}\int_0^{N_1}\int_0^{N_2}\int_0^{N_1}\int_0^{N_2} C_u(k-r,t-s)dtdkdsdr \\
&= \frac{\sigma_u^2}{N_1^2 N_2^2}\int_0^{N_1}\int_0^{N_2}\int_{\eta=-r}^{N_1-r}\int_{\nu=-s}^{N_2-s} K_u(k-r,t-s)dtdkdsdr \\
&= \frac{\sigma_u^2}{N_1^2 N_2^2}\int_0^{N_1} dr \int_0^{N_2} ds \int_{-r}^{N_1-r} d\eta \int_{-s}^{N_2-s} K_u(\eta,\nu)d\nu \\
&= \frac{\sigma_u^2}{N_1^2 N_2^2}\int_0^{N_1} dr \int_{-r}^{N_1-r} d\eta \int_0^{N_2} ds \int_{-s}^{N_2-s} K_u(\eta,\nu)d\nu \\
&= \frac{\sigma_u^2}{N_1^2 N_2^2}\int_{-N_1}^{N_1} d\eta \int_0^{N_1-|\eta|} dr \int_{-N_2}^{N_2} ds \int_0^{N_2-|\nu|} K_u(\eta,\nu)d\nu \\
&= \frac{\sigma_u^2}{N_1^2 N_2^2}\int_{-N_1}^{N_1} d\eta \int_{-N_2}^{N_2} d\nu \int_0^{N_1-|\eta|} dr \int_0^{N_2-|\nu|} K_u(\eta,\nu)ds \\
&= \frac{\sigma_u^2}{N_1^2 N_2^2}\int_{-N_1}^{N_1} d\eta \int_{-N_2}^{N_2} (N_1-|\eta|)(N_2-|\nu|)K_u(\eta,\nu)d\nu
\end{aligned}
$$

In the above we have made use of the substitution $\eta = k - r$ and $\nu = t - s$, and the change of order of integration illustrated in Figure 5.1 below.
Thus for a finite sampling area of $N_1 \times N_2$ we find for the estimate of the velocity that the mean square error is:

$$
MSE = \frac{\sigma_u^2}{N_1 N_2}\int_{-N_1}^{N_1}\int_{-N_2}^{N_2}\left(1 - \frac{|\eta|}{N_1}\right)\left(1 - \frac{|\nu|}{N_2}\right) K_u(\eta,\nu)d\nu d\eta \qquad (5.2)
$$

The above expression is valid for all sampling areas. If however we consider very short averaging areas, the correlation coefficient is approximately unity and we find:

$$
MSE = \frac{\sigma_u^2}{N_1 N_2}\int_{-N_1}^{N_1}\int_{-N_2}^{N_2}\left(1 - \frac{|\eta|}{N_1}\right)\left(1 - \frac{|\nu|}{N_2}\right) K_u(\eta,\nu)d\nu d\eta
$$

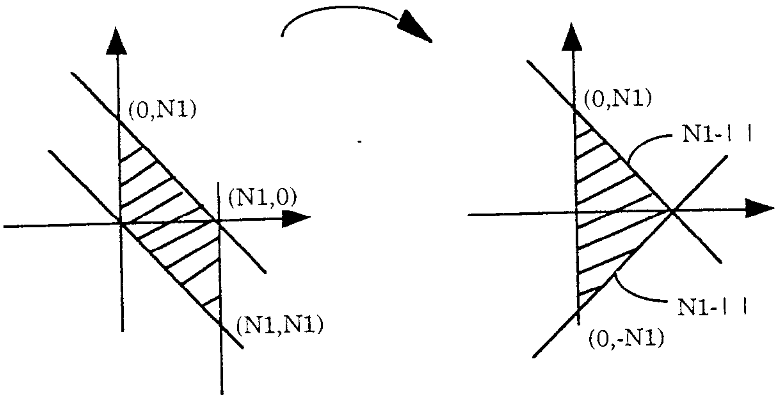

Figure 5.1: The change of order of integration.

$$\Rightarrow MSE \approx \sigma_u^2 \tag{5.3}$$

Thus for very small sampling areas the mean square error is equal to the variance of the sampled velocity values.

For large sampling areas $N_1 \times N_2$ the correlation coefficient is approaching zero and we can take the limit in the expression for the mean square error.

$$\begin{aligned}
\lim_{N_1,N_2\to\infty} N_1N_2MSE &= \lim_{N_1,N_2\to\infty} \sigma_u^2 \int_{-\infty}^{\infty}\int_{-\infty}^{\infty}\left(1-\frac{|\eta|}{N_1}\right)\left(1-\frac{|\nu|}{N_2}\right)K_u(\eta,\nu)d\nu d\eta \\
\Rightarrow \lim_{N_1,N_2\to\infty} N_1N_2MSE &= \sigma_u^2 \int_{-\infty}^{\infty}\int_{-\infty}^{\infty} K_u(\eta,\nu)d\nu d\eta \\
\Rightarrow MSE &= \frac{\sigma_u^2}{N_1N_2}\int_{-\infty}^{\infty}\int_{-\infty}^{\infty} K_u(\eta,\nu)d\nu d\eta \qquad (5.4)
\end{aligned}$$

5.2.2 1D estimates.

Mean velocity estimates in 1D where we sample over a length N_1 instead of over an area, is simply a special case of the 2D relations derrived above. We find the equivalent 1D expressions for the mean square error when estimating the mean velocity to be:

General expression:

$$MSE = \frac{\sigma_u^2}{N_1}\int_{-N_1}^{N_1}\left(1-\frac{|\eta|}{N_1}\right)K_u(\eta)d\eta \tag{5.5}$$

For small sampling lengths:

$$MSE = \sigma_u^2 \tag{1.6}$$

For large sampling lenthgs:

$$MSE = \frac{\sigma_u}{N_1} \int_{-\infty}^{\infty} K_u(\eta) d\eta \tag{1.7}$$

1.2.3 Mean square error for various approximations of $K_u(\eta, \nu)$.

It is now possible for a given flow situation to find the mean square error when estimating the mean value of the velocity over a given sampling area or length. Conversely it is also possible to determine the sampling length or area required to give a certain value of the MSE. Unfortunately there exists no universal form of $K_u(\eta, \nu)$; it has to be determined for the flow situation in question, however for certain flow types the approximate shape of the correlation coefficient is well known and we also require that $K_u(0,0) = 1$ and that $K_u(\eta, \nu) \to 0$ as $\eta, \nu \to \infty$. We will now estimate the mean square error for three approximations of $K_u(\eta, \nu)$, namely :

$$K_u(\eta, \nu) = e^{-\alpha^2 r^2} = e^{-\alpha^2(\eta^2+\nu^2)}$$

$$K_u(\eta, \nu) = e^{-\alpha|\eta|-\beta|\nu|}$$

$$K_u(\eta, \nu) = e^{-\alpha|r|} \cos \beta r = e^{-\alpha(\eta^2+\nu^2)^{\frac{1}{2}}} \cos \beta(\eta^2 + \nu^2)^{\frac{1}{2}}$$

The third form for K_u is representative of flows where there is an underlying periodicity.

For $K_u(\eta, \nu) = e^{-\alpha^2(\eta^2+\nu^2)}$

General expression:

$$\begin{aligned}
MSE &= \frac{\sigma_u^2}{N_1 N_2}\int_{-N_1}^{N_1}\int_{-N_2}^{N_2}\left(1-\frac{|\eta|}{N_1}\right)\left(1-\frac{|\nu|}{N_2}\right)K_u(\eta,\nu)d\nu d\eta \\
&= \frac{\sigma_u^2}{N_1 N_2}\int_{-N_1}^{N_1}\int_{-N_2}^{N_2}\left(1-\frac{|\eta|}{N_1}\right)\left(1-\frac{|\nu|}{N_2}\right)e^{-\alpha^2(\eta^2+\nu^2)}d\nu d\eta \\
&= \frac{\sigma_u^2}{N_1 N_2}\left\{\frac{\sqrt{\pi}}{\alpha}+\frac{1}{\alpha^2 N_1}\left(e^{-\alpha^2 N_1^2}-1\right)\right\} \\
&\quad \times\left\{\frac{\sqrt{\pi}}{\alpha}+\frac{1}{\alpha^2 N_1}\left(e^{-\alpha^2 N_2^2}-1\right)\right\}
\end{aligned} \tag{5.8}$$

As we see this value of the MSE approaches zero as $N_1, N_2 \to \infty$, showing that we have a consistent estimate of the mean velocity.

In the above we have used the following approximation. At some point we have to integrate $\int_{-N_1}^{N_1} e^{\alpha^2\eta^2}d\eta$, it is however not possible to find the exact value of this so we have to approximate. Define the errorfunction $erf(x) = \frac{2}{\sqrt{\pi}}\int_0^x e^{-u^2}du$, and let $u = \alpha\eta \Rightarrow du = \alpha d\eta$ to give

$$\begin{aligned}
\frac{\sqrt{\pi}}{N_1\alpha}erf(x) &= \frac{2}{N_1}\int_{u=0}^{u=x} e^{-\alpha^2\eta^2}d\eta \\
\Rightarrow \frac{\sqrt{\pi}}{N_1\alpha}erf(N_1) &= \frac{2}{N_1}\int_0^{N_1} e^{-\alpha^2\eta^2}d\eta
\end{aligned}$$

$$\begin{aligned}
erf(x) &= \frac{2}{\sqrt{\pi}}\left(x-\frac{x^3}{3\cdot 1!}+\frac{x^5}{5\cdot 2!}-\frac{x^7}{7\cdot 3!}\cdots\right) \\
&\sim 1-\frac{e^{-x^2}}{\sqrt{\pi}x}\left(1-\frac{1}{2x^2}+\frac{1\cdot 3}{(2x^2)^2}-\cdots\right)
\end{aligned}$$

This tends rapidly to unity, at $x = 2$, $erf(x) = 0.9953$ within 1% of 1. Therefore it is reasonable in this context to take $erf(x) = 1$.

$$\frac{2}{N_1}\int_{-N_1}^{N_1} e^{-\alpha^2\eta^2}d\eta = \frac{\sqrt{\pi}}{\alpha}erf(N_1) \approx \frac{\sqrt{\pi}}{\alpha N_1}$$

In the limit for large sampling areas we find the mean square error to be:

$$\begin{aligned} MSE &= \frac{\sigma_u^2}{N_1 N_2} \int_{-\infty}^{\infty} \int_{-\infty}^{\infty} K_u(\eta, \nu) d\nu d\eta \\ &= \frac{\sigma_u^2}{N_1 N_2} \int_{-\infty}^{\infty} \int_{-\infty}^{\infty} e^{-\alpha^2(\eta^2+\nu^2)} d\nu d\eta \\ &= \frac{\sigma_u^2 \pi}{\alpha^2 N_1 N_2} \end{aligned} \tag{5.9}$$

For $K_u(\eta, \nu) = e^{-\alpha|\eta| - \beta|\nu|}, \quad \alpha, \beta > 0$

General expression:

$$\begin{aligned} MSE &= \frac{\sigma_u^2}{N_1 N_2} \int_{-N_1}^{N_1} \int_{-N_2}^{N_2} \left(1 - \frac{|\eta|}{N_1}\right) \left(1 - \frac{|\nu|}{N_2}\right) K_u(\eta, \nu) d\nu d\eta \\ &= \frac{\sigma_u^2}{N_1 N_2} \int_{-N_1}^{N_1} \int_{-N_2}^{N_2} \left(1 - \frac{|\eta|}{N_1}\right) \left(1 - \frac{|\nu|}{N_2}\right) e^{-\alpha|\eta| - \beta|\nu|} d\nu d\eta \\ &= \frac{4\sigma_u^2}{N_1 N_2} \left\{ \frac{1}{\alpha} + \frac{1}{\alpha^2 N_1} \left(e^{-\alpha N_1} - 1 \right) \right\} \\ &\quad \times \left\{ \frac{1}{\beta} + \frac{1}{\beta^2 N_2} \left(e^{-\beta N_2} - 1 \right) \right\} \end{aligned} \tag{5.10}$$

This approaches zero as $N_1, N_2 \to \infty$ showing that we have a consistent estimate of the mean velocity.

For large sampling areas $N_1 \times N_2$ we find the mean square error to be:

$$\begin{aligned} MSE &= \frac{\sigma_u^2}{N_1 N_2} \int_{-\infty}^{\infty} \int_{-\infty}^{\infty} K_u(\eta, \nu) d\nu d\eta \\ &= \frac{\sigma_u^2}{N_1 N_2} \int_{-\infty}^{\infty} \int_{-\infty}^{\infty} e^{-\alpha|\eta| - \beta|\nu|} d\nu d\eta \\ &= \frac{4\sigma_u^2}{N_1 N_2} \frac{1}{\alpha\beta} \end{aligned} \tag{5.11}$$

For $K_u(\eta,\nu) = e^{-\alpha(\eta^2+\nu^2)^{\frac{1}{2}}}\cos\beta(\eta^2+\nu^2)^{\frac{1}{2}}\quad \alpha,\beta > 0$

There is no exact solution for the mean square error with this approximation of $K_u(\eta,\nu)$. When we consider the limit for large sampling areas we are, however, able to determine the value of the mean square error, this involves a transformation to circular polar coordinates.

$$\int_R\int f(x,y)dxdy = \int_{R^*}\int f[x(u,v)y(u,v)]\left|\frac{\partial(x,y)}{\partial(u,v)}\right|dudv$$

Where the Jacobian

$$J = \frac{\partial(x,y)}{\partial(u,v)} = \begin{vmatrix} \frac{\partial x}{\partial u} & \frac{\partial x}{\partial v} \\ \frac{\partial y}{\partial u} & \frac{\partial y}{\partial v} \end{vmatrix}$$

Here $\eta = \cos\theta,\ \nu = \sin\theta$

$$J = \begin{vmatrix} \cos\theta & -r\sin\theta \\ \sin\theta & r\cos\theta \end{vmatrix} = r$$

and

$$\begin{array}{rcl} -\infty & \leq N_1 \leq & \infty \\ -\infty & \leq N_2 \leq & \infty \end{array} \longrightarrow \begin{array}{rcl} 0 & \leq \theta \leq & 2\pi \\ 0 & \leq r \leq & \infty \end{array}$$

thus for large sampling areas we find:

$$\begin{aligned} MSE &= \frac{\sigma_u^2}{N_1N_2}\int_{-\infty}^{\infty}\int_{-\infty}^{\infty} K_u(\eta,\nu)d\nu d\eta \\ &= \frac{\sigma_u^2}{N_1N_2}\int_{-\infty}^{\infty}\int_{-\infty}^{\infty} e^{-\alpha(\eta^2+\nu^2)^{\frac{1}{2}}}\cos\beta(\eta^2+\nu^2)^{\frac{1}{2}}d\nu d\eta \\ &= \frac{\sigma_u^2}{N_1N_2}\int_0^{2\pi}\int_0^{\infty} re^{-\alpha r}\cos\beta r dr d\theta \\ &= \frac{\sigma_u^2}{N_1N_2}\frac{2\pi(\alpha^2-\beta^2)}{(\alpha^2+\beta^2)^2} \end{aligned} \tag{5.12}$$

Similar results have been established for mean velocity estimates over a one-dimensional sampling length N_1, as this is simply a special case of the two-dimensional calculations. The collective results are presented in tables 5.1 and 5.3.

There might be occasions where we are not only interested in the mean square error MSE, but in the ***normalized standard error*** ϵ, where ϵ is the +ve square root of the normalized mean square error ϵ^2. For mean velocity estimates the normalizing factor is μ_u^2, the square of the true mean velocity. The value of ϵ^2 for the various approximations of $K_u(\eta, \nu)$ are presented in tables 5.2 and 5.4.

Table 5.1. *MSE* results for 1D estimates of the mean velocity.

$K_u(\eta) = e^{-\alpha^2\eta^2} \quad \alpha > 0$	
General expression:	$\frac{\sigma_u^2}{N_1}\left\{\frac{\sqrt{\pi}}{\alpha} + \frac{2}{\alpha^2 N_1}\left(e^{-\alpha^2 N_1^2} - 1\right)\right\}$
Small $N_1 \ll 1/\alpha^2$:	σ_u^2
Large $N_1 \gg 1/\alpha^2$:	$\frac{\sigma_u^2\sqrt{\pi}}{N_1\alpha}$

$K_u(\eta, \nu) = e^{-\alpha\|\eta\|} \quad \alpha > 0$	
General expression:	$\frac{2\sigma_u^2}{\alpha N_1}\left\{1 + \frac{1}{\alpha N_1}\left(e^{-\alpha N_1} - 1\right)\right\}$
Small $N_1 \ll 1/\alpha$:	σ_u^2
Large $N_1 \gg 1/\alpha$:	$\frac{2\sigma_u^2}{\alpha N_1}$

$K_u(\eta) = e^{-\alpha\|\eta\|}\cos\beta\eta \quad \alpha, \beta > 0$	
General expression:	$\frac{2\sigma_u^2}{N_1}\left\{\frac{\alpha}{(\alpha^2+\beta^2)} - \frac{1}{N_1}\frac{(\alpha^2-\beta^2)}{(\alpha^2+\beta^2)^2} + \frac{1}{N_1}\frac{\{(\alpha^2-\beta^2)\cos\beta N_1 + 2\alpha\beta\sin\beta N_1\}}{(\alpha^2+\beta^2)^2}\right\}$
Small $N_1 \ll 1/\alpha$:	σ_u^2
Large $N_1 \gg 1/\alpha$:	$\frac{2\sigma_u^2}{N_1}\frac{\alpha}{(\alpha^2+\beta^2)}$

Table 5.2 Normalized MSE, ϵ^2 results for 1D mean velocity estimates.

$K_u(\eta) = e^{-\alpha^2\eta^2} \quad \alpha > 0$	
General expression:	$\frac{\sigma_u^2}{N_1\mu_u^2}\left\{\frac{\sqrt{\pi}}{\alpha} + \frac{2}{\alpha^2 N_1}\left(e^{-\alpha^2 N_1^2} - 1\right)\right\}$
Small $N_1 \ll 1/\alpha^2$:	$\frac{\sigma_u^2}{\mu_u^2}$
Large $N_1 \gg 1/\alpha^2$:	$\frac{\sigma_u^2}{\mu_u^2}\frac{\sqrt{\pi}}{\alpha N_1}$

$K_u(\eta) = e^{-\alpha\lvert\eta\rvert} \quad \alpha > 0$	
General expression :	$\frac{2\sigma_u^2}{\mu_u^2 N_1\alpha}\left\{1 + \frac{1}{\alpha N_1}\left(e^{-\alpha N_1} - 1\right)\right\}$
Small $N_1 \ll 1/\alpha$:	$\frac{\sigma_u^2}{\mu_u^2}$
Large $N_1 \gg 1/\alpha$:	$\frac{2\sigma_u^2}{\mu_u^2 N_1\alpha}$

$K_u(\eta) = e^{-\alpha\lvert\eta\rvert}\cos\beta\eta \quad \alpha, \beta > 0$	
General expression:	$\frac{2\sigma_u^2}{\mu_u^2 N_1}\left\{\frac{\alpha}{(\alpha^2+\beta^2)} - \frac{1}{N_1}\frac{(\alpha^2-\beta^2)}{(\alpha^2+\beta^2)^2}\right.$ $\left.\frac{1}{N_1}\frac{e^{-\alpha N_1}\{(\alpha^2-\beta^2)\cos\beta N_1 + 2\alpha\beta\sin\beta N_1\}}{(\alpha^2+\beta^2)^2}\right\}$
Small $N_1 \ll 1/\alpha$:	$\frac{\sigma_u^2}{\mu_u^2}$
Large $N_1 \gg 1/\alpha$:	$\frac{2\sigma_u^2}{\mu_u^2 N_1}\frac{\alpha}{(\alpha^2+\beta^2)}$

Table 5.3 *MSE* results for 2D estimates of the mean velocity.

--- $K_u(\eta,\nu) = e^{-\alpha^2(\eta^2+\nu^2)}$ $\alpha > 0$	
General expression :	$\frac{\sigma_u^2}{N_1 N_2}\left\{\frac{\sqrt{\pi}}{\alpha} + \frac{1}{\alpha^2 N_1}\left(e^{-\alpha^2 N_1^2} - 1\right)\right\}$ $\times\left\{\frac{\sqrt{\pi}}{\alpha} + \frac{1}{\alpha^2 N_2}\left(e^{-\alpha^2 N_2^2} - 1\right)\right\}$
Small $N_1, N_2 \ll 1/\alpha^2$:	σ_u^2
Large $N_1, N_2 \gg 1/\alpha^2$:	$\frac{\sigma_u^2}{N_1 N_2}\frac{\pi}{\alpha^2}$
$K_u(\eta,\nu) = e^{-\alpha\lvert\eta\rvert-\beta\lvert\nu\rvert}$ $\alpha,\beta > 0$	
General expression :	$\frac{4\sigma_u^2}{N_1 N_2}\left\{\frac{1}{\alpha} + \frac{1}{\alpha^2 N_1}\left(e^{-\alpha N_1} - 1\right)\right\}$ $\times\left\{\frac{1}{\beta} + \frac{1}{\beta^2 N_1}\left(e^{-\beta N_2} - 1\right)\right\}$
Small$N_1, N_2 \ll 1/\alpha,\beta$:	σ_u^2
Large $N_1, N_2 \gg 1/\alpha,\beta$:	$\frac{4\sigma_u^2}{N_1 N_2}\frac{1}{\alpha\beta}$
$K_u(\eta,\nu) = e^{-\alpha(\eta^2+\nu^2)^{\frac{1}{2}}}\cos\beta(\eta^2+\nu^2)^{\frac{1}{2}}$ $\alpha;\beta > 0$	
General expression :	No exact solution exists
Small $N_1, N_2 \ll 1/\alpha$:	σ_u^2
Large $N_1, N_2 \gg 1/\alpha$:	$\frac{\sigma_u^2 2\pi}{N_1 N_2}\frac{(\alpha^2-\beta^2)}{(\alpha^2+\beta^2)^2}$

Table 5.4 Normalized MSE, ϵ^2 results for 2D mean velocity estimates.

$K_u(\eta,\nu) = e^{-\alpha^2(\eta^2+\nu^2)} \quad \alpha > 0$	
General expression :	$\frac{\sigma_u^2}{\mu_u^2 N_1 N_2}\left\{\frac{\sqrt{\pi}}{\alpha} + \frac{1}{\alpha^2 N_1}\left(e^{-\alpha^2 N_1^2} - 1\right)\right\}$ $\times\left\{\frac{\sqrt{\pi}}{\alpha} + \frac{1}{\alpha^2 N_2}\left(e^{-\alpha^2 N_2^2} - 1\right)\right\}$
Small $N_1, N_2 \ll 1/\alpha^2$:	$\frac{\sigma_u^2}{\mu_u^2}$
Large $N_1, N_2 \gg 1/\alpha^2$:	$\frac{\sigma_u^2}{\mu_u^2}\frac{\pi}{\alpha^2 N_1 N_2}$
$K_u(\eta,\nu) = e^{-\alpha\vert\eta\vert-\beta\vert\nu\vert} \quad \alpha,\beta > 0$	
General expression :	$\frac{4\sigma_u^2}{\mu_u^2 N_1 N_2}\left\{\frac{1}{\alpha}\frac{1}{\alpha^2 N_1}\left(e^{-\alpha N_1} - 1\right)\right\}$ $\times\left\{\frac{1}{\beta} + \frac{1}{\beta^2 N_2}\left(e^{-\beta N_2} - 1\right)\right\}$
Small $N_1, N_2 \ll 1/\alpha,\beta$:	$\frac{\sigma_u^2}{\mu_u^2}$
Large $N_1, N_2 \gg 1/\alpha,\beta$:	$\frac{4\sigma_u^2}{\mu_u^2 N_1 N_2}\frac{1}{\alpha\beta}$
$K_u(\eta,\nu) = e^{-\alpha(\eta^2+\nu^2)^{\frac{1}{2}}}\cos\beta(\eta^2+\nu^2)^{\frac{1}{2}} \quad \alpha,\beta > 0$	
General expression :	No exact solution exists
Small $N_1, N_2 \ll 1/\alpha$:	$\frac{\sigma_u^2}{\mu_u^2}$
Large $N_1, N_2 \gg 1/\alpha$:	$\frac{\sigma_u^2}{\mu_u^2}\frac{2\pi}{N_1 N_2}\frac{(\alpha^2-\beta^2)}{(\alpha^2+\beta^2)^2}$

5.3 Mean square value estimates.

5.3.1 2D estimates.

Another useful parameter is the mean square value ψ_u^2. The estimate of the mean square value when averaging over a finite area $N_1 \times N_2$ is

$$\hat{\psi}_u^2 = \frac{1}{N_1}\frac{1}{N_2}\int_0^{N_1}\int_0^{N_2} u^2(x,y)dydx$$

The true mean square value is ψ_u^2, and N_1, N_2 the sampling lengths in the x and y directions respectively.
The expected value of the estimate $\hat{\psi}_u^2$ is

$$E[\hat{\psi}_u^2] = \frac{1}{N_1}\frac{1}{N_2}\int_0^{N_1}\int_0^{N_2} E[u^2(x,y)]dydx = \psi_u^2$$

Hence $\hat{\psi}_u^2$ is an unbiased estimate of the mean square value, and the mean square error MSE is given by the variance of the estimate.

$$MSE = var[\hat{\psi}_u^2] = E[(\hat{\psi}_u^2 - \psi_u^2)^2] = E[\hat{\psi}_u^4] - \psi_u^4$$

We find the expression for the mean square error as follows:

$$\begin{aligned}
MSE &= E[\hat{\psi}_u^4] - \psi_u^4 \\
&= E\left[\frac{1}{N_1^2}\frac{1}{N_2^2}\int_0^{N_1}\int_0^{N_2}\int_0^{N_1}\int_0^{N_2} u^2(r,s)u^2(k,t)dtdkdsdr\right] - \psi_u^4 \\
&= \frac{1}{N_1^2}\frac{1}{N_2^2}\int_0^{N_1}\int_0^{N_2}\int_0^{N_1}\int_0^{N_2} E[u^2(r,s)u^2(k,t)] - \psi_u^4 dtdkdsdr \\
&= \frac{2}{N_1^2 N_2^2}\int_0^{N_1}\int_0^{N_2}\int_0^{N_1}\int_0^{N_2} R_u^2(\underline{k}-\underline{r}) - \mu_u^4 dtdkdsdr \\
&= \frac{2}{N_1^2 N_2^2}\int_0^{N_1}\int_0^{N_2}\int_0^{N_1}\int_0^{N_1} C_u^2(\underline{k}-\underline{r}) + 2\mu_u^2 C_u(\underline{k}-\underline{r})dtdkdsdr \\
&= \frac{2\sigma_u^4}{N_1^2 N_2^2}\int_0^{N_1}\int_0^{N_2}\int_0^{N_1}\int_0^{N_2} K_u^2(\underline{k}-\underline{r}) + \frac{2\mu_u^2}{\sigma_u^2}K_u(\underline{k}-\underline{r})dtdkdsdr \\
&= \frac{2\sigma_u^4}{N_1 N_2}\int_{-N_1}^{N_1}\int_{-N_2}^{N_2}\left(1-\frac{|\eta|}{N_1}\right)\left(1-\frac{|\nu|}{N_2}\right)\left\{K_u^2(\eta,\nu) + \frac{2\mu_u^2}{\sigma_u^2}K_u(\eta,\nu)\right\}d\nu d\eta
\end{aligned}$$

The method of integration is the same as for the estimates of the mean velocity. We have made use of the following relation, valid for a Gaussian probability density function:

$$E[x_1x_2x_3x_4] = E[x_1x_2]E[x_3x_4] + E[x_1x_3]E[x_2x_4] + E[x_1x_4]E[x_2x_3] - 2\mu_{x_1}\mu_{x_2}\mu_{x_3}\mu_{x_4}$$

Leading to:

$$E[u^2(r,s)u^2(k,t)] = \psi_u^4 + 2R_u^2(\underline{k}-\underline{r}) - 2\mu_u^4$$

And from the basic relation $C_u(\underline{r}) = R_u(\underline{r}) - \mu_u^2$ we find

$$C_u^2(\underline{r}-\underline{x}) + 2\mu_u^2 C_u(\underline{r}-\underline{x}) = R_u^2(\underline{r}-\underline{x}) - \mu_u^4$$

Thus we find that the mean square error MSE when estimating the mean square value over a finite area is:

$$MSE = \frac{2\sigma_u^4}{N_1 N_2}\int_{-N_1}^{N_1}\int_{-N_2}^{N_2}\left(1-\frac{|\eta|}{N_1}\right)\left(1-\frac{|\nu|}{N_2}\right)\left\{K_u^2(\eta,\nu)+\frac{2\mu_u^2}{\sigma_u^2}K_u(\eta,\nu)\right\}d\nu d\eta \tag{5.13}$$

This is the general expression valid for all sampling areas. For very small averaging areas the correlation coefficient is almost unity and we find:

$$\begin{aligned} MSE &= \frac{2\sigma_u^4}{N_1 N_2}\int_{-N_1}^{N_1}\int_{-N_2}^{N_2}\left(1-\frac{|\eta|}{N_1}\right)\left(1-\frac{|\nu|}{N_2}\right)\left(1+\frac{2\mu_u^2}{\sigma_u^2}\right) \\ &= \frac{2\sigma_u^4}{N_1 N_2}\left(1+\frac{2\mu_u^2}{\sigma_u^2}\right)N_1 N_2 \\ &= 2\sigma_u^4\left(1+\frac{2\mu_u^2}{\sigma_u^2}\right) \end{aligned} \tag{5.14}$$

If we take the limit for large averaging areas $N_1 \times N_2$ we find the expression for the mean square error to be:

$$\begin{aligned} &\lim_{N_1,N_2\to\infty} N_1 N_2 MSE \\ &= \lim_{N_1,N_2\to\infty} 2\sigma_u^4\int_{-N_1}^{N_1}\int_{-N_2}^{N_2}\left(1-\frac{|\eta|}{N_1}\right)\left(1-\frac{|\nu|}{N_2}\right)\left\{K_u^2(\eta,\nu)+\frac{2\mu_u^2}{\sigma_u^2}K_u(\eta,\nu)\right\}d\nu d\eta \\ \Rightarrow MSE &= \frac{2\sigma_u^4}{N_1 N_2}\int_{-\infty}^{\infty}\int_{-\infty}^{\infty}\left\{K_u^2(\eta,\nu)+\frac{2\mu_u^2}{\sigma_u^2}K_u(\eta,\nu)\right\}d\nu d\eta \end{aligned} \tag{5.15}$$

5.3.2 1D mean square value estimates

It is also possible to estimate the mean square value in one dimension only, that is over a sampling length of N_1. In this case we find the equivalant expressions for the mean square error to be:

General expression:

$$MSE = \frac{2\sigma_u^4}{N_1}\int_{-N_1}^{N_1}\left(1-\frac{|\eta|}{N_1}\right)\left\{K_u^2(\eta)+\frac{2\mu_u^2}{\sigma_u^2}K_u(\eta)\right\}d\nu \tag{5.16}$$

For small sampling lengths :

$$MSE = 2\sigma_u^4\left(1+\frac{2\mu_u^2}{\sigma_u^2}\right) \tag{5.17}$$

For long sampling lengths :

$$MSE = \frac{2\sigma_u^2}{N_1} \int_{-\infty}^{\infty} \left\{ K_u^2(\eta) + \frac{2\mu_u^2}{\sigma_u^2} K_u(\eta) \right\} d\eta \tag{5.18}$$

5.3.3 Mean square error for various approximations of $K_u(\eta, \nu)$.

Results for the mean square error in one- and two-dimensions have been calculated using the approximations for the correlation coefficient $K_u(\eta, \nu)$ introduced in sec. 5.2.3. The results are presented in tables 5.5 and 5.7. The normalizing factor used to obtain the normalized mean square error ϵ^2 is, for mean square value estimates, ψ_u^4 , the square of the true mean square value. Results for ϵ^2 for mean square estimates given the above approximations of $K_u(\eta, \nu)$ are presented in table 6.6 and 5.8.

Table 5.5 *MSE* results for 1D estimates of the mean square value.

$K_u(\eta) = e^{-\alpha^2\eta^2} \quad \alpha > 0$	
General expression :	$\frac{2\sigma_u^4}{N_1}\left\{\frac{\sqrt{\pi}}{\alpha}\left(\frac{1}{\sqrt{2}} + \frac{2\mu_u^2}{\sigma_u^2}\right) + \frac{1}{\alpha^2 N_1} e^{-\alpha^2 N_1^2}\left(\frac{1}{2}e^{-\alpha^2 N_1^2} - \frac{2\mu_u^2}{\sigma_u^2}\right) + \frac{1}{\alpha^2 N_1^2}\left(\frac{1}{\alpha^2} + \frac{2\mu_u^2}{\sigma_u^2}\right)\right\}$
Small $N_1 \ll 1/\alpha$:	$2\sigma_u^4\left(1 + \frac{2\mu_u^2}{\sigma_u^2}\right)$
Large $N_1 \gg 1/\alpha$:	$\frac{2\sigma_u^4}{\alpha N_1}\left\{\sqrt{\frac{\pi}{2}}\left(1 + \frac{2\sqrt{2}\mu_u^2}{\sigma_u^2}\right)\right\}$
$K_u(\eta) = e^{-\alpha\lvert\eta\rvert} \quad \alpha > 0$	
General expression :	$\frac{4\sigma_u^4}{\alpha N_1}\left\{\left(\frac{1}{2} + \frac{2\mu_u^2}{\sigma_u^2}\right) + \frac{1}{4\alpha N_1} e^{-\alpha N_1}\left(e^{-\alpha N_1} + \frac{8\mu_u^2}{\sigma_u^2}\right) - \frac{1}{4\alpha N_1}\left(1 + \frac{8\mu_u^2}{\sigma_u^2}\right)\right\}$
Small $N_1 \ll 1/\alpha$:	$2\sigma_u^4\left(1 + \frac{2\mu_u^2}{\sigma_u^2}\right)$
Large $N_1 \gg 1/\alpha$:	$\frac{2\sigma_u^4}{\alpha N_1}\left(1 + \frac{4\mu_u^2}{\sigma_u^2}\right)$
$K_u(\eta) = e^{-\alpha\lvert\eta\rvert}\cos\beta\eta \quad \alpha, \beta > 0$	
General expression :	$\frac{4\sigma_u^4}{\alpha N_1}\left\{\frac{1}{2} + \frac{2\alpha^2}{(4\alpha^2+4\beta^2)^2} + \frac{\alpha}{N_1}\frac{e^{-2\alpha N_1}\{(4\alpha^2-4\beta^2)\cos 2\beta N_1 + 8\alpha\beta\sin 2\beta N_1\}}{(\alpha^2+\beta^2)^2} + \frac{2\mu_u^2}{\sigma_u^2}\left\{\frac{\alpha^2}{(\alpha^2+\beta^2)^2} + \frac{\alpha}{N_1}\frac{e^{-\alpha N_1}\{(\alpha^2-\beta^2)\cos\beta N_1 + 2\alpha\beta\sin\beta N_1\}}{(\alpha^2+\beta^2)^2} + \frac{\alpha(\alpha^2-\beta^2)}{(\alpha^2+\beta^2)^2}\right\}\right\}$
Small $N_1 \ll 1/\alpha$:	$2\sigma_u^4\left(1 + \frac{2\mu_u^2}{\sigma_u^2}\right)$
Large $N_1 \gg 1/\alpha$:	$\frac{2\sigma_4}{N_1}\left(\frac{1}{\alpha} + \frac{\alpha}{(\alpha^2+\beta^2)}\left(1 + \frac{4\mu_u^2}{\sigma_u^2}\right)\right)$

Table 5.6 Normalized MSE, ϵ^2 results for 1D mean square estimates.

$K_u(\eta) = e^{-\alpha^2\eta^2} \quad \alpha > 0$	
General expression :	$\frac{2}{\left(1+\frac{\mu_u^2}{\sigma_u^2}\right)^2 N_1}\Big\{\frac{\sqrt{\pi}}{\alpha}\left(\frac{1}{\sqrt{2}}+\frac{2\mu_u^2}{\sigma_u^2}\right)$ $+\frac{e^{-\alpha^2 N_1^2}}{\alpha^2 N_1}\left(\frac{e^{-\alpha^2 N_1}}{2}-\frac{2\mu_u^2}{\sigma_u^2}\right)+\frac{1}{\alpha^2 N_1}\left(\frac{1}{\alpha^2}+\frac{2\mu_u^2}{\sigma_u^2}\right)\Big\}$
Small $N_1 \ll 1/\alpha^2$:	$2\left(1+\frac{2\mu_u^2}{\sigma_u^2}\right)\Big/\left(1+\frac{\mu_u^2}{\sigma_u^2}\right)^2$
Large $N_1 \gg 1/\alpha^2$:	$\frac{2}{\alpha N_1}\sqrt{\frac{\pi}{2}}\left(1+\frac{2\sqrt{2}\mu_u^2}{\sigma_u^2}\right)\Big/\left(1+\frac{\mu_u^2}{\sigma_u^2}\right)$
$K_u(\eta) = e^{-\alpha\lvert\eta\rvert} \quad \alpha > 0$	
General expression :	$\frac{2}{\alpha N_1\left(1+\frac{\mu_u^2}{\sigma_u^2}\right)^2}\Big\{\left(1+\frac{4\mu_u^2}{\sigma_u^2}\right)$ $+\frac{e^{-\alpha N_1}}{\alpha N_1}\left(\frac{e^{-\alpha N_1}}{2}+\frac{4\mu_u^2}{\sigma_u^2}\right)-\frac{1}{\alpha N_1}\left(\frac{1}{2}+\frac{4\mu_u^2}{\sigma_u^2}\right)\Big\}$
Small $N_1 \ll 1/\alpha$:	$2\left(1+\frac{2\mu_u^2}{\sigma_u^2}\right)\Big/\left(1+\frac{\mu_u^2}{\sigma_u^2}\right)^2$
Large $N_1 \gg 1/\alpha$:	$\frac{2}{\alpha N_1}\left(1+\frac{4\mu_u^2}{\sigma_u^2}\right)\Big/\left(1+\frac{\mu_u^2}{\sigma_u^2}\right)^2$
$K_u(\eta) = e^{-\alpha\lvert\eta\rvert}\cos\beta\eta \quad \alpha,\beta > 0$	
General expression :	$\frac{4}{\alpha N_1\left(1+\frac{\mu_u^2}{\sigma_u^2}\right)^2}\Big\{\frac{1}{2}+\frac{2\alpha^2}{(4\alpha^2+4\beta^2)}+\frac{2\mu_u^2}{\sigma_u^2}\frac{\alpha(\alpha^2-\beta^2)}{(\alpha^2+\beta^2)^2}$ $+\frac{\alpha}{N_1}\frac{e^{-2\alpha N_1}\{(4\alpha^2-4\beta^2)\cos 2\beta N_1+8\alpha\beta\sin 2\beta N_1\}}{(\alpha^2+\beta^2)^2}$ $+\frac{2\mu_u^2}{\sigma_u^2}\Big\{\frac{\alpha^2}{(\alpha^2+\beta^2)}+\frac{\alpha}{N_1}\frac{e^{-\alpha N_1}\{(\alpha^2-\beta^2)\cos\beta N_1+2\alpha\beta\sin\beta N_1\}}{(\alpha^2+\beta^2)^2}\Big\}\Big\}$
Small $N_1 \ll 1/\alpha$:	$2\left(1+\frac{2\mu_u^2}{\sigma_u^2}\right)\Big/\left(1+\frac{\mu_u^2}{\sigma_u^2}\right)^2$
Large $N_1 \gg 1/\alpha$:	$2\left(\frac{1}{\alpha}+\frac{\alpha}{(\alpha^2+\beta^2)}\left(1+\frac{4\mu_u^2}{\sigma_u^2}\right)\right)\Big/N_1\left(1+\frac{\mu_u^2}{\sigma_u^2}\right)^2$

Table 5.7 *MSE* results for 2D estimates of the mean square value.

$K_u(\eta,\nu) = e^{-\alpha^2(\eta^2+\nu^2)} \quad \alpha > 0$	
General expression :	$\frac{2\sigma_u^4}{\alpha^2 N_1 N_2}\left\{\left\{\sqrt{\frac{\pi}{2}}+\frac{1}{2\alpha N_1}\left(e^{-2\alpha^2N_1^2}-1\right)\right\}\left\{\sqrt{\frac{\pi}{2}}+\frac{1}{2\alpha N_2}\left(e^{-2\alpha^2N_2^2}-1\right)\right\} + \frac{2\mu_u^2}{\sigma_u^2}\left\{\sqrt{\pi}+\frac{1}{\alpha N_1}\left(e^{-\alpha^2N_1^2}-1\right)\right\}\left\{\sqrt{\pi}+\frac{1}{\alpha N_2}\left(e^{-\alpha^2N_2^2}-1\right)\right\}\right\}$
Small $N_1, N_2 \ll 1/\alpha$:	$2\sigma_u^4\left(1+\frac{2\mu_u^2}{\sigma_u^2}\right)$
Large $N_1, N_2 \gg 1/\alpha$:	$\frac{\pi\sigma_u^4}{\alpha^2 N_1 N_2}\left(1+\frac{4\mu_u^2}{\sigma_u^2}\right)$

$K_u(\eta,\nu) = e^{-\alpha\lvert\eta\rvert-\beta\lvert\nu\rvert} \quad \alpha,\beta > 0$	
General expression :	$\frac{2\sigma_u^4}{\alpha\beta N_1 N_2}\left\{\left\{1-\frac{1}{2N_1}\left(\frac{1}{2}-e^{-2\alpha N_1}\right)\right\}\left\{1-\frac{1}{2N_2}\left(\frac{1}{2}-e^{-2\beta N_2}\right)\right\} + \frac{8\mu_u^2}{\sigma_u^2}\left\{1-\frac{1}{N_1}\left(1-e^{-\alpha N_1}\right)\right\}\left\{1-\frac{1}{N_2}\left(1-e^{-\beta N_2}\right)\right\}\right\}$
Small $N_1, N_2 \ll 1/\alpha,\beta$:	$2\sigma_u^4\left(1+\frac{2\mu_u^2}{\sigma_u^2}\right)$
Large $N_1, N_2 \gg 1/\alpha,\beta$:	$\frac{2\sigma_u^4}{\alpha\beta N_1 N_2}\left(1+\frac{8\mu_u^2}{\sigma_u^2}\right)$

$K_u(\eta,\nu) = e^{-\alpha(\eta^2+\nu^2)^{\frac{1}{2}}}\cos\beta(\eta^2+\nu^2)^{\frac{1}{2}} \quad \alpha,\beta > 0$	
General expression :	No exact solution exists
Small $N_1, N_2 \ll 1/\alpha,\beta$:	$2\sigma_u^4\left(1+\frac{2\mu_u^2}{\sigma_u^2}\right)$
Large $N_1, N_2 \gg 1/\alpha,\beta$:	$\frac{\pi\sigma_u^4}{2N_1 N_2}\left\{\frac{1}{\alpha^2}+\frac{(\alpha^2-\beta^2)}{(\alpha^2+\beta^2)^2}\left(1+\frac{4\mu_u^2}{\sigma_u^2}\right)\right\}$

Table 5.8 Normalized MSE, ϵ^2 results for 2D mean square estimates.

$K_u(\eta,\nu) = e^{-\alpha^2(\eta^2+\nu^2)} \ \ \alpha > 0$	
General expression :	$\frac{2}{\alpha^2 N_1 N_2 (1+\frac{\mu_u^2}{\sigma_u^2})^2} \left\{ \left\{ \sqrt{\frac{\pi}{2}} + \frac{1}{2\alpha N_1}\left(e^{-2\alpha^2 N_1^2} - 1\right)\right\} \left\{ \sqrt{\frac{\pi}{2}} + \frac{1}{2\alpha N_2}\left(e^{-2\alpha^2 N_2^2} - 1\right)\right\} + \frac{2\mu_u^2}{\sigma_u^2}\left\{\sqrt{\pi} + \frac{1}{\alpha N_2}\left(e^{-\alpha^2 N_1^2} - 1\right)\right\}\left\{\sqrt{\pi} + \frac{1}{\alpha N_2}\left(e^{-\alpha^2 N_2^2} - 1\right)\right\}\right\}$
Small $N_1, N_2 \ll 1/\alpha$:	$2\left(1+\frac{2\mu_u^2}{\sigma_u^2}\right) \Big/ \left(1+\frac{\mu_u^2}{\sigma_u^2}\right)^2$
Large $N_1, N_2 \gg 1/\alpha$:	$\frac{\pi}{\alpha^2 N_1 N_2}\left(1+\frac{4\mu_u^2}{\sigma_u^2}\right) \Big/ \left(1+\frac{\mu_u^2}{\sigma_u^2}\right)^2$
$K_u(\eta,\nu) = e^{-\alpha\lvert\eta\rvert-\beta\lvert\nu\rvert} \ \ \alpha,\beta > 0$	
General expression :	$\frac{2}{\alpha\beta N_1 N_2 (1+\frac{\mu_u^2}{\sigma_u^2})^2}\left\{1-\frac{1}{2N_1}\left(\frac{1}{2}-e^{-2\alpha N_1}\right)\right\}\left\{1-\frac{1}{2N_2}\left(\frac{1}{2}-e^{-2\beta N_2}\right)\right\} + \frac{8\mu_u^2}{\sigma_u^2}\left\{1-\frac{1}{N_1}\left(1-e^{-\alpha N_1}\right)\right\}\left\{1-\frac{1}{N_2}\left(1-e^{-\beta N_2}\right)\right\}$
Small $N_1, N_2 \ll 1/\alpha,\beta$:	$2\left(1+\frac{2\mu_u^2}{\sigma_u^2}\right) \Big/ \left(1+\frac{\mu_u^2}{\sigma_u^2}\right)^2$
Large $N_1, N_2 \gg 1/\alpha,\beta$:	$\frac{2}{\alpha\beta N_1 N_2}\left(1+\frac{8\mu_u^2}{\sigma_u^2}\right) \Big/ \left(1+\frac{\mu_u^2}{\sigma_u^2}\right)^2$
$K_u(\eta,\nu) = e^{-\alpha(\eta^2+\nu^2)^{\frac{1}{2}}} \cos\beta(\eta^2+\nu^2)^{\frac{1}{2}} \ \ \alpha,\beta > 0$	
General expression :	No exact solution exists
Small $N_1, N_2 \ll 1/\alpha$:	$2\left(1+\frac{2\mu_u^2}{\sigma_u^2}\right) \Big/ \left(1+\frac{\mu_u^2}{\sigma_u^2}\right)^2$
Large $N_1, N_2 \gg 1/\alpha$:	$\frac{\pi}{2N_1 N_2}\left\{\frac{1}{\alpha^2} + \frac{(\alpha^2-\beta^2)}{(\alpha^2+\beta^2)^2}\left(1+\frac{4\mu_u^2}{\sigma_u^2}\right)\right\} \Big/ \left(1+\frac{\mu_u^2}{\sigma_u^2}\right)^2$

5.3.4 The mean square error for RMS estimates.

Often it is the rms value we seek when we estimate the mean square value, so we must relate the mean square error for the mean square value to the mean square error for the rms value. As before the estimate of the mean square value over a sampling area $N_1 \times N_2$ is

$$\hat{\psi}_u^2 = \frac{1}{N_1}\frac{1}{N_2}\int_0^{N_1}\int_0^{N_2} u^2(x,y)dydx$$

The estimate of the rms is $\hat{\psi}_u = +\sqrt{\hat{\psi}_u^2}$
The true value of the mean square value is ψ_u^2 and the true value of the rms velocity is ψ_u.
Using the Taylor expansion, which for a function $f(\xi)$ expanded about a is :

$$f(\xi) \approx f(a) + f'(a)(\xi - a) + f''(a)\frac{(\xi - a)^2}{2!} + \cdots$$

Here let $\xi = \hat{\psi}_u^2$, $f(\xi) = \sqrt{\xi}$ and expand about $a = \psi_u^2$. Thus we find that

$$\begin{aligned}
\hat{\psi}_u &= f(\xi) = \sqrt{\xi} \approx \sqrt{a} + \frac{1}{2\sqrt{a}}(\xi - a) - \frac{1}{4a^{3/2}}\frac{(\xi - a)^2}{2!}\cdots \\
\Rightarrow \hat{\psi}_u^2 &\approx \sqrt{\psi_u^2} + \frac{1}{2\sqrt{\psi_u^2}}(\hat{\psi}_u^2 - \psi_u^2) - \frac{1}{8\psi_u^3}(\hat{\psi}_u^2 - \psi_u^2)^2 \\
&= \psi_u + \frac{1}{2\psi_u}(\hat{\psi}_u^2 - \psi_u^2) - \frac{1}{\psi_u^3}(\hat{\psi}_u^2 - \psi_u^2)^2 \\
\Rightarrow \hat{\psi}_u - \psi_u &\approx \frac{1}{2\psi_u}(\hat{\psi}_u^2 - \psi_u^2) - \frac{1}{8\psi_u^3}(\hat{\psi}_u^2 - \psi_u^2)^2 \\
\Rightarrow (\hat{\psi}_u - \psi_u)^2 &\approx \frac{1}{4}\frac{(\hat{\psi}_u^2 - \psi_u^2)^2}{\psi_u^2} \\
& \text{we have ignored two terms see below} \\
\Rightarrow var[\hat{\psi}_u] &= E[(\hat{\psi}_u - \psi_u)^2] \approx \frac{1}{4}\frac{E[(\hat{\psi}_u^2 - \psi_u^2)^2]}{\psi_u^2} \\
\Rightarrow var[\hat{\psi}_u] &\approx \frac{1}{4}\frac{var[\hat{\psi}_u^2]}{\psi_u^2} \\
\Rightarrow \frac{var[\hat{\psi}_u]}{\psi_u^2} &\approx \frac{1}{4}\frac{var[\hat{\psi}_u^2]}{\psi_u^4} \\
\Rightarrow \epsilon_{rms}^2 &\approx \frac{1}{4}\epsilon_{ms}^2 \\
\Rightarrow \epsilon_{rms} &\approx \frac{1}{2}\epsilon_{ms} \qquad (5.19)
\end{aligned}$$

ϵ_{rms} is the normalized standard error for the rms value, $\epsilon_{rms} = \frac{s.d.[\hat{\psi}_u]}{\psi_u}$, where $s.d.$ denotes the standard deviation, that is the +ve square root of the variance.

Likewise we find the normalized standard error for the mean square value $\epsilon_{ms} = \frac{s.d.[\hat{\psi}_u^2]}{\psi_u^2}$.
In the above we at some point ignored the two terms $+\frac{1}{64\psi_u^4}(\hat{\psi}_u^2 - \psi_u^2)^4 - \frac{1}{8\psi_u^4}(\hat{\psi}_u^2 - \psi_u^2)^3$. As the first term is smaller than the last the result is that we have ignored a small negative factor leading to the final result that the normalized standard error for the rms value is smaller than or equal to approximately half the normalized standard error for the mean square value.

5.4 Longitudinal correlationfunction estimates.

Suppose we have a spatially stationary and ergodic velocity record $u(x)$ sampled over the length N_1. Define the longitudinal correlationfunction $f(r)$ as follows:

$$f(r) = \frac{\overline{u_x(x)u_x(x+r)}}{\overline{u_x^2(x)}}$$

Where $u_x(x)$ denotes the velocity in the x-direction at the point x. The estimate of the correlationfunction over the sampling length N_1 is :

$$\hat{f}(x_1) = \frac{1}{N_1}\int_0^{N_1} f(x_1)dx \quad , \; 0 < x_1 < N_1$$

The true value is $f(x_1) = E[f(x_1)]$. The expected value of the estimate $\hat{f}(x_1)$ is:

$$E[\hat{f}(x_1)] = \frac{1}{N_1}\int_0^{N_1} E[f(x_1)]dx = f(x_1)$$

Showing that $\hat{f}(x_1)$ is an unbiased estimate of $f(x_1)$. Thus we find that the mean square error MSE is given by:

$$\begin{aligned}
MSE &= var[\hat{f}(x_1)] \\
&= E[(\hat{f}(x_1) - f(x_1))^2| \\
&= E[\hat{f}^2(x_1)] - f^2(x_1) \\
&= E\left[\frac{1}{N_1^2}\int_0^{N_1}\int_0^{N_1} f(x_1)f(x_1)dkdr\right] - f^2(x_1) \\
&= \frac{1}{N_1^2}\int_0^{N_1}\int_0^{N_1} E\left[\frac{\overline{u_x(r)u_x(r+x_1)}}{\overline{u_x^2(r)}}\frac{\overline{u_x(k)u_x(k+x_1)}}{\overline{u_x^2(k)}}\right] dkdr - f^2(x_1) \\
&= \frac{1}{N_1^2}\int_0^{N_1}\int_0^{N_1} f^2(x_1) + f^2(k-r) \\
&\quad +f(k-r+x_1)f(k-r-x_1)dkdr - f^2(x_1) \\
&= \frac{1}{N_1^2}\int_0^{N_1}\int_0^{N_1} f^2(k-r) + f(k-r+x_1)f(k-r-x_1)dkdr
\end{aligned}$$

$$
\begin{aligned}
&= \frac{1}{N_1^2}\int_0^{N_1}\int_{-r}^{N_1-r} f^2(\eta)+f(\eta+x_1)f(\eta-x_1)d\eta dr \\
&= \frac{1}{N_1^2}\int_{-N_1}^{N_1}\int_0^{N_1-|\eta|} f^2(\eta)+f(\eta+x_1)f(\eta-x_1)drd\eta \\
\Rightarrow MSE &= \frac{1}{N_1}\int_{-N_1}^{N_1}\left(1-\frac{|\eta|}{N_1}\right)\left(f^2(\eta)+f(\eta+x_1)f(\eta-x_1)\right)d\eta \qquad (5.20)
\end{aligned}
$$

In the above we have assumed zero mean velocity $\mu_u = 0$, in order to make the derivation simpler. In a practical flow situation, the mean velocity will be subtracted before any statistical parameters are calculated. We have also used the relation for $E[x_1x_2x_3x_4]$ mentioned earlier.
It is worth noting that this is the mean square error for $f(x_1)$ and that $f(\eta)$ is the general form of the longitudinal correlationfunction. In order for the above expression to make sense we must impose the criteria that the length over which we sample is larger than the correlation length for which we are trying to estimate the error i.e.$N_1 \geq x_1$. It is to be expected that the mean square error varies according to the argument of the correlationfunction x_1.

In the limit for large sampling lengths N_1, we find the mean square error to be:

$$MSE = \frac{1}{N_1}\int_{-\infty}^{\infty}\left(f^2(\eta)+f(\eta+x_1)f(\eta-x_1)\right)d\eta \qquad (5.21)$$

5.4.1 Mean square error evaluations for various approximations of $f(\eta)$.

The validity of using an approximation to the longitudinal correlationfunction when estimating the mean square error in the same is debatable. We have, however, chosen to carry the argument through for the purpose of comparison with the previous results. Again the various approaches, methods and approximations are covered in previous sections, so no detailed calculations are presented. The results are shown in Table 5.9.

Table 5.9 Result for estimates of the longitudinal correlationfunction $f(x_1)$ sampled over a length N_1, $N_1 \geq x_1$.

$f(\eta) = e^{-\alpha^2\eta^2} \quad \alpha > 0$	
General expression :	$\frac{\left(1+e^{-2\alpha^2 x_1}\right)}{\alpha N_1}\left\{\sqrt{\frac{\pi}{2}} - \frac{1}{2\alpha N_1}\left(1 - e^{-2\alpha^2 N_1^2}\right)\right\}$
Large $N_1 \gg 1/\alpha$:	$\sqrt{\frac{\pi}{2}}\frac{\left(1+e^{-2\alpha^2 x_1^2}\right)}{\alpha N_1}$
$f(\eta) = e^{-\alpha\|\eta\|} \quad \alpha > 0$	
General expression :	$\frac{1}{N_1}\left\{e^{-2\alpha x_1}(2x_1 + 1/\alpha) + \frac{1}{\alpha} - \frac{1}{\alpha N_1}\left(e^{-2\alpha x_1}(\alpha x_1^2 + x_1 + 1/2\alpha) - \frac{e^{-2\alpha N_1}}{\alpha}\right)\right\}$
Large $N_1 \gg 1/\alpha$:	$\frac{1}{\alpha N_1}\left(e^{-2\alpha x_1}(1 + 2\alpha x_1) + 1\right)$
$f(\eta) = e^{-\alpha\|\eta\|}\cos\beta\eta \quad \alpha, \beta > 0$	
General expression :	$A\frac{1}{N_1} + B\frac{1}{N_1^2} + C\frac{e^{-2\alpha N_1}}{N_1} + D\frac{e^{-2\alpha N_1}}{N_1}(\alpha\cos 2\beta N_1 - \beta\sin 2\beta N_1) + E\frac{e^{-2\alpha N_1}}{N_1^2} + F$ A, B, C, D, E, F are constant functions of $\cos x_1$, $\sin x_1$, α and β
Large $N_1 \gg 1/\alpha$:	$\frac{1}{2N_1}\left\{\frac{1}{\alpha}\frac{4\alpha}{(4\alpha^2+4\beta^2)} + \frac{e^{-2\alpha x_1}}{\alpha\beta(4\alpha^2+4\beta^2)}\left((5\alpha^2\beta + 4\beta^3)\cos 2\beta x_1 + \alpha(4\alpha^2 + 4\beta^2)\sin 2\beta x_1\right) + 2x_1 e^{-2\alpha x_1}\cos 2\beta x_1\right\}$

Note that for any given sampling length N_1, the mean square error is smaller for larger correlationlengths x_1.

5.5 Discussion and simplification of the results.

We have found, similarly to results for LDA, that since we have unbiased estimates of the mean, mean square value and correlationfunction, the mean square error for these are equal to the variance of the estimate. From this we have found the form of the mean square error given three different approximations of the correlationcoefficient, the results of most interest being the ones for small and large sampling lengths or areas. In the following we will extract simplified expression from the above results. To this purpose we define the *integral lengthscale* L_1 L_2 in one and two dimensions respectively.

$$L_1 = \int_0^\infty K_u(\eta)d\eta \tag{5.22}$$

$$L_2 = \int_0^\infty \int_0^\infty K_u(\eta,\nu)d\nu d\eta \tag{5.23}$$

The integral lengthscale is a measure of the length over which some sort of correlation persists, it is thus related to the size of eddies in the flow, and ultimatively to physical factors governing the flow. It should therefore be possible to determine L_1, L_2 from prerequisite knowledge about the flow in question.

5.5.1 Simplified results for mean velocity estimates.

It is now possible to determine the mean square error if the exact form of the correlationcoefficient is known, the result can be found in the tables provided. The most important result however is that for small sampling areas the mean square error is equal to the variance of the sampled values σ_u^2, and from this we find the normalized mean square error $\epsilon^2 = \frac{\sigma_u^2}{\mu_u^2}$. This latter expression is actually the square of the ratio of the fluctuating, or dynamic, component of the velocity to the mean velocity, which for turbulent flows is the rms turbulence level. This result is independent of the choice of approximation for K_u.

For large sampling areas we have found the form of the mean square error to be:

$$MSE = \frac{\sigma_u^2}{N_1}\int_{-\infty}^{\infty} K_u(\eta)d\eta \quad \text{in 1D}$$

$$MSE = \frac{\sigma_u^2}{N_1 N_2}\int_{-\infty}^{\infty}\int_{-\infty}^{\infty} K_u(\eta,\nu)d\nu d\eta \quad \text{in 2D}$$

If we compare this with the definition of the integral lengthscale (5.22),(5.23) above, and normalize the result, we find **The normalized mean square error** ϵ^2 to be:

$$\epsilon^2 = \frac{2L_1}{N_1}\frac{\sigma_u^2}{\mu_u^2} \quad \text{in 1D} \tag{5.24}$$

$$\epsilon^2 = \frac{4L_2}{N_1 N_2}\frac{\sigma_u^2}{\mu_u^2} \quad \text{in 2D} \qquad (5.25)$$

Thus, as was the case for small sampling lengths or areas, we need not consider the form of the curve for the correlationcoefficient in order to estimate the mean square error for a given sampling length or area, or conversely when we want to estimate the lenght or area required to give a certain value for the MSE.
Below are tables giving examples of the above expression given certain values of $\frac{\sigma_u^2}{\mu_u^2}$ and L_1 L_2. The last column gives the required value of the sampling length or area required to yield a normalized standard error of 0.02 (2%).

1D	$\frac{\sigma_u}{\mu_u}$	L_1 (mm)	ϵ^2	$\epsilon = \Rightarrow$	$N_1 =$ (mm)
	0.02	50	$0.04/N_1$	0.02	100
	0.04	50	$0.16/N_1$	0.02	400
	0.06	50	$0.36/N_1$	0.02	900

2D	$\frac{\sigma_u}{\mu_u}$	L_2 (mm^2)	ϵ^2	$\epsilon = \Rightarrow$	$N_1 \times N_2 =$ (mm^2)
	0.02	$(50)^2$	$4/N_1N_2$	0.02	$(100)^2$
	0.04	$(50)^2$	$16/N_1N_2$	0.02	$(200)^2$
	0.06	$(50)^2$	$36/N_1N_2$	0.02	$(300)^2$

It is noteworthy that such relatively large sampling lengths/areas are required in order to obtain a normalized mean square error of 0.02 . Also, not unexpectedly, that the higher the level of rms turbulence in the flow, the larger the error or corresponding required sampling length/area.

5.5.2 Simplified results for mean square estimates.

Simplification in this case is not as straightforward as for mean velocity estimates. As we will see the situation is more complicated, and the form of the approximation does influence the outcome, except for very small sampling lengths or areas where the normalized mean square error takes the form:

$$\epsilon^2 = \frac{2\left(1 + \frac{2\mu_u^2}{\sigma_u^2}\right)}{\left(1 + \frac{\mu_u^2}{\sigma_u^2}\right)^2}$$

This is independent of sampling length/area and approximation of K_u.

For large sampling lengths/areas we found the MSE (eqn.5.15 , 5.18). As these expressions contain the factor $K_u^2(\eta,\nu)$ $K_u^2(\eta)$ respectively , they do not lend themselves to a simple substitution for the integral lengthscale, we have to calculate this in each individual case and then substitute it in the expression for the normalized mean square error ϵ^2 . In Table 5.10 below we present the simplified results and integral lenghtscales for the various approximations of K_u.

Table 5.10 Simplified results and integral lengthscales for the given approximations of K_u.

Approximation of K_u	ϵ^2	*integral lengthscale*
$e^{-\alpha^2\eta^2}$	$\frac{2\sqrt{2}L_1}{N_1}\frac{\left(1+\frac{2\sqrt{2}\mu_u^2}{\sigma_u^2}\right)}{\left(1+\frac{\mu_u^2}{\sigma_u^2}\right)^2}$	$L_1 = \frac{\sqrt{\pi}}{2\alpha}$
$e^{-\alpha\|\eta\|}$	$\frac{2L_1}{N_1}\frac{\left(1+\frac{4\mu_u^2}{\sigma_u^2}\right)}{\left(1+\frac{\mu_u^2}{\sigma_u^2}\right)^2}$	$L_1 = \frac{1}{\alpha}$
$e^{-\alpha\|\eta\|}\cos\beta\eta$	$\frac{2}{N_1}\left(\frac{1}{\alpha}+L_1\right)\frac{\left(1+\frac{4\mu_u^2}{\sigma_u^2}\right)}{\left(1+\frac{\mu_u^2}{\sigma_u^2}\right)^2}$	$L_1 = \frac{\alpha}{(\alpha^2+\beta^2)^2}$
$e^{-\alpha^2(\eta^2+\nu^2)^2}$	$\frac{4L_2}{N_1N_2}\frac{\left(1+\frac{4\mu_u^2}{\sigma_u^2}\right)}{\left(1+\frac{\mu_u^2}{\sigma_u^2}\right)^2}$	$L_2 = \frac{\pi}{4\alpha^2}$
$e^{-\alpha\|\eta\|-\beta\|\nu\|}$	$\frac{2L_2}{N_1N_2}\frac{\left(1+\frac{8\mu_u^2}{\sigma_u^2}\right)}{\left(1+\frac{\mu_u^2}{\sigma_u^2}\right)^2}$	$L_2 = \frac{1}{\alpha\beta}$
$e^{-\alpha(\eta^2+\nu^2)^{\frac{1}{2}}}\cos\beta(\eta^2+\nu^2)^{\frac{1}{2}}$	$\frac{1}{N_1N_2}\frac{\left(\frac{\pi}{2\alpha}+4L_2\left(1+\frac{4\mu_u^2}{\sigma_u^2}\right)\right)}{\left(1+\frac{\mu_u^2}{\sigma_u^2}\right)^2}$	$L_2 = \frac{\pi(\alpha^2-\beta^2)}{(\alpha^2+\beta^2)^2}$

We find, as expected, that the results differ, although for the two first approximations there is a certain similarity. Later we will show that they are so similar that they are almost interchangeable. For the third approximation involving the cosine term there are greater differences. We have not succeeded in eliminating the factor α entirely but it would seem reasonble to state that it is very closely related to the integral lengthscale; it is the integral lengthscale for the approximation $e^{-\alpha|\eta|}$. If we thus take this factor to be of the same order as the integral lengthscale for the given approximation, we find the end result to be near twice that of the other approximations. For a flow situation to have a correlation coefficient of the form $e^{-\alpha|\eta|}\cos\beta\eta$, that is it does not approach zero smoothly but oscillates about the axis while tailing off, there would have to be dominant converging and/or diverging flowpatterns f.ex. sinks or sources. This type of correlation is for instance common in any type of vortex shedding, and is relevant for motions under water waves. For these types of flow it is not unreasonable to expect larger mean square errors, than for more 'well-behaved' flow regimes.

As in the previous section we present tables of the simplified results, with given values of $\frac{\sigma_u}{\mu_u}$ and L_1, L_2 and the sampling lengths/areas required to yield $\epsilon = 0.02$.

Table 5.11 Simplified results and integral lengthscales for the given approximations of K_u.

1D	$\frac{\sigma_u}{\mu_u}$	L_1(mm)	ϵ^2	$\epsilon = \Rightarrow$ $N_1 =$ (mm)	
$e^{-\alpha^2\eta^2}$	0.02	50	$0.16/N_1$	0.02	400
	0.04	50	$0.64/N_1$	0.02	1596
	0.06	50	$1.43/N_1$	0.02	3579
$e^{-\alpha|\eta|}$	0.02	50	$0.16/N_1$	0.02	400
	0.04	50	$0.64/N_1$	0.02	1600
	0.06	50	$1.43/N_1$	0.02	3577
$e^{-\alpha|\eta|}\cos\beta\eta$	0.02	50	$0.32/N_1$	0.02	800
	0.04	50	$1.28/N_1$	0.02	3191
	0.06	50	$2.86/N_1$	0.02	7155

Table 5.12 Simplified results and integral lengthscales for the given approximations of K_u.

2D	$\frac{\sigma_u}{\mu_u}$	L_2 (mm^2)	ϵ^2	$\epsilon = \Rightarrow$	$N_1 \times N_2 = (\mathrm{mm}^2)$
$e^{-\alpha^2(\eta^2+\nu^2)}$	0.02	$(50)^2$	$16/N_1N_2$	0.02	$(200)^2$
	0.04	$(50)^2$	$64/N_1N_2$	0.02	$(400)^2$
	0.06	$(50)^2$	$143/N_1N_2$	0.02	$(600)^2$
$e^{-\alpha\lvert\eta\rvert-\beta\lvert\nu\rvert}$	0.02	$(50)^2$	$16/N_1N_2$	0.02	$(200)^2$
	0.04	$(50)^2$	$64/N_1N_2$	0.02	$(499)^2$
	0.06	$(50)^2$	$143/N_1N_2$	0.02	$(598)^2$
$e^{-\alpha(\eta^2+\nu^2)^{\frac{1}{2}}} \cos\beta(\eta^2+\nu^2)^{\frac{1}{2}}$	0.02	$(50)^2$	$66/N_1N_2$	0.02	$(406)^2$
	0.04	$(50)^2$	$114/N_1N_2$	0.02	$(534)^2$
	0.06	$(50)^2$	$193/N_1N_2$	0.02	$(695)^2$

As mentioned above, we find that the first two expressions are almost interchangeable in the limit for large sampling areas or lengths. The first approximation is chosen when the form the correlation coefficient is symmetric and Gaussian, the second if there is a significant difference in the lateral and transverse integral lengthscales, and the third if we have a flow situation where the correlation oscillates significantly about zero. As mentioned, for large sampling lengths/areas, no distinction is necessary between the two first, as none is necessary at all for very small sampling lengths/ areas.

Again we find that very large sampling lengths or areas are required if the error is required to be reduced, improving the accuracy.

5.5.3 Simplified results for longitudinal correlationfunction estimates.

In this case we find no useful results when we try to simplify the results, due to the form of the expression itself. As for the previous two cases, the mean square error is inversely proportional to the sampling length N_1. Furthermore we find that the mean square error seems to be dependent on a factor of the order $e^{-2\alpha x_1}$. It is worth remembering at this point that what we have found is the error when measuring $f(x_1)$, the longitudinal correlationfunction at x_1, that is for two points x_1 apart . It is therefore not surprising to find a dependency on x_1 in the result.

5.6 Inhomogeneous shear flows.

In the above we have assumed spatial stationarity with the added implication of homogeneity of the flow. If we do not have a homogeneous flow situation and therefore cannot assume spatial stationarity, an entirely different approach is called for.

Bendat and Piersol [16] states " A totally adequate methodology does not exist as yet for the analysis of all types of non-stationary data. This is partly due to the fact that a nonstationary conclusion is generally a negative statement specifying the lack of stationary properties, rather than defining the precise nature of the nonstationarity. On the other hand when a process is deemed stationary certain positive results are known to apply to all stationary data. Special techniques must be developed for stationary data which apply only to limited classes of these data".

Thus there is a very big difference between this situation and the calculations we performed for stationary (homogeneous) data. In the nonstationary case it would not be correct to state anything or estimate parameters from one single measurement. We could, for the sake of argument, ignore this and just apply the results for stationary flows relying on the spatial correlation that really does exist. We could then assume the results given in the tables in the preceeding sections would be correct for small N_1, N_2 but not for the necessary large sampling areas or lengths. Therefore we must sample several times, that is capture a succession of PIV measurements of the same flow situation. We could in theory sample at sufficient speed to be able to find the time correlation between the individual samples. In most cases, however, we must assume that the data points are not sampled at such a rate, and therefore are statistically independent. In the following we will only concern ourselves with trying to state something about calculating the mean velocity; no other parameters will be considered.

5.6.1 Mean velocity estimates.

For a spatial nonstationary process $\{u(x)\}$ statistical properties at any point x are not invariant with respect to translations in x. Suppose we have such a nonstationary process $\{u(x)\}$ and we sample K times, that is take K measurements. We will thus have K sample functions for any one point x:

$$u_i(x) \ : 0 \leq x \leq N, \ \ i = 1, 2, 3, \ldots, K$$

Now for a given point x we can compute the ensemble average of the mean.

$$\hat{\mu}_u(x) = \frac{1}{K} \sum_{i=1}^{K} u_i(x)$$

This estimate changes dependent on the samples we choose. As before, what we are interested in is finding how the estimate differs from the true mean value μ_u. The expected value of the estimate is

$$E[\hat{\mu}_u(x)] = \frac{1}{K}\sum_{i=1}^{K} E[u_i(x)] = \mu_u$$

Thus we have an unbiased estimate of μ_u for all x, independent of K. And as we have assumed that the K sample functions are statistically independent, the error in estimating $\mu_u(x)$ by $\hat{\mu}_u(x)$ is equal to the variance of $\hat{\mu}_u(x)$.

$$var[\hat{\mu}_u(x)] = E[\{\hat{\mu}_u(x) - \mu_u(x)\}^2]$$

Note that $var|\hat{\mu}_u(x)] = \sigma^2_{\bar{u}}$ and $var[u_i(x)] = \sigma^2_u$.
Thus we find in the expression for the error:

$$\begin{aligned} var[\hat{\mu}_u(x)] &= var\left[\frac{1}{K}\sum_{i=1}^{K} u_i(x)\right] \\ &= \frac{1}{K^2} var\left[\sum_{i=1}^{K} u_i(x)\right] \\ &= \frac{1}{K^2}\sum_{i=1}^{K}\sigma^2_u \\ &= \frac{\sigma^2_u}{K} \end{aligned}$$

In the above we have used the fact that $var[ax] = a^2 var[x]$. Thus we find the error in estimating the mean to be equal to the variance and:

$$var[\hat{\mu}_u(x)] = \sigma^2_{\bar{u}} = \frac{\sigma^2_u}{K} \tag{5.26}$$

As we see the sample variance approaches zero as K approaches infinity, so we find that $\hat{\mu}_u(x)$ is a consistent estimate of $\mu_u(x)$ for all x.
Even though we might not know the exact probability distribution of the estimate of the mean, we are , given the above, still able to predict the range of results for a given value of x. We use the Tchebycheff Inequality for Unknown Distribution. This takes several forms:

$$Prob[\ |\hat{\mu}_u(x) - \mu_u| \leq c\sigma_{\hat{\mu}_u}] \geq 1 - \frac{1}{c^2}$$

$$Prob[\ |\hat{\mu}_u(x) - \mu_u] \geq c\sigma_{\hat{\mu}_u}] \leq \frac{1}{c^2}$$

Although we by no means are able to give such detailed forms of the error involved when estimating the mean for the nonstationary case as we were for the stationary case, it is clear that we are able to predict something about the number of samples required in order to find the estimate within a certain inteval round the true mean. The larger the number of samples, the greater the certainty that the true value is included. In the case where $u(x)$ follows a Gaussian distribution, the probability described above takes on a different form. Generally speaking it gives greater certainty that the true value is included than would be expected in the equations above.

If we choose $c = 5$ in the above expression, we find that there is 95% certainty that the estimate is within $\frac{5\sigma_u}{\sqrt{K}}$ of the true value. We can then adjust the number of samples K to make this 'error' as small as we desire.

Chapter 6

PIV applied to turbulent flows

In this chapter we present the results from PIV measurements on homogeneous, isotropic, grid turbulence in air and water. Originally, the measurements were performed in order to provide a suitable database for verification of the theoretical predictions presented in the preceeding chapter. However, as we found the results to be of very good quality, we decided to investigate the performance of the technique as a measurement tool for turbulent flows. Several authors have applied PIV to turbulent or other types of complex flows [6, 50, 51, 54, 55, 69, 70, 87]. Staying with the trend, we have investigated the resolution obtained and compared this with the relevant turbulent length scales of the given flow and coherent structure theories. Homogeneous and near-isotropic turbulence is most easily generated in the laboratory by passing air through a mesh or grid [19]. The isotropic turbulence is superimposed on a mean flow, thus we have to subtract the mean velocity in order to investigate the homogeneous isotropic structure.

6.1 PIV applied to grid turbulence in air.

The first set of experiments are for homogeneous isotropic grid turbulence in air. We used apparatus originally designed for experiments on particle roping [59]. After slight modifications it proved well suited to experiments on the turbulent background flow itself.

6.1.1 Experimental set-up.

To generate the flow a windtunnel-type arrangement was used. This is essentially a miniature windtunnel, designed to the same rules as larger size windtunnels, Figure 6.1 shows a photograph of the windtunnel and experimental set-up. Figure 6.2 is a schematic diagram of the same.

Air from the fan is monitored by a pitot-static tube before entering the windtunnel. In the windtunnel the air passes through a series of mesh screens followed by settling chambers, the last settling chamber being longer than the others. These

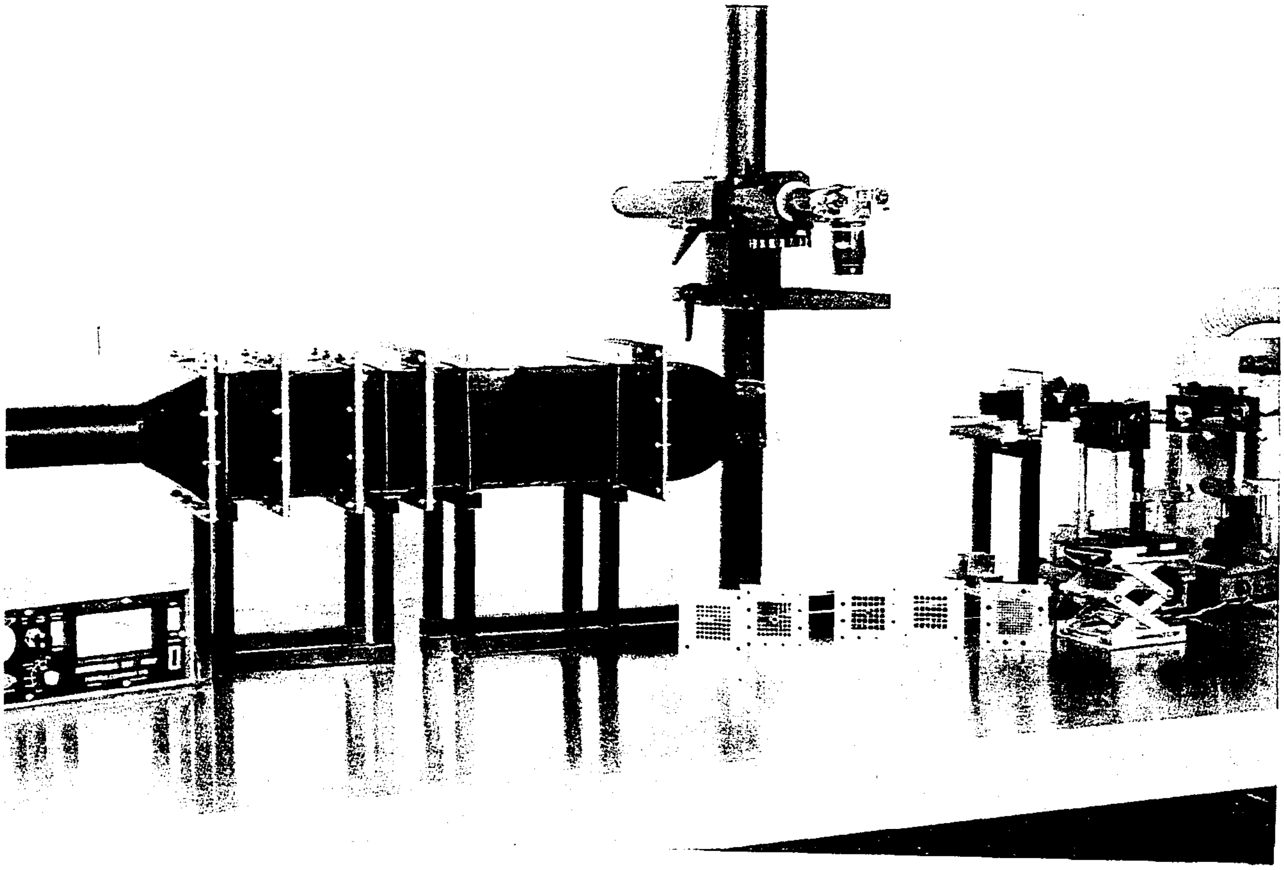

Figure 6.1: The miniature windtunnel.

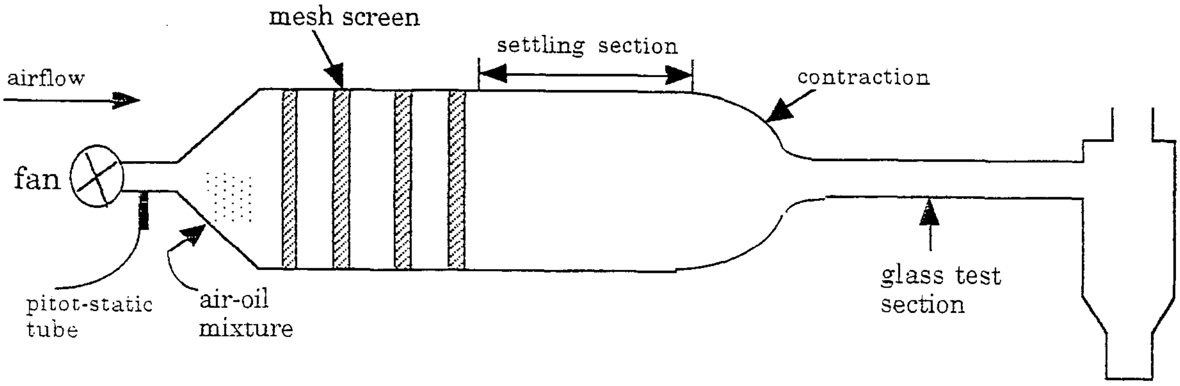

Figure 6.2: A schematic diagram of the windtunnel experimental set-up.

screens and settling chambers help to smoothe the airflow, reducing the background turbulence level. After the final settling chamber the air passes through a contaction having an area ratio of 12:1 and enters the glass test section which has a 52mm square cross-section. LDA measurements in the test section show that the above experimental set-up produces a uniform flow with a background turbulence level of less than 1% [60]. The mean velocity in the test section, relative to the setting of the fan, has been determined using pitot-static and LDA measurements.

Two different turbulence-generating grids were employed, both square rod, square meshes. Grid I has grid diameter $d = 2.44$mm and grid spacing $M = 8.41$mm, giving a solidity of $\sigma = 0.496$, where:

$\sigma = d/M(2 - d/M)$

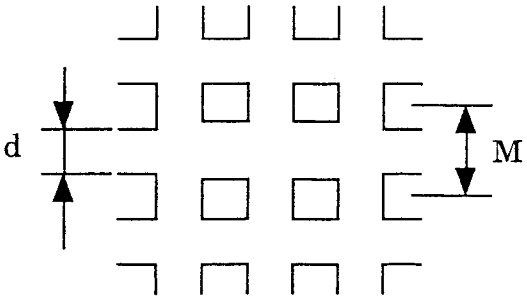

LDA measurements found the rms turbulence level $\frac{u'}{U}$ to be 6.2%. Grid II has grid diameter $d = 2$mm and grid spacing $M = 2$ mm resulting in a solidity of $\sigma = 1$. For grid II, LDA measurements found the turbulent intensity to be 9%. Both grids were verified as producing isotropic turbulence at a distance of 20 mesh diameters or more from the grid and at this distance the flow is assumed to be fully developed [59]. The design of the grids were found in [19], and on application it was found that the grids reflected a significant amount of light, so subsequently they were painted black in order to avoid problems with optical interference.

The flow was seeded with corn oil droplets using a Dantec Type 55L17 seeding generator. The oil droplets have a mean particle diameter of 1μm.

Measurements were performed for mean flow speeds of 1m/s and 2m/s. Results from both sets of experiments are presented here, but the theoretical verification and evaluations are concentrated on the 2 m/s mean velocity measurements for grid I. The Reynolds number for the measurements based on the grid spacing M, and mean velocity $\overline{u}$ is:

$\overline{U}$	GRID I	Grid II
1 m/s	R = 561	R = 133
2 m/s	R = 1121	R = 267

The camera, a Nikon F801 autofocus with a AF Micro-Nikkor 60 mm lens, was mounted horizontically over the glass test section at a distance giving a magnification of 0.5. Figure 6.3 shows the mounted camera.

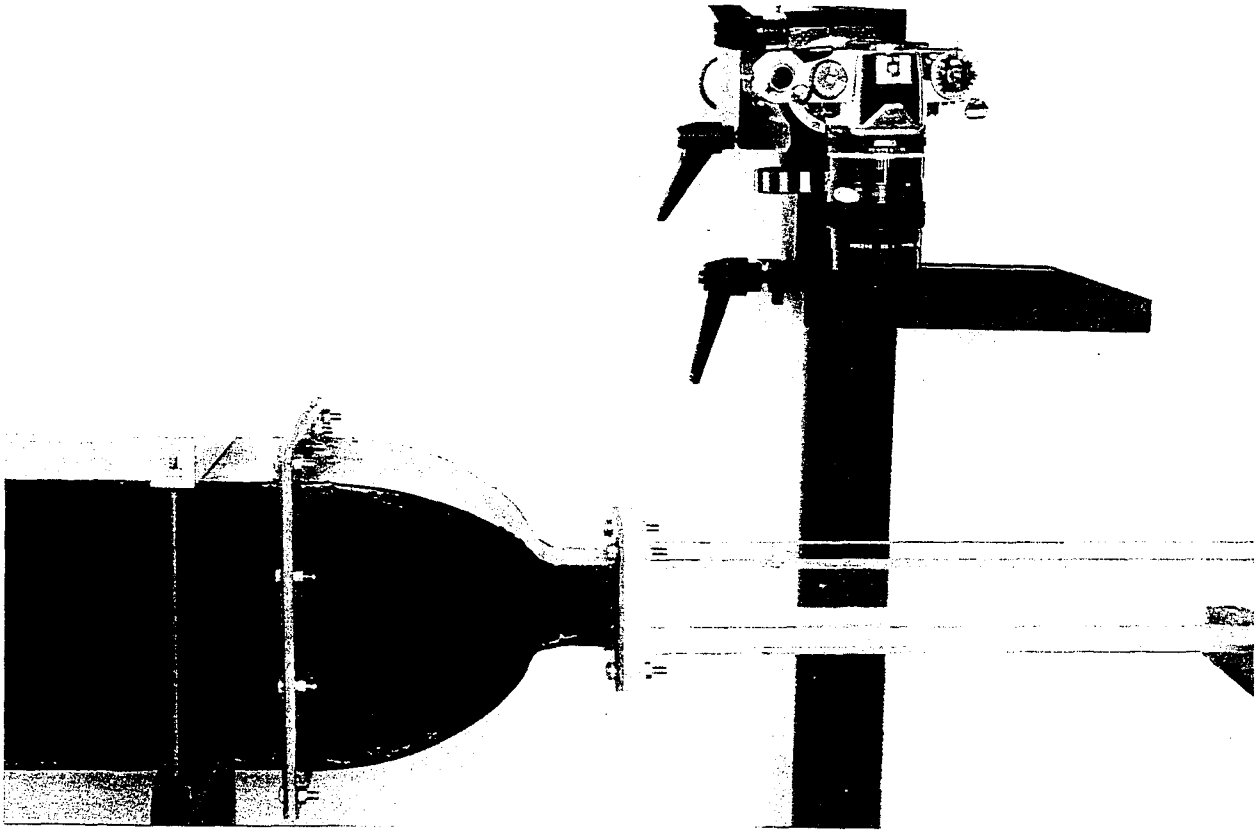

Figure 6.3: The glass test section with the camera mount.

The flow was recorded 130-200mm from the grid for grid I. which equals 65-100 mesh diameters, and at 180-250mm equal to 21-30 mesh diameters for grid II. At 20+ mesh diameters downstream a fully developed flow is expected.

For illumination we a scanning beam system [34]was used, employing an 18-sided mirror and a 15 Watt Argon-ion laser with radiation in the blue-green range,wavelength 400-530 nm. In all the measurements the laser was used at full power that is 15 Watt. Figure 6.4 shows the illumination and the apparatus used for a particle roping experiment(courtesy of Dr. McCluskey).

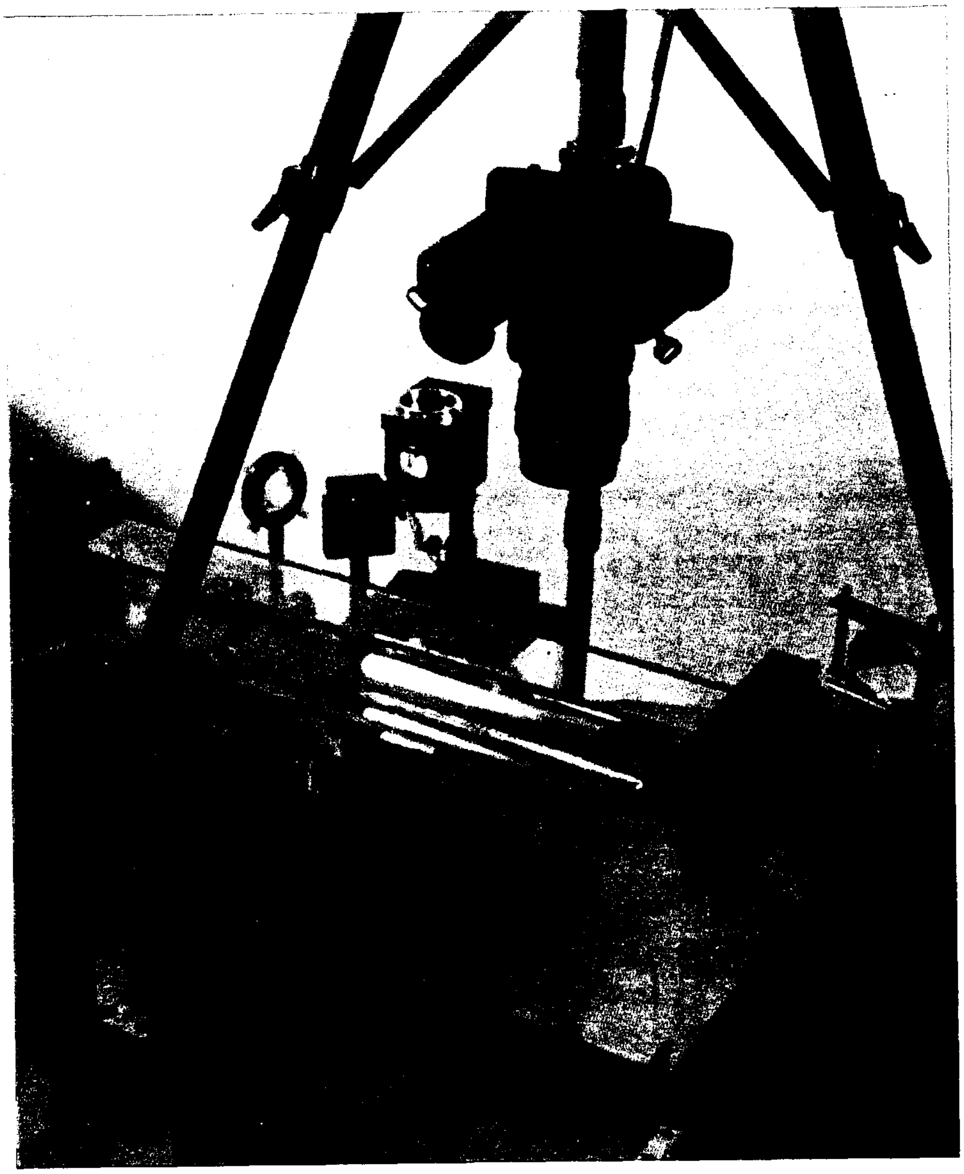

Figure 6.4: Illuminating equipment as used for a particle roping measurement (Courtesy of Dr. D.R.McCluskey).

The film used was a Kodak Tmax 400 with a resolution of 100 lines/mm. As seen in Chapter 3, the image diameter on the film is given by Adrian [3] as;

$$d_i = \left(M^2 d_p^2 + d_{spot}^2 + d_r^2\right)^{1/2}$$

Where:

d_p is the seeding particle diameter (here 1μ).

d_{spot} is the diffraction limited spot diameter of the optical system, which is given by:

$d_{spot} = 2.44(1 + M) f_{no} \lambda_f$,

where λ_f is the wavelength of the illuminating light source.

d_r is the point spread function for the film emulsion and may be approximated by the width of a line which is just resolved.

For this experiment we have: $M = 0.5$, $\lambda_f \simeq 500nm$, $f_{no} = 4 - 8$, $d_r = 10\mu$ and $d_p = 1\mu$.

This gives the result $d_i = 12.4\mu - 17.7\mu$ which is sufficient for the individual particle images to be resolved on the film.

Since an 18-sided mirror was employed there was a choice of scanning speeds from 300 Hz to 650 Hz, corresponding to scanning times between 85.5μs -185 μs. In accordance with recommandations put forward by [47,48,49] amongst others, we would aim for a particle image separation on the film of less than 0.25 times the analysis beam diameter.

An example: For a flow with a mean velocity of 2m/s, and a scanning speed of 350 Hz, the scanning time is 158.7 μs, resulting in a particle image separation of approximately 0.16mm. As we have an analysis beam diameter of 1mm this is within the recommended range. We then set the shutter speed to 1/1000 giving us 6 exposures per negative.

Several measurements were performed for the individual flows and 30 selected for further analysis. A typical example of a PIV negative from these measurements is found in Figure 6.5.

The PIV analysis system was the fully automated Youngs fringes system described in Chapter 4. As mentioned above the analysis beam was circular with a diameter of 1mm. A region of 20mm × 30mm was analysed in 0.5mm steps for each negative, resulting in vector plots with around 2500 vectors. The overlap in interrogation regions will result in a smoothing of the vector values as part of the particle images used in determining the velocity at one point will also be included in the analysis of neighbouring points. However, since the interrogating beam has a Gaussian intensity profile, it is found that the overlapping regions are less significant, and the possible error reduces similarily.

The vector plots was filtered to leave values with unacceptably low visibility out, and the mean velocity was subtracted to reveal the underlying turbulent structure. The visibility in this case is defined as the ratio of the amplitude of the displacement peak to the amplitude of the underlying noise.

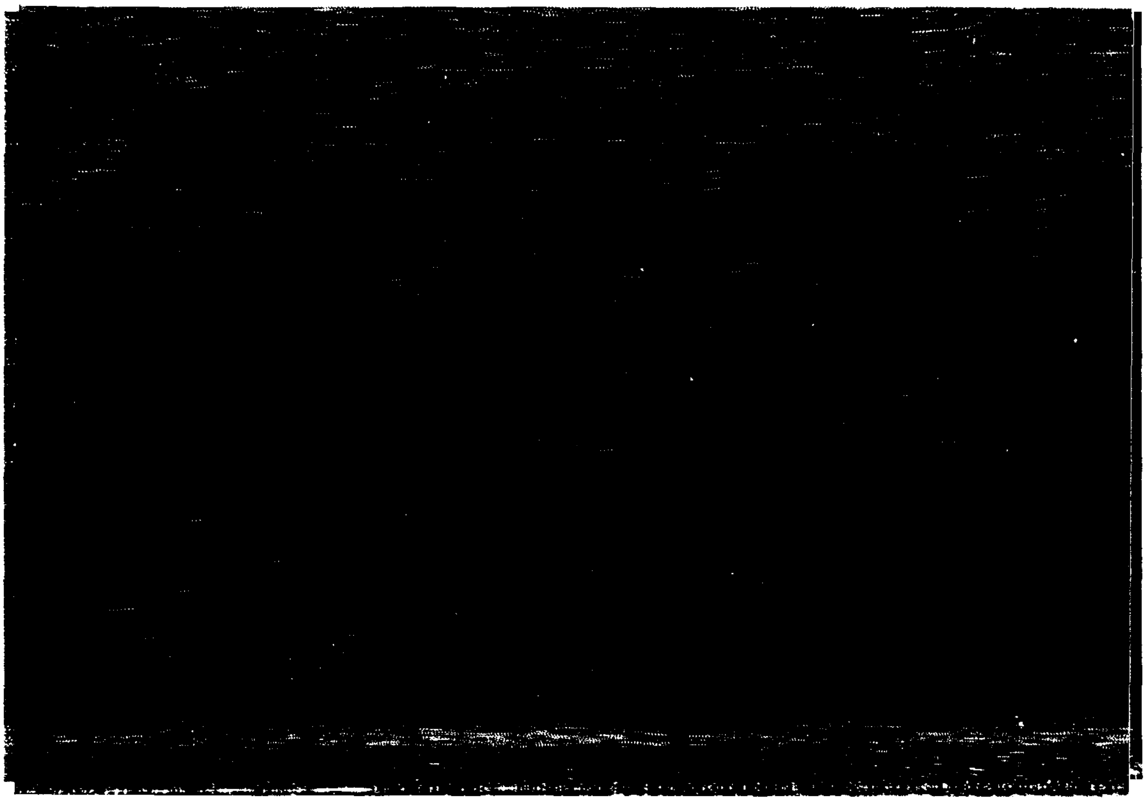

Figure 6.5: A typical PIV negative from measurements on grid turbulence in air.

6.1.2 Results.

An example of an enlargement of an actual PIV negative from the measurements desribed above is found in Figure 6.5.
The negative is from a 35mm film and thus measures 25mm x 35mm. It may seem as if this negative would hardly be analysable, but it is very representable of the type of PIV negative we would get from this experimental set-up, and is in fact of good quality. Figure 6.6 shows a typical resulting vector velocity plot of the instantaneous turbulent flow field in two dimensions. We have to bear in mind that in reality it is a two-dimensional slice of a three dimensional field.

This particular result is for a 1m/s mean flow and 9% level of turbulence (grid II). The values with lowest visibility have been removed; generally the drop-out rate is low, a line in the top left corner and a few single points, in all less than 5%. When the mean velocity has been subtracted the turbulent structure become quite clear. We find several types of larger structures. Figure 6.7 shows an enlargement of a part of the preceeding plot. Here it is very striking, that if nothing else, PIV is an excellent flow visualization tool. We find two eddies, one rotating clockwise and one counterclockwise, we also find a sink in the flow which

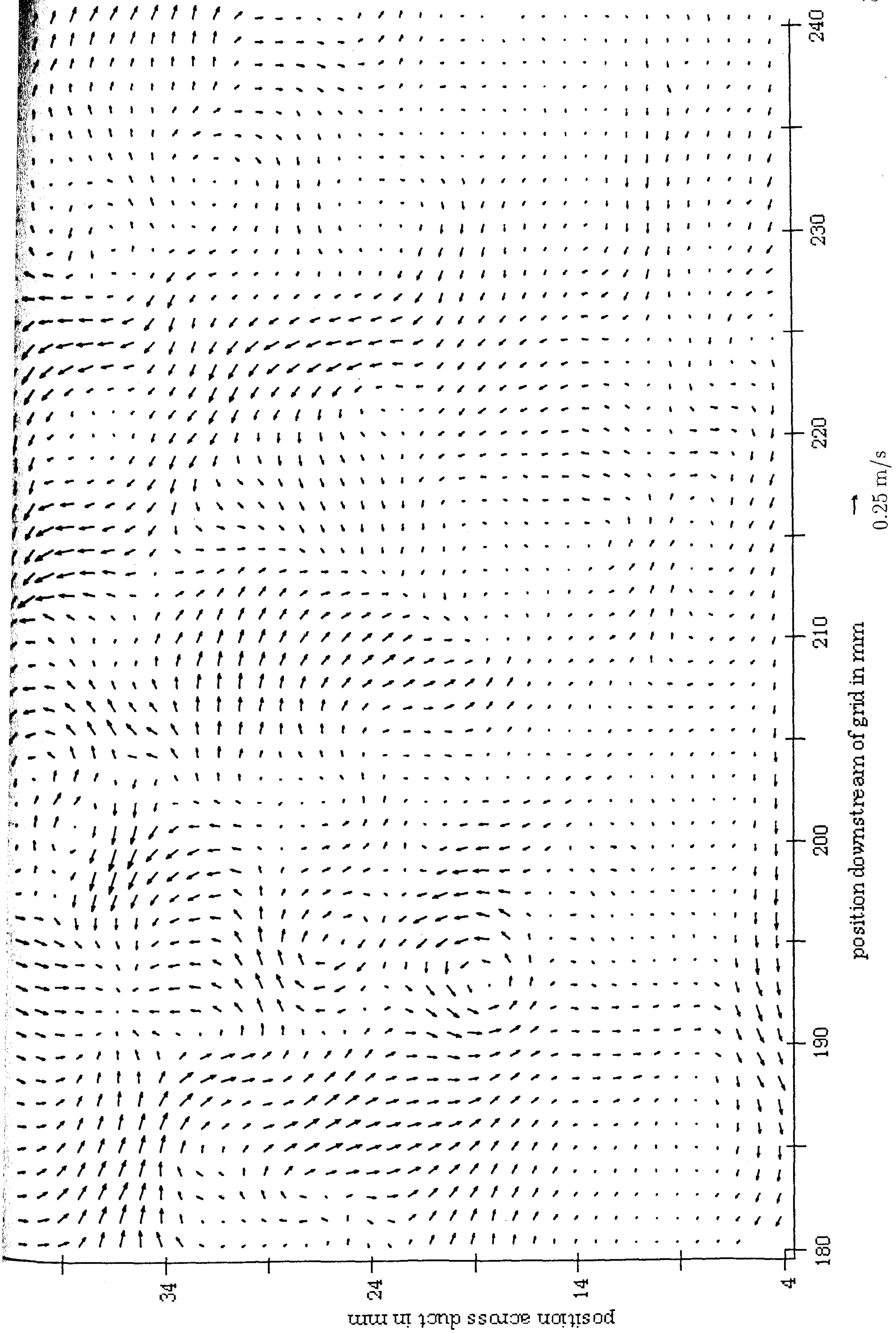

Figure 6.6: A vector velocity plot for grid turbulence with an rms turbulence level of typically 9% with the mean velocity of 1m/s subtracted.

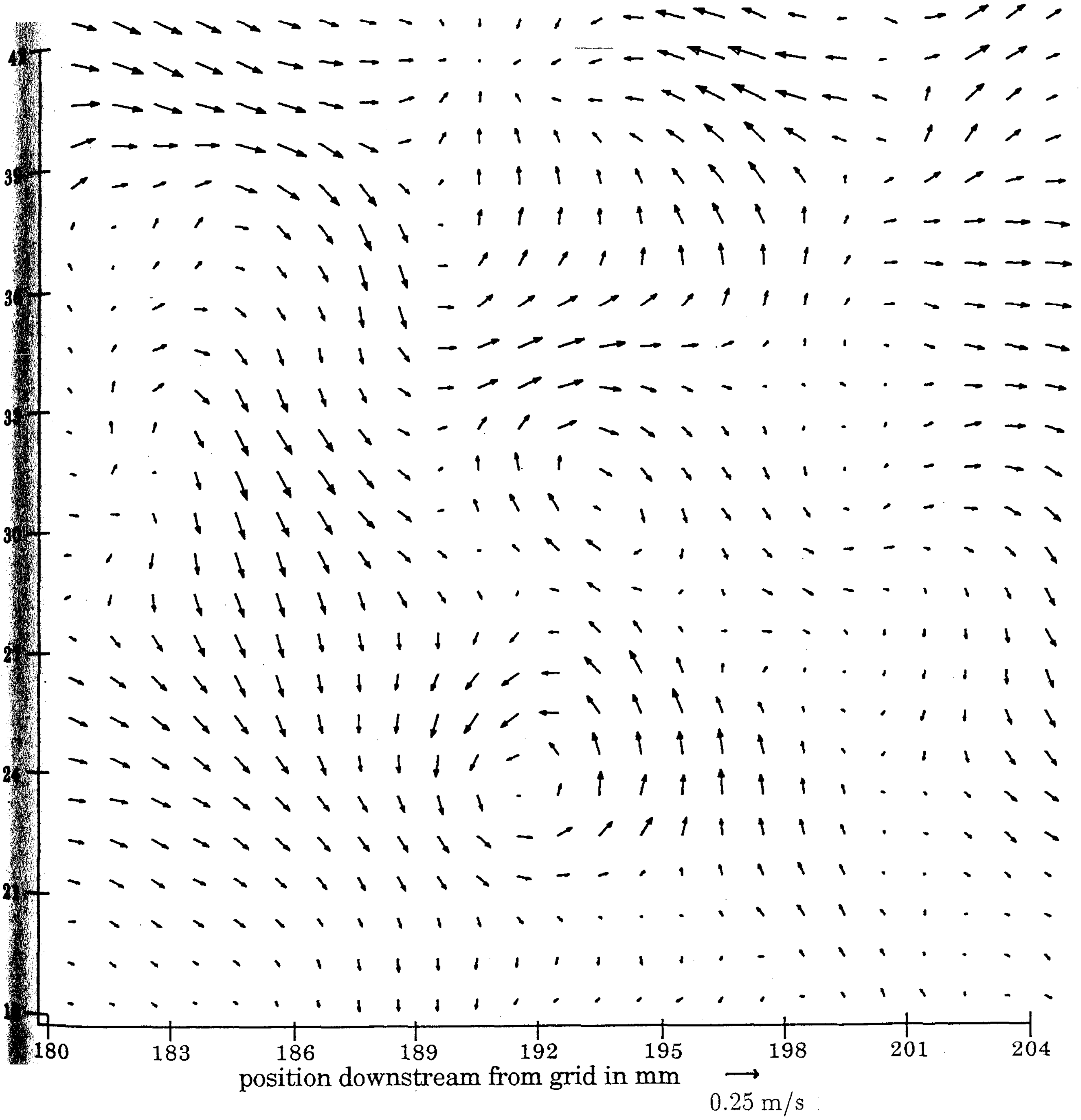

Figure 6.7: Enlargement of an area of Figure 6.6.

adds a sense of three dimensionality to the map. When we consider the fact that these results are the product of analysing a PIV negative in 0.5mm steps, with a magnification of 0.5, we find that there is 1mm spacing between each vector in the flow plane. This is indeed a very good resolution. The eddies in Figure 6.7 are thus 5-6mm in diameter and structures down to the size of 2-3mm are clearly resolved. This type of result proves that PIV is a very versatile flow measurement technique; not only can it be succesfully applied to a very complex flow regime, it also produces velocity maps with high resolution. Furthermore is has coped with the wide range of velocities in the flow, which again corresponds to a good dynamic range.

As mentioned above, we have for the largest part concentrated the theoretical analysis of the results on the measurements of 2m/s mean flow and grid I generating a turbulence level of about 6 %. Figure 6.8 - 6.10 shows an example of these results, starting with the actual resulting planar instantaneous velocity map. Figure 6.9 shows the vector velocity map after removal of spurious vectors and subtraction of the mean velocity. Figure 6.10 shows the corresponding vorticity plot. The overall quality and resolution of these results are exactly the same as for the ones presented above. Examples of larger turbulent structures, such as eddies, are framed by boxes and again we find that even the smaller structures of 2-3mm in diameter are resolved.
The spanwise vorticity is defined in Chapter 2 as;

$$\vec{\omega} = curl\ \vec{u} \Rightarrow \omega_z = \frac{\partial v}{\partial x} - \frac{\partial u}{\partial y}$$

This vorticity is related to the rotational part of the fluid motion [77]. In accordance with this, the areas of strongest vorticity are found to correspond to areas, in the velocity map, with a large velocity gradient, such as eddies and other types of swirling motion. This is in agreement with results presented by, amongst others Adrian, Reuss and Liu [6,8,54,69,70]. These areas are thus perhaps most precisely identified from a vorticity plot.

6.1.3 Correlation.

For this and subsequent analysis a total number of 12 frames were selected, this giving a total of approximately 30.000 vector velocity values. The correlation function $R_u(\underline{r})$ can be found from the longitudinal and transverse correlation functions $f(\underline{r})$ and $g(\underline{r})$ [11,12]. Hence it is sufficient to investigate these two two-dimensional cases when we wish to establish the form of the curve of the correlation coefficient. The correlation functions $f(\underline{r})$ and $g(\underline{r})$ were calculated for each line in the vector velocity maps, a total of 240 lines, and the general form of these curves could thus be established.

Figure 6.11 and 6.11 show $f(\underline{r})$ and $g(\underline{r})$ respectively, for homogeneous isotropic grid turbulence, decaying from 6% and with a mean velocity of 2m/s. The shapes of these curves are in good agreement with numerous other results from the same

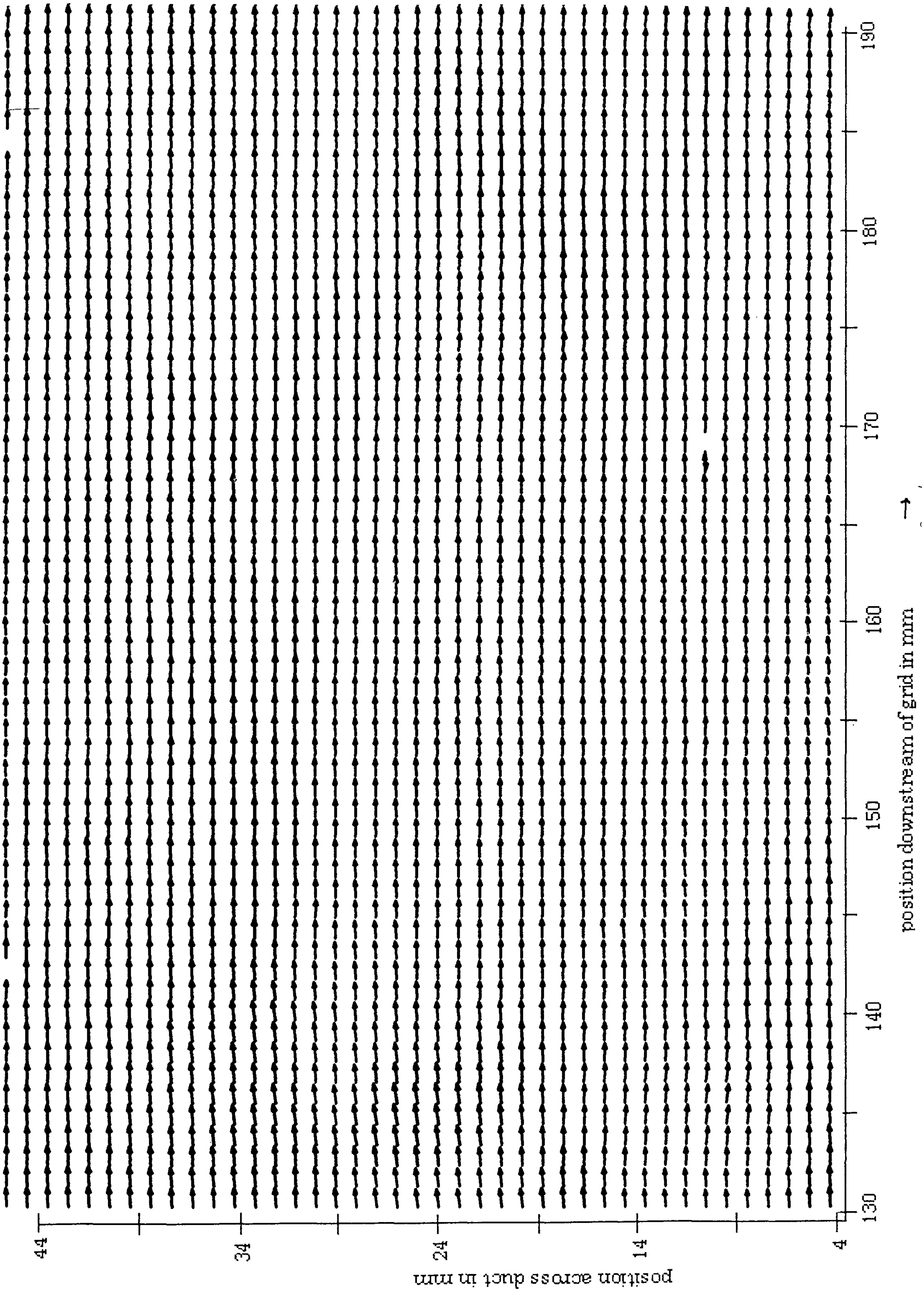

Figure 6.8: Vector velocityplot of 6 % grid turbulence in air.

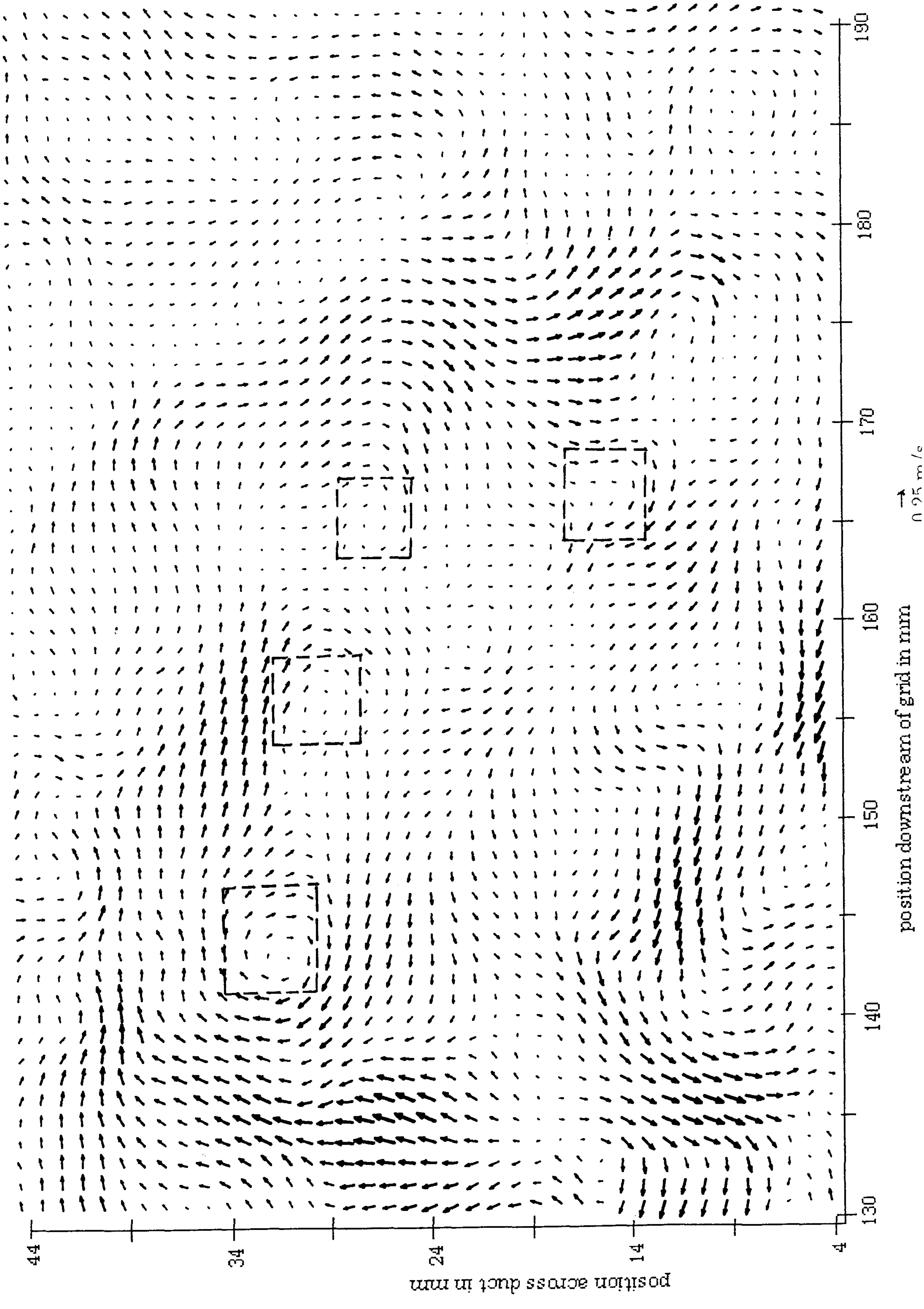

Figure 6.9: Vector velocityplot of Figure 6.8 with mean velocity subtracted.

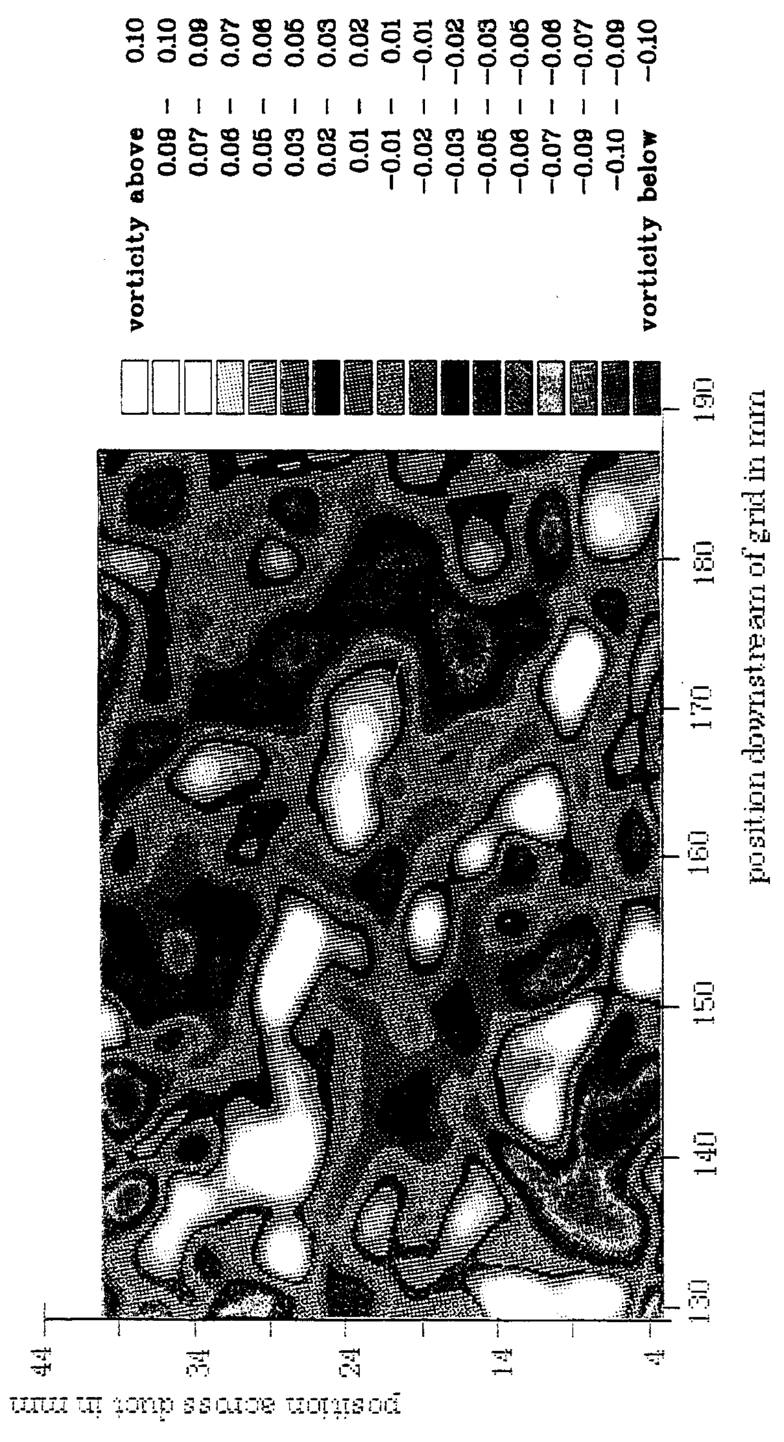

Figure 6.10: Vorticityplot of the flow field shown in Figure 6.8.

type of flow, starting with the correlation 1 for $r = 0$ and then decreasing rapidly tending towards zero as r approaches infinity.

As stated by Tritton [77] it is possible to infer further facts about the flow from just the mere shape of the curve of the correlation coefficients. According to this Figure 6.11 and 6.12 could indeed correspond to isotropic turbulence with a wide spectrum of eddies, which is exactly what is expected from the fully developed flow we have investigated. There appears to be a slight overweight of eddies of one particular size within the spectrum, accounting for the 'bump' on the curves around $3\times M$, M being the grid spacing, also masking the expected negative part of $g(\underline{r})$. Investigation of the vorticity plot does not reveal any obvious structures with correlation of this length. There are however connected strings of structures which might account for this small deviation. Disregarding this small aberration, there is no significant correlation left after approximately 15mm, which is about twice the grid spacing M.

6.1.4 Length scales

As described above it has already been established that for this flow regime, structures down to the size of 2-3mm in diameter, are clearly resolved by the PIV technique. It is of interest to compare this to the standard turbulent length scales inherent to the flow . For this it is necessary to calculate the turbulent Reynolds number R_t. For comparison we do this based on the LDA measurement results for the flow, which we for the time being assume are the more accurate.

> Actually the quantitative velocity information obtained using the PIV technique is similar to and, as accumulated evidence suggests, as accurate as that obtained from LDA measurements. One demonstration of this is for example; for the measurements described above, the mean flow velocity was found to be 1.968 m/s and the rms turbulent intensity 6.6 %. LDA measurements of the same flow area, found the mean velocity to be 2 m/s and the turbulence intensity 6.2% [60].

The turbulent Reynolds number R_t is defined in terms of the rms fluctuating velocity component u', found from LDA measurements and a length scale l_e, which is comparative to the average size of the energy containing eddies; in our case the grid spacing M is a suitable choice for l_e. From this we find;

$$R_t = \frac{u' l_e}{\nu} = 70$$

Using the standard relationship between R_t, Taylors microscale λ and The Kolmogorov microscale η:

$$\lambda / l_e \simeq \sqrt{15/R_t}; \quad \lambda/\eta \simeq (225 R_t)^{1/4}$$

λ is found to have the value 3.89mm and from this η is estimated as 0.347mm.

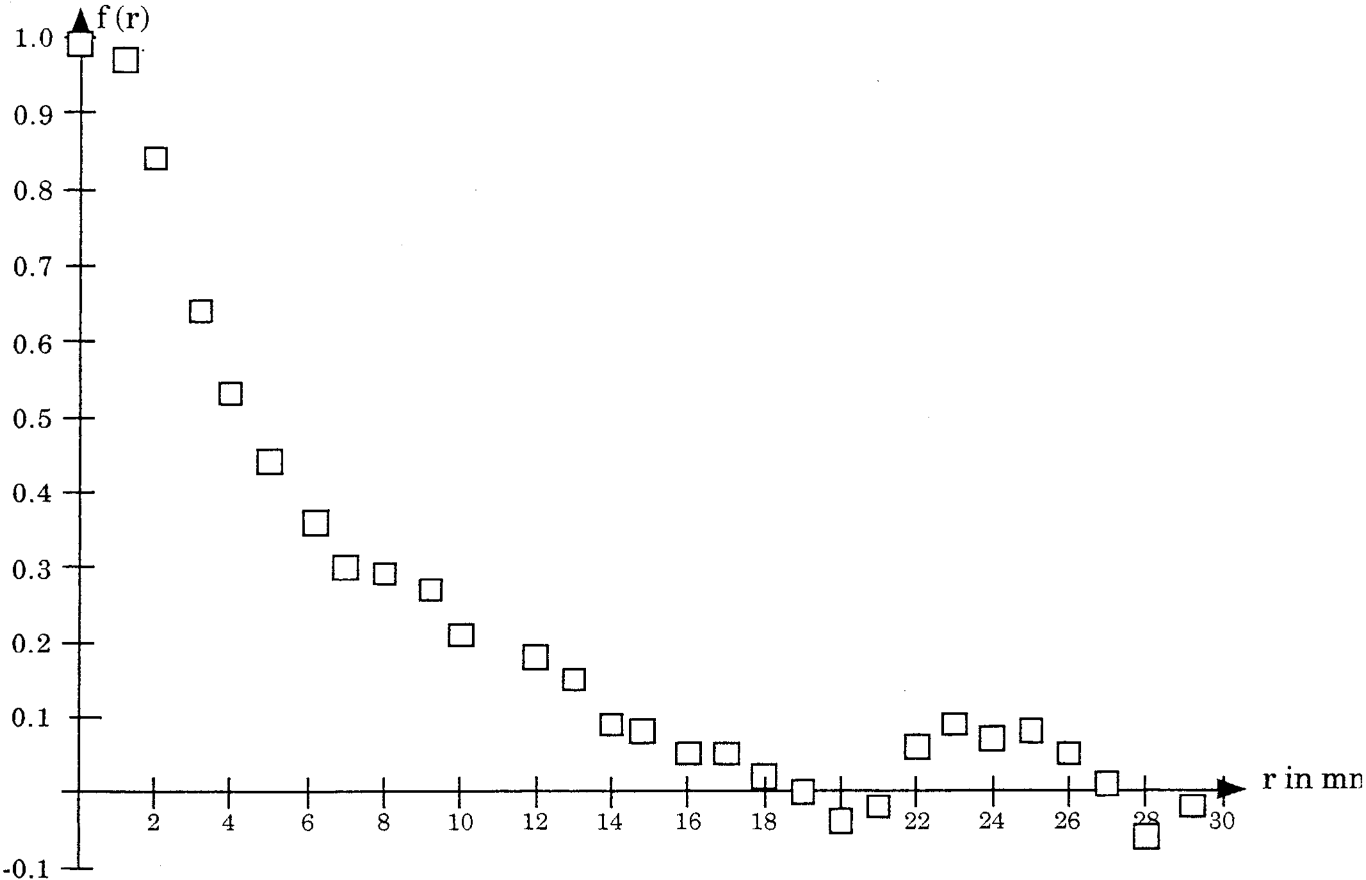

Figure 6.11: The longitudinal correlation function $f(r)$ for grid turbulence in air.

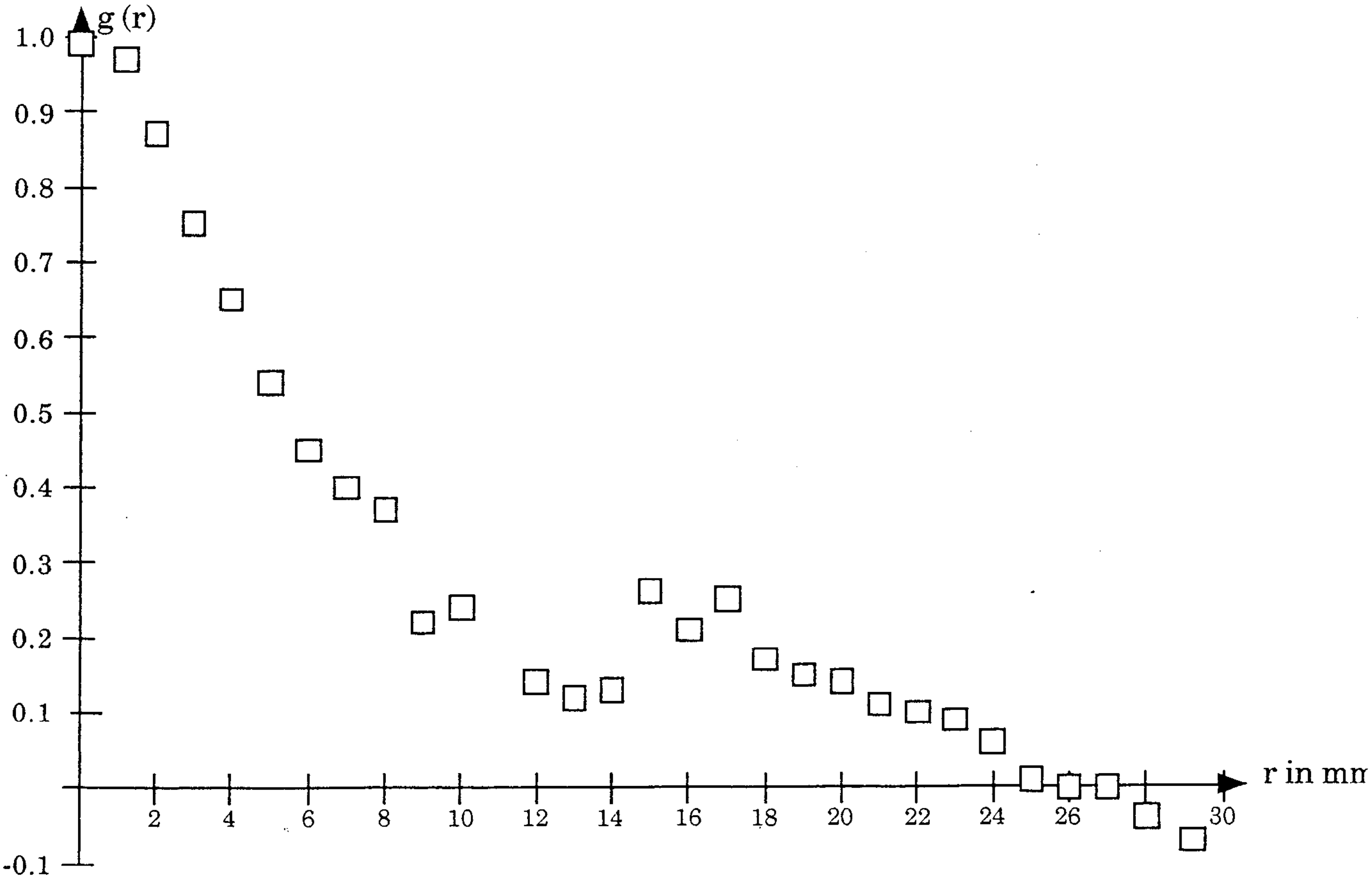

Figure 6.12: The transverse correlation function $g(r)$ for grid turbulence in air.

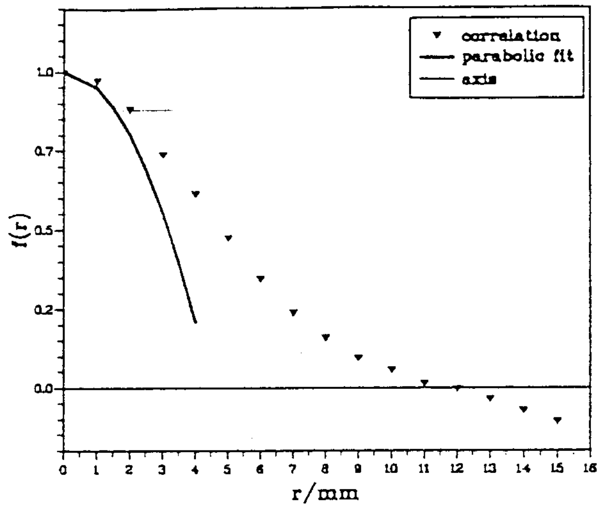

Figure 6.13: An osculating parabola fitted to the curve of the correlation function.

It is thus clear that structures of a size comparable to Taylors microscale are clearly resolved. This should also be a minimum requirement of the technique, as this length scale is representative of the average dimension of the eddies mainly responsible for dissipation.
Structures down to the size comparable to η are however not resolved by the system in this case.

As a measure of the accuracy of the PIV technique we compare the above value of λ (and thus η) found from LDA measurements, with estimates of the same found from the PIV results.
An estimate of Taylors scale λ can be found by fitting an osculating parabola to the curve of the correlation function as seen in Figure 6.13 . The intersection between this parabola and the x-axis can be taken as λ [75]. In our case this procedure yields the value $\lambda = 4.47mm$ in reasonable accordance with the value obtained from LDA.
The integral length scale L, as we have defined it in the previous chapters, should not be confused with the length scale l_e defined above. L is a measure of the length over which some sort of correlation persists, and is defined in terms of the correlation coefficient whereas l_e is a measure of the average size of the largest energy containing eddies and is smaller than L, but of the same order of magnitude.

6.1.5 Coherent structures.

In Chapter 2 we introduced the various definitions and realisations of coherent structures. At least two of the definitions, Mumford and Hussain [44, 45, 62, 63] concur with what we might term as an intuitive perception of coherent structures. Hussain, which as perhaps the most widely accepted definition, describes coherent structures in terms of the spatial extend of instantaneous phase correlated vorticity. These lumps of correlated vorticity can be identified from the vorticity plot (Figure 6.10) and can to a very large extent be associated with the coherent structures as defined by Mumford. Mumford defines coherent structures in terms of identifiable large scale velocity patterns as the ones emphasized in Figure 6.9, and we thus find that these PIV experiments produce results which make identification of coherent structures according to the above two definitions possible.

Furthermore, Westerweel [83] has succesfully subjected results from the experiment described above to analysis according to the definitions put forward by Hunt et. al. The conclusion must be that PIV as a measurement technique is capable, not only of resolving turbulent structures down to a size less than Taylors microscale, but also of giving valueable information regarding the overlying large scale coherent structures.

6.1.6 Comparison with Digital PIV,(DPIV).

Results from the experimental set-up described above has also formed the database for a comparison between Digital PIV (DPIV) and the Young fringes analysis method described in Chapter 3 and 4 [84]. It was found that both techniques are able to detect the same large scale structures and that the main differences were to be found in accuracy and resolution. At the time DPIV was found to be less accurate and have less resolution than the method employed above. In this comparison, however, DPIV analysis was significantly faster than the more conventional technique. Speed is one of the features of DPIV which will probably make it the PIV analysis method of the future. The inferior accuracy and resolution is imposed by a technology which is advancing rapidly.

6.1.7 Verification of theoretical results.

As mentioned in the beginning of this chapter, the main purpose for performing these measurements of turbulent flows, was to accumulate enough data for verification of the theoretical results presented in chapter 5. These theoretical results were presented for mean velocity estimates and mean square estimates, and it was found that certain parameters were common to all results.

One such significant parameter is the integral lengthscale L_1 or L_2. In this case for homogeneous isotropic grid turbulence, we would estimate that the velocities are virtually decorrelated at a separation of approximately $2 \times M$, where M is the grid spacing. This would in turn correspond to the one and two-dimensional integral lengthscale having the values:

$$L_1 = 16mm, \qquad L_2 = 256mm^2$$

If we relate this to the correlationfunctions $f(r)$ and $g(r)$ in Figure 6.11 and 6.12, it is found that for $r = 16mm$, $f(r)$ has dropped to less than 10% of its value at the origin, and $g(r)$ is less than 20 % of $g(0)$. From this the immediate impression is that $2 \times M$ is a reasonable estimate of the integral lengthscale. In the following we will try to establish more firmly whether this is the correct choice of L for these measurements and calculations.

Another significant parameter is the rms turbulence level for the flow, $\frac{\sigma}{\mu}$. From this set of experiments the value was found to be:

$$\frac{\sigma}{\mu} = 0.0659$$

As we have evaluated the mean square error MSE and the normalized standard error ϵ for various forms of the correlation coefficient K_u, we should also establish the general shape of the curve of the correlation coefficient for this particular experimental set-up.
The relationship is [12]:

$$R_{ij}(\underline{r}) = u'^2 \left(\frac{f-g}{r^2} r_i r_j + g \delta_{ij} \right)$$

from which it is possible to determine R_u, and thus K_u, from the one-dimensional correlation curves of $f(r)$ and $g(r)$.
Simple observation of the shape of the curves for $f(r)$ and $g(r)$, however, gives clues as to which of the three possible approximations for $K_u(\underline{r})$, is closest to the curve for the flow in question.
There is no significant oscillation present and the narrowness and similarity of the two curves suggests that it is the approximation

$$K_u(\eta, \nu) = e^{-\alpha^2(\eta^2+\nu^2)}$$

that best describes the curve of the correlation coefficient for this particular flow. Naturally this need not be considered when we are concerned with the simplified results for mean value estimates as these were independent approximations for K_u. For the error involved when estimating the mean square value, however, it is necessary to consider the shape of the curve of the correlation coefficient.

For the agreed approximation of the correlation curve, the simplified results for the error when estimating the mean and mean square value over a finite area $N_1 \times N_2$, were:

$$\boxed{\boldsymbol{K_u(\eta,\nu)} = e^{-\alpha^2(\eta^3+\nu^2)}}$$

Mean value estimates

Small sampling areas: $\epsilon^2 = \frac{\sigma_u^2}{\mu_u^2}$

Large sampling areas: $\epsilon^2 = \frac{L_2}{N_1 N_2}\frac{\sigma_u^2}{\mu_u^2}$

Mean square estimates

Small sampling areas: $\epsilon^2 = \frac{2\left(1+\frac{2\mu_u^2}{\sigma_u^2}\right)}{\left(1+\frac{\mu_u^2}{\sigma_u^2}\right)^2}$

Large sampling areas. $\epsilon^2 = \frac{4L_2\left(1+\frac{4\mu_u^2}{\sigma_u^2}\right)}{N_1 N_2\left(1+\frac{\mu_u^2}{\sigma_u^2}\right)^2}$

When comparing the above predictions with calculations from the PIV results, the following method was employed:

Method: A total of 12 frames were selected, each covering an area of 2400 mm^2 of the flow plane. These were treated as one large area covering a total of 28.000 mm^2. The frames were divided into subareas and the mean velocity and mean square value calculated for each individual area. The mean square error was then calculated according to the basic definition in (5.1) and (5.15).

$$MSE = var[\hat{\mu}_u] = E[(\hat{\mu}_u - \mu_u)^2] = E[\hat{\mu}_u^2] - \mu_u^2$$

$$MSE = var[\hat{\psi}_u^2] = E[(\hat{\psi}_u^2 - \psi_u^2)^2] = E[\hat{\psi}_u^4] - \psi_u^4$$

From this the normalized standard error ϵ is obtained. The true mean μ_u and mean square ψ_u^2 are found by calculating both these values over the total area of 28.000 mm^2.

Table 6.1 and Figure 6.14 display the normalized standard error ϵ for mean value estimates over the area $N_1 \times N_2$, in a homogenous near-isotropic flow regime with a two-dimensional integral lengthscale of $L_2 = 256mm^2$.

Table 6.1 Mean value estimates for grid turbulence in air.

Sampling area $N_1 \times N_2$ (mm^2)	ϵ_t estimated from theory	ϵ_c calculated from PIV results
300	0.122	0.042
600	0.086	0.040
1200	0.061	0.037
1800	0.049	0.033
2400	0.043	0.032
3000	0.038	0.022
3600	0.035	0.025
4200	0.032	0.022
4800	0.030	0.020
Small sampling areas $\epsilon = 0.066$		

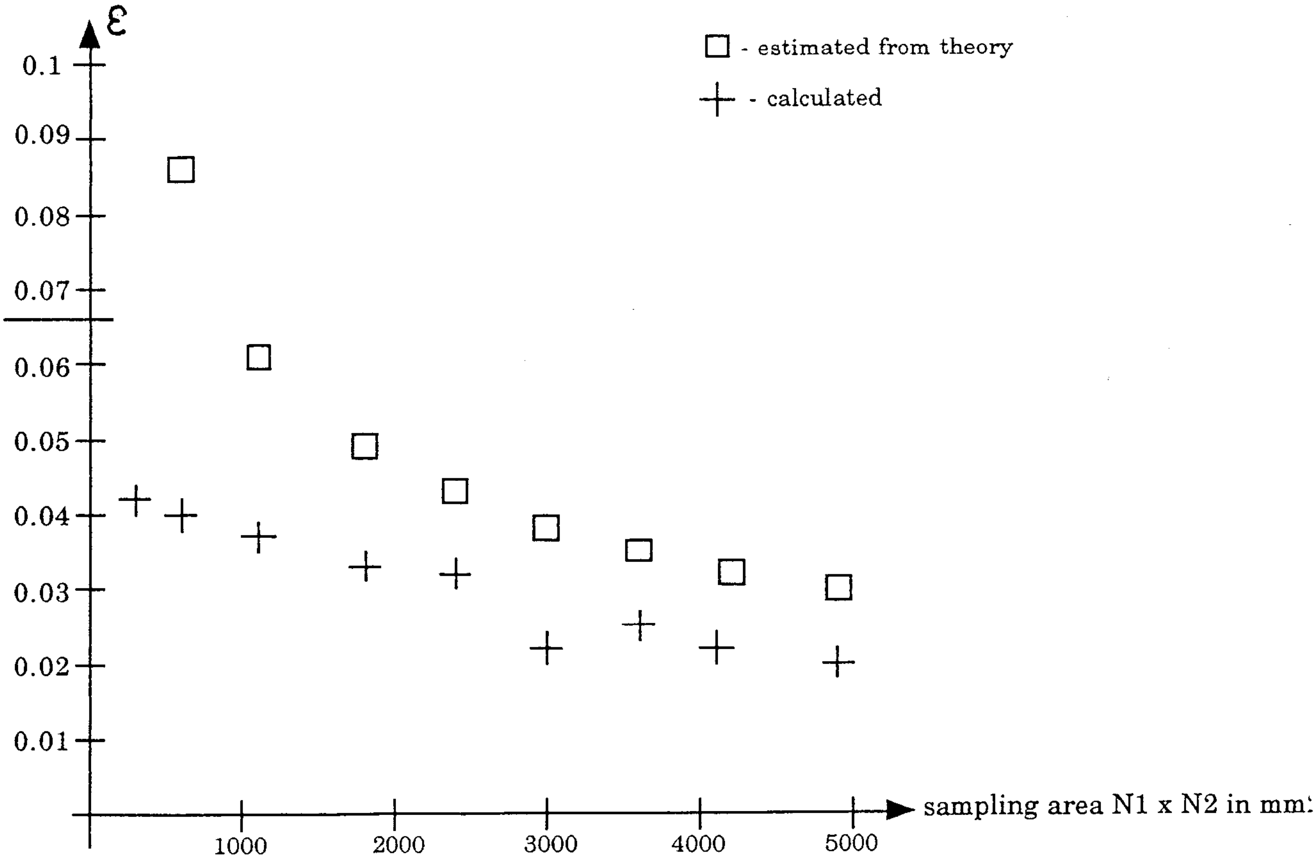

Figure 6.14: Mean value estimates for grid turbulence in air.

Here we find very good agreement between the estimated and calculated values for ϵ, especially for larger sampling areas, which is hardly surprising as this is where the simplified results are valid. The reason for the large discrepancies for smaller sampling areas is simply that the theoretical predictions are not as valid for this range.
The values of ϵ estimated from theory are larger than those actually found for this particular flow. Since the theoretical results are heavily dependent on the choice of integral lengthscale L, it would appear, at the moment, that our initial choice of $L = 2 \times M$ is slightly too large.

Note that, according to theory, if we want to estimate the mean value for this flow, with a normalized standard error of less than 5%, we will be required to sample over an area greater than 2000 mm^2 (1 frame = 2400 mm^2).

Table 6.2 and Figure 6.15 display the normalized standard error ϵ for mean square value estimates over the area $N_1 \times N_2$, for homogeneous near-isotropic grid turbulence in air with a two-dimensional integral lengthscale of $L_2 = 256mm^2$.

Table 6.2 Mean square value estimates for grid turbulence in air.

Sampling area $N_1 \times N_2$ (mm^2)	ϵ estimated from theory	ϵ calculated from PIV results
300	0.230	0.087
600	0.162	0.081
1200	0.1115	0.075
1800	0.094	0.068
2400	0.081	0.063
3000	0.073	0.056
3600	0.066	0.055
4200	0.061	0.045
4800	0.057	0.040
Small sampling areas $\epsilon = 0.1315$		

Again we find reasonable accordance between the theoretical predictions and the results calculated from PIV measurements. Similarly it appears as if we could well have chosen a slightly smaller value for the integral length scale.
As a final example, we note that for this type of flow, we would have to sample over more than 3600 mm^2 (1 frame = 2400 mm^2) in order to achieve a normalized standard error in the estimate of the mean square value of less than 5%.

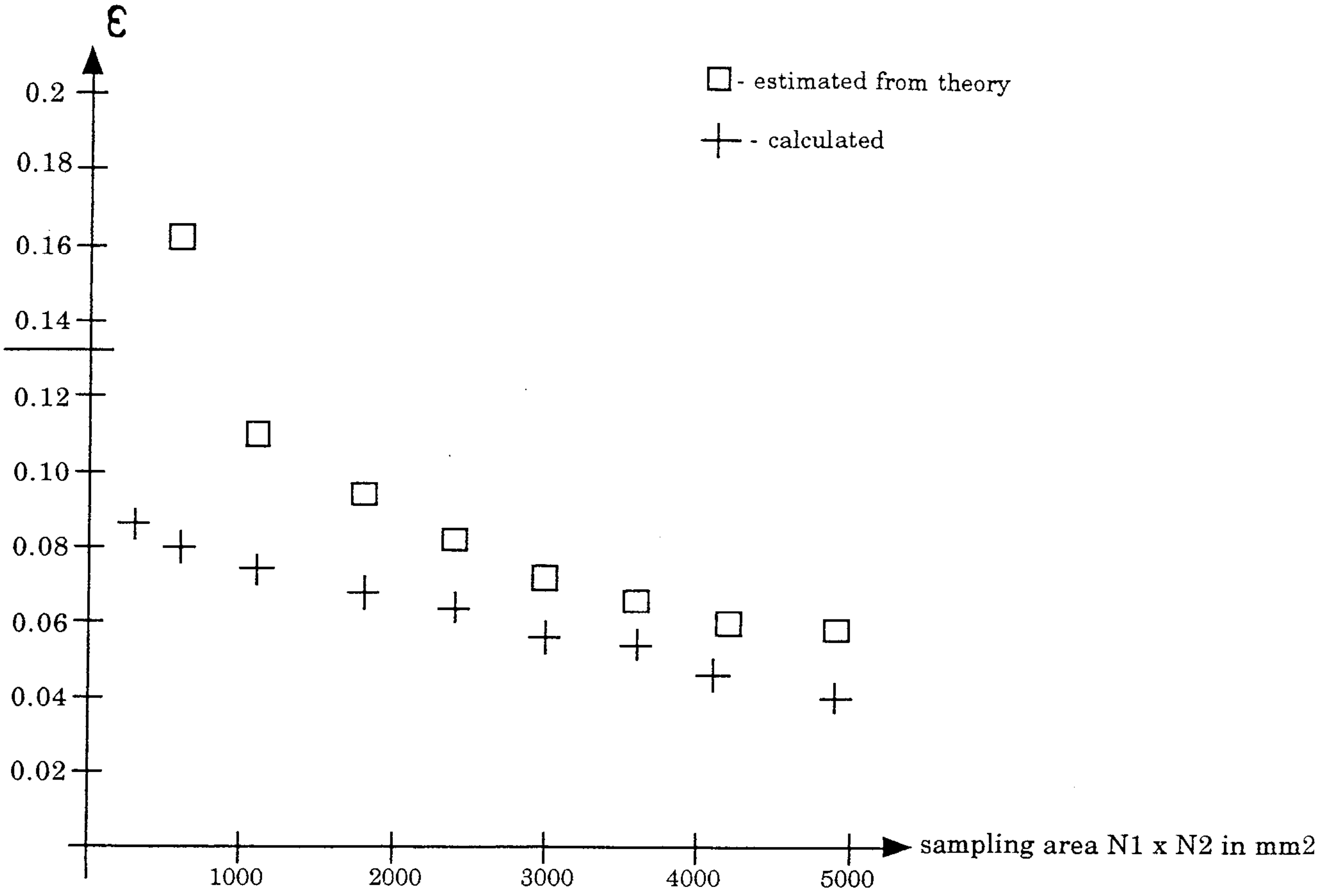

Figure 6.15: Mean square value estimates for grid turbulence in air.

Conclusions.

PIV was succesfully applied to homogeneous isotropic grid turbulence in air with a mean flow of 1 and 2 m/s. The results reveal a multitude of details about the flowstructure, resolving individual structures down to a size comperable with Taylors lengthscale for the flow; even eddies down to a size of 3mm in diameter were clearly identified.
In addition to being an outstanding flow visualization tool, PIV has also been shown to produce accurate quantitative results. Furthermore, theoretical predictions regarding the error introduced when sampling over a finite area of the PIV results were verified using results from these measurements. It was, however, evident that great care has to be taken when determining a value for the integral lenght scale for the given flow. This will be discussed in more detail in the general conclusion for this chapter.

6.2 PIV applied to grid turbulence in water.

This set of experiments with measurements on grid-generated turbulence in water were conducted using one of the wave flumes at The University of Edinburgh.

The measurements were performed as a time-series, allowing us to study both the spatial and the temporal development of the flow.

6.2.1 Experimental set-up.

The flow was generated in a wave flume, the tank having dimensions; $6m \times 1.1m \times 0.4m$. As in the previous set of measurements, we are concerned with homogeneous, isotropic turbulence. The wave tank has a steady flow facility, although in this case we do not have the contraction and smoothing screens available in the windtunnel experimental set-up.
The turbulence generating grid has a square mesh with round rods, with grid diameter $d = 6.25mm$, and grid spacing $M = 18.75mm$ resulting in a solidity of:

$$\sigma = d/M(2 - d/M) = 0.556$$

The grid was found to produce an rms tubulence level of $\overline{u}/\overline{U} = 0.062 \approx 6\%$. Again the flow was expected to be fully developed at a distance of 20 mesh diameters from the grid.

For this flow regime we have no direct comparison with LDA measurements. The wave flume have been used for seveal different types of experiments [68, 72] and good agreement have been found between LDA and PIV experiments for these. Furthermore, as was stated earlier, there is no reason to expect the PIV measurements to be less accurate than LDA measurements for this type of experiment.

One of the possible problems is to find suitable scattering particles; ones which follow the flow, scatter light well and are spherical.
For experiments in water, several types of scatterers have been tried over time. We used connifer pollen. This is almost neutrally bouyant [68] and scatters light well. Conifer pollen particles, however, are not quite spherical, more of an oblong shape, which will cause them to rotate in the flow, but they are still considered the best choice. The pollen particles have a diameter of about 70μ, and are thus small enough to follow the flow accurately.

Measurements were performed for a flow speed of $0.07m/s = 7cm/s$, resulting in a Reynolds number of:

$$R = 1307$$

The camera used was a Nikon F801 with an AF Micro-Nikkor 60mm lens. This was equipped with a boosterpack to increase the possible number of frames per second. Film used was Kodak Tmax 400, with a resolution of 100lines/mm. The camera was mounted vertically at a distance from the investigated flow plane corresponding to a magnification of 0.13.
According to the formula:

$$d_i = \left(M^2 d_p^2 + d_{spot}^2 + d_r^2\right)^{1/2}$$

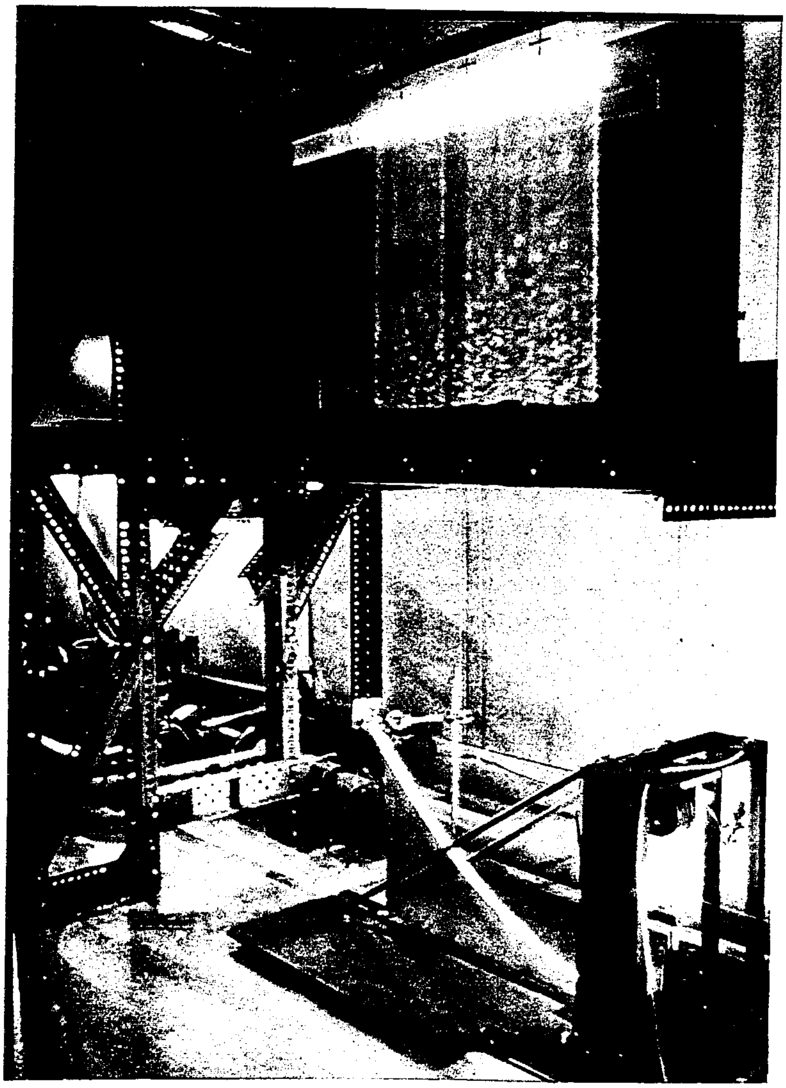

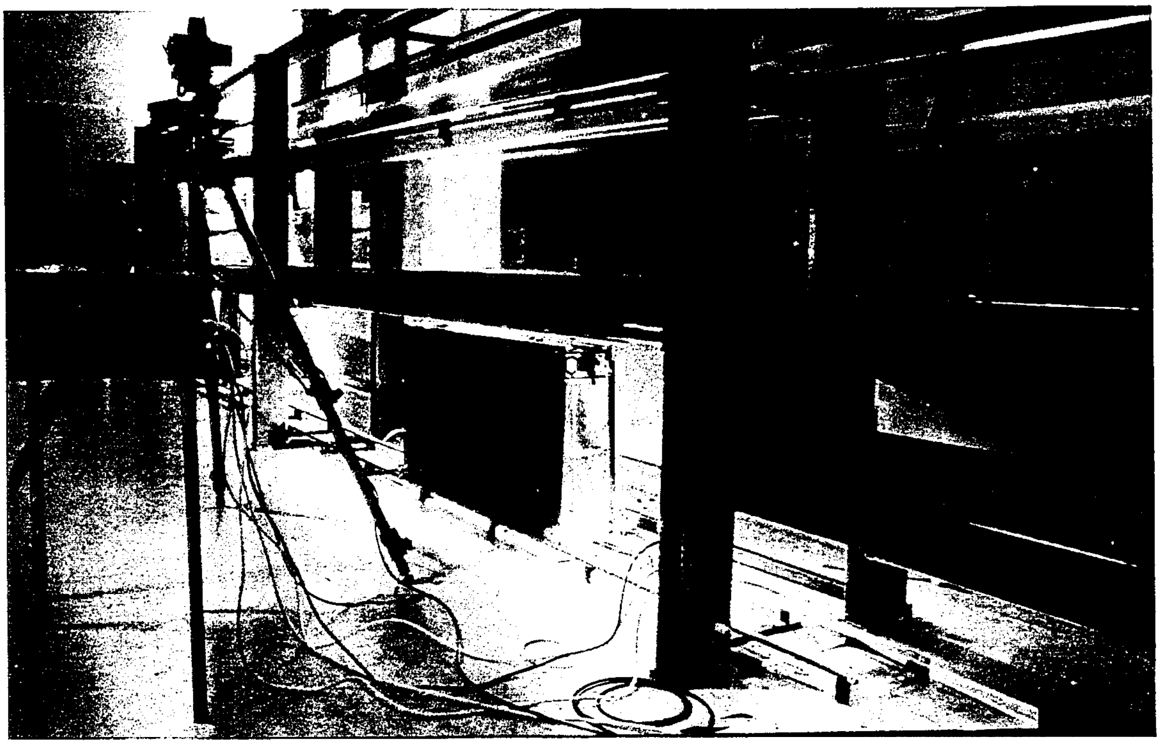

Figure 6.16: The wavetank and the illuminating scanning beam arrangement.

$d_i = 15\mu$ and is completely resolved by the film.

A scanning beam illumination system was employed, using an 8-sided mirror and a 15 Watt argon-ion laser. A scanning speed of $8.1m/s$ and a shutter speed of 1/30 was chosen.

Figure 6.16 shows the illuminating system and the resulting laser ligth sheet. For all measurements the laser output was between 8-10 Watt.

Several measurements were performed. In the ones selected and presented here, the area covered extends from immediately behind the turbulence generating grid, to 15 mesh diameters downstream. We should thus expect to see a developing, and to a certain extend also decaying, flow on the resulting vector velocity and vorticity plots.

This series of experiments were performed as a time-series, that is the camera was set to take a continous set of PIV-pictures with a known time separation of 230ms equal to 4.35 frames per second. This was done to make it possible to study, not only the spatial but also the temporal development of the flow.

First the mean flow, magnification and photographic parameters were determined by taking a trial film without the grid in place, but both with and without the steady flow. After these parameters were properly established, the grid was put in place and the measurements described above performed.

The fully automated Youngs fringes analysis system described in Chapter 4 was employed for analysis of the PIV negatives. The analysis beam has a circular diameter of 1mm and a Gaussian profile. Similarly to the preceeding experiments, an area of $20mm \times 30mm$ was analysed in 0.5mm steps, again with suitable filtering.

6.2.2 Results.

A typical example of an enlargement of a PIV negative from this experiment is found in Figure 6.17.

The small crosses were marks on the tank side used for alignment of the camera. Small abberations in the light sheet are also visible, showing up as stripes. These effects are generally caused by slight uneveness in the surface of the parabolic mirror.

Figure 6.18 - 6.21 shows the analysis of one negative starting with the flow as it looks in Figure 6.18. In Figure 6.19, the mean flow is subtracted revealing the underlying structure of the flow and Figure 6.20 and 6.21 are different types of vorticity plots for the same negative.

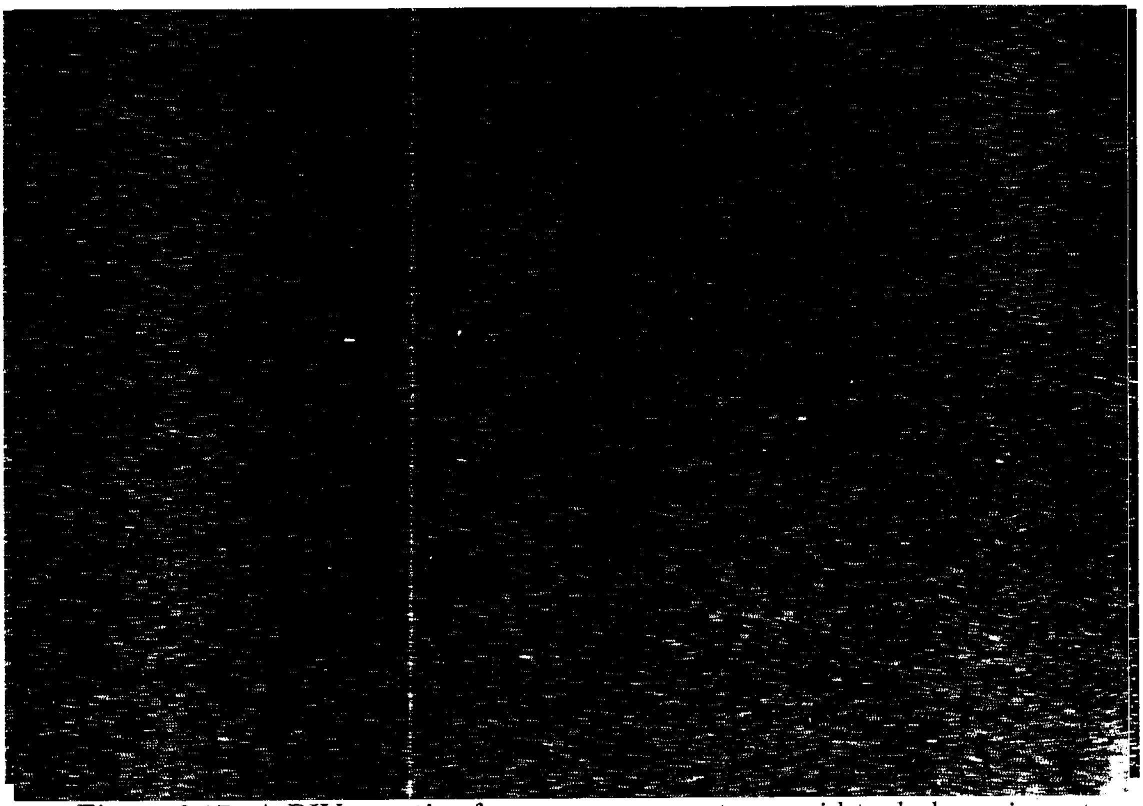

Figure 6.17: A PIV negative from measurements on grid turbulence in water.

In Figure 6.19 we have framed certain structures such as eddies. Since the negative was analysed on a 0.5mm grid, the separation between the vectors in the plot corresponds to 3.85mm in the flow plane. As in the previous experiments, we find that the resolution is indeed very good. Structures down to a size of 10mm are clearly resolved and even smaller structures can be discerned.

As mentioned above, we performed these measurements as a time-series and Figures 6.22 to 6.35 show a consecutive series of the vectorplots, with the mean velocity subtracted, the time between each plot being 230ms. It can perhaps be difficult to follow the development of the flow on the vector plots, but on the corresponding vorticity plots Figure 6.29 to 6.35, the flow situation is much clearer. Bearing in mind that the turbulence generating grid is immediately to the left of the picture, we can actually follow the generation and development of the vortices. As an example: On the first picture a row of vortices, all rotating the same way, have just been generated. The whole structure is about 6mm long and the individual eddies 2-3mm in diameter. It is now possible to follow this structure in time and space. As it moves downstream, the structure splits up into independent vortices that slowly decay as the flow develops, in accordance with the flow becoming more and more homogeneous and isotropic further downstream from the grid. Note that the seven frames shown here extend over a time period of less than 1.5 seconds.

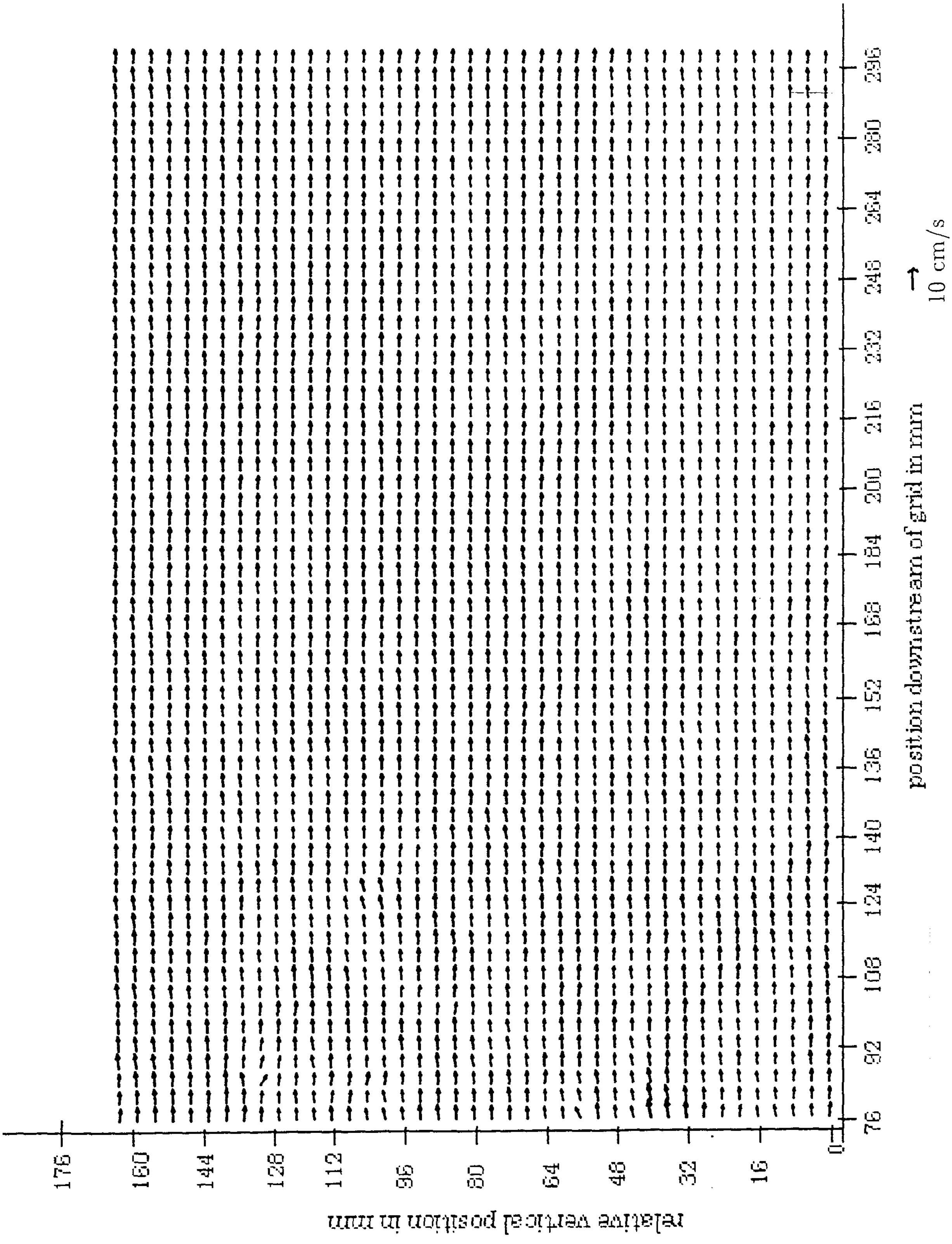

Figure 6.18: PIV measurement of grid-generated turbulence in water, mean flow 0.07m/s.

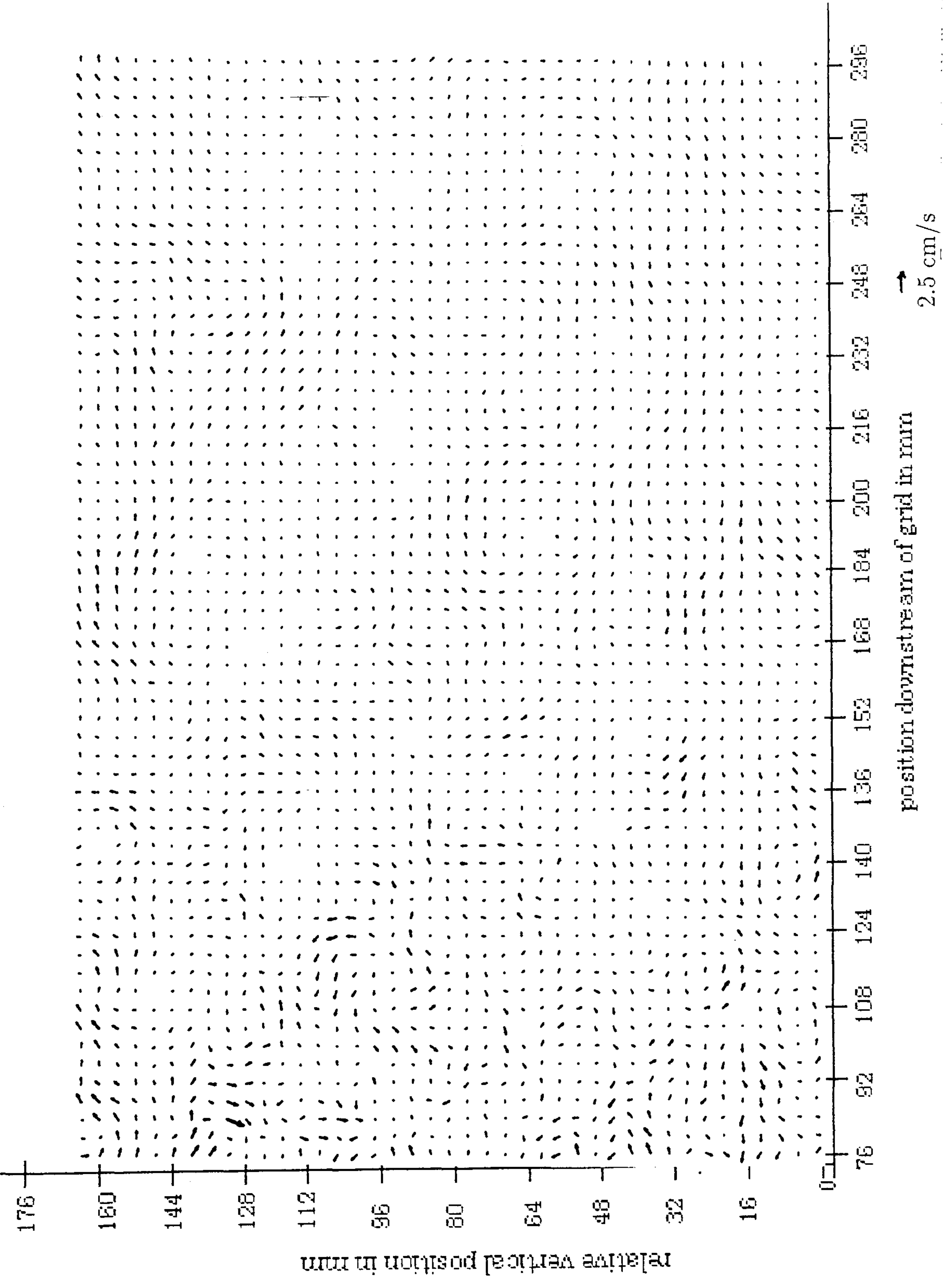

Figure 6.19: PIV measurement of grid-generated turbulence in water, mean flow 0.07m/s subtracted.

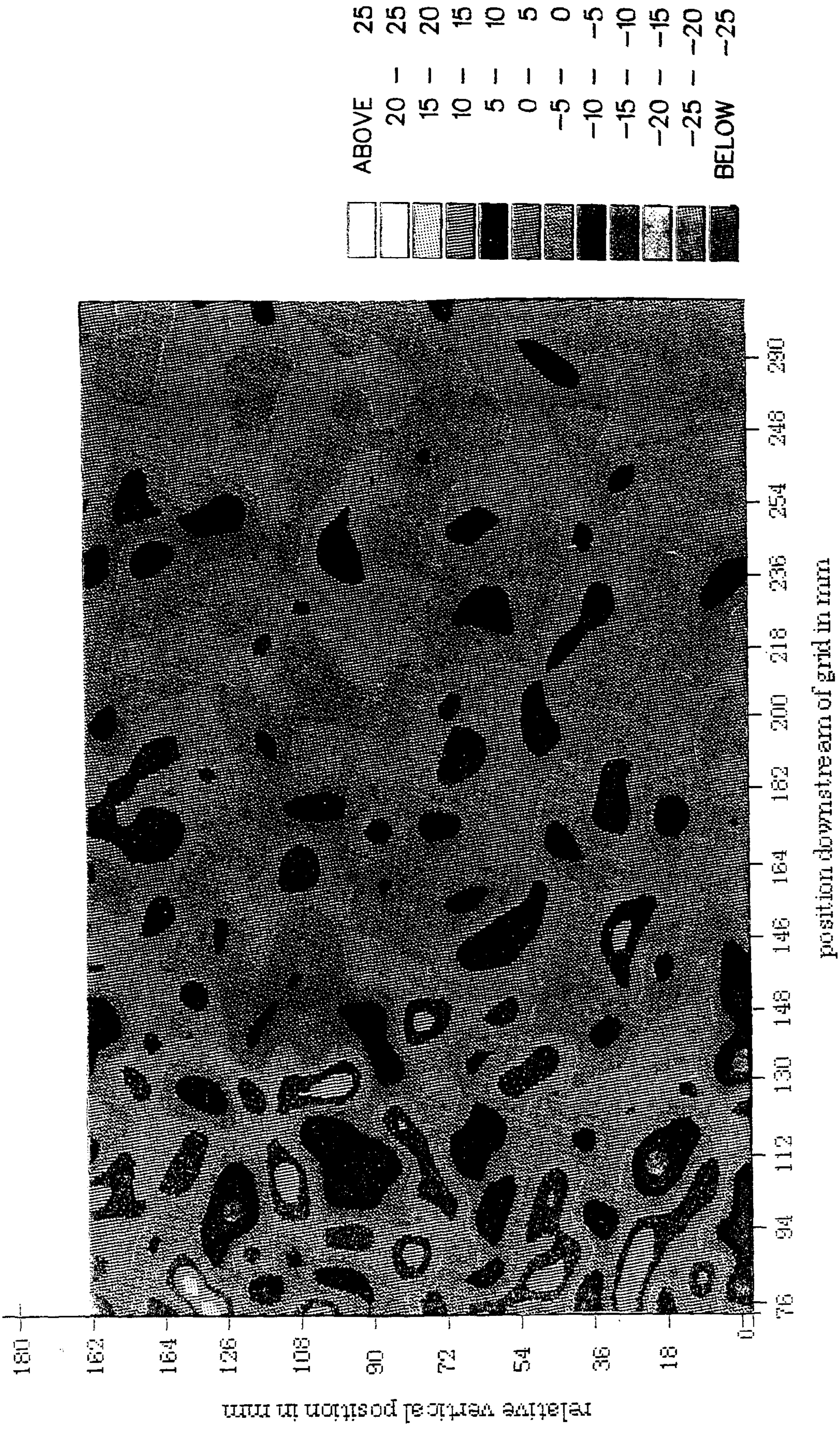

Figure 6.20: Vorticityplot of the flow pictured in Figure 6.19.

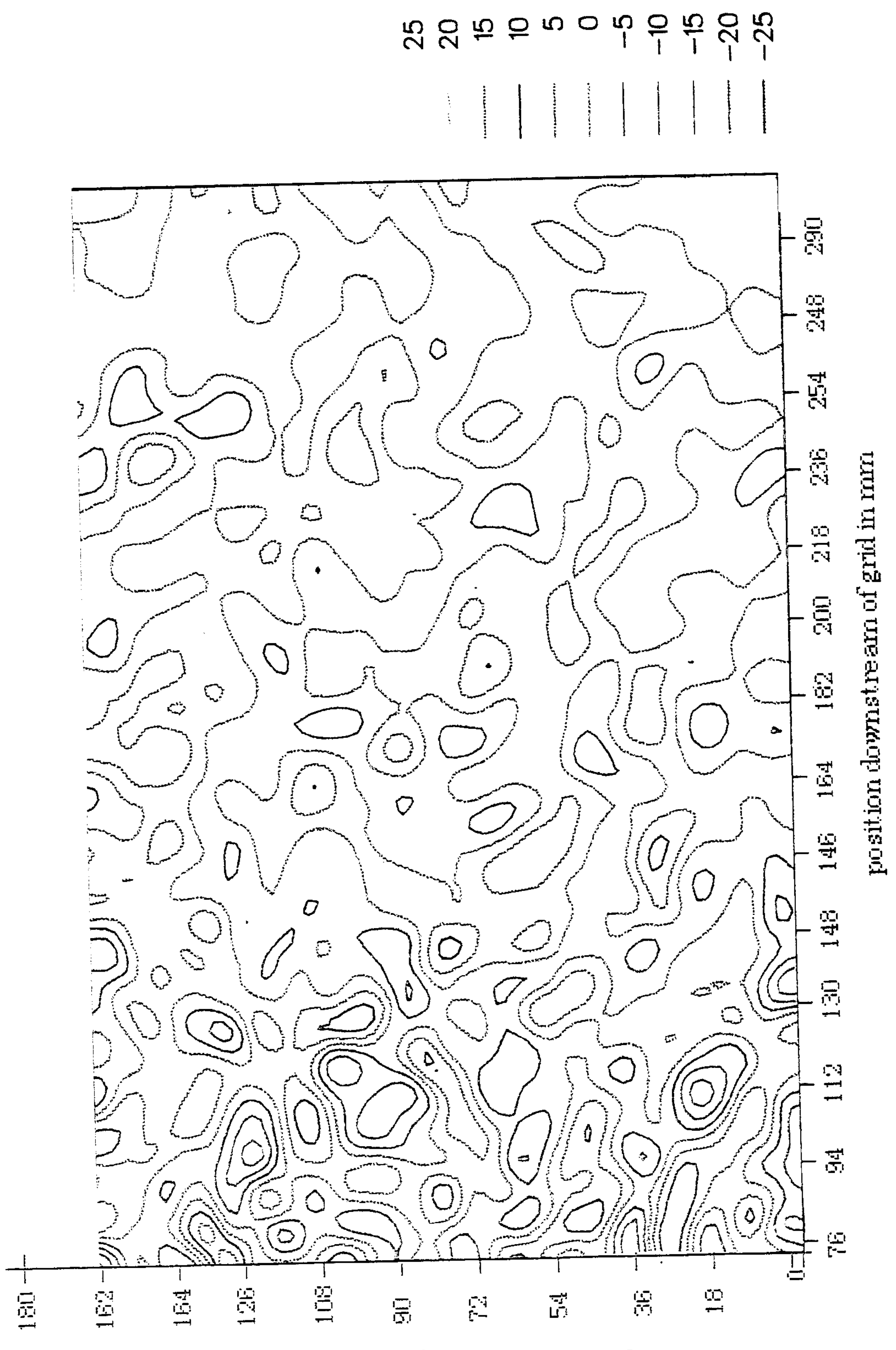

Figure 6.21: Vorticityplot of the flow pictured in Figure 6.19.

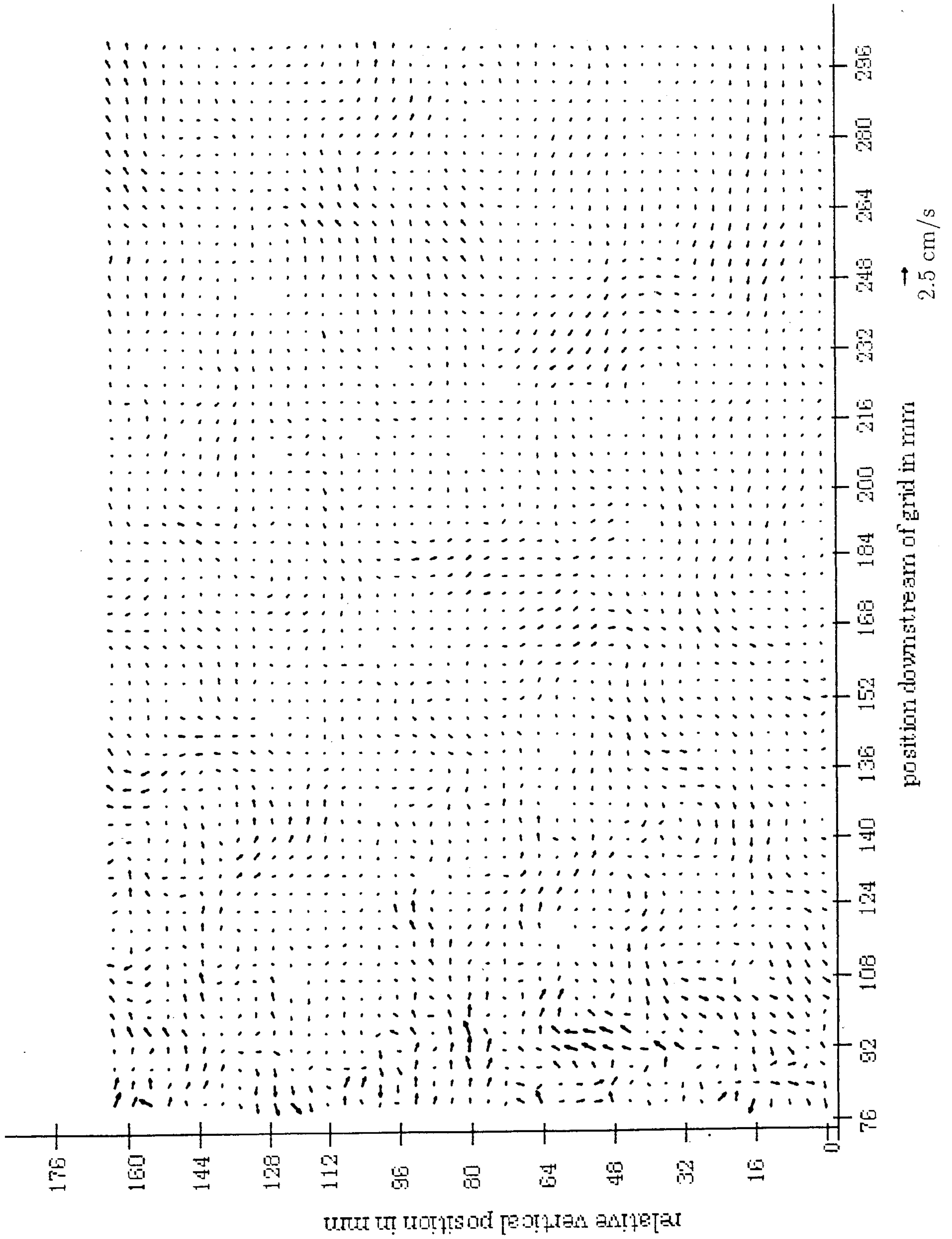

Figure 6.22: PIV measurement of grid turbulence in water, mean velocity of 0.07m/s subtracted. Frame 1, T=0.

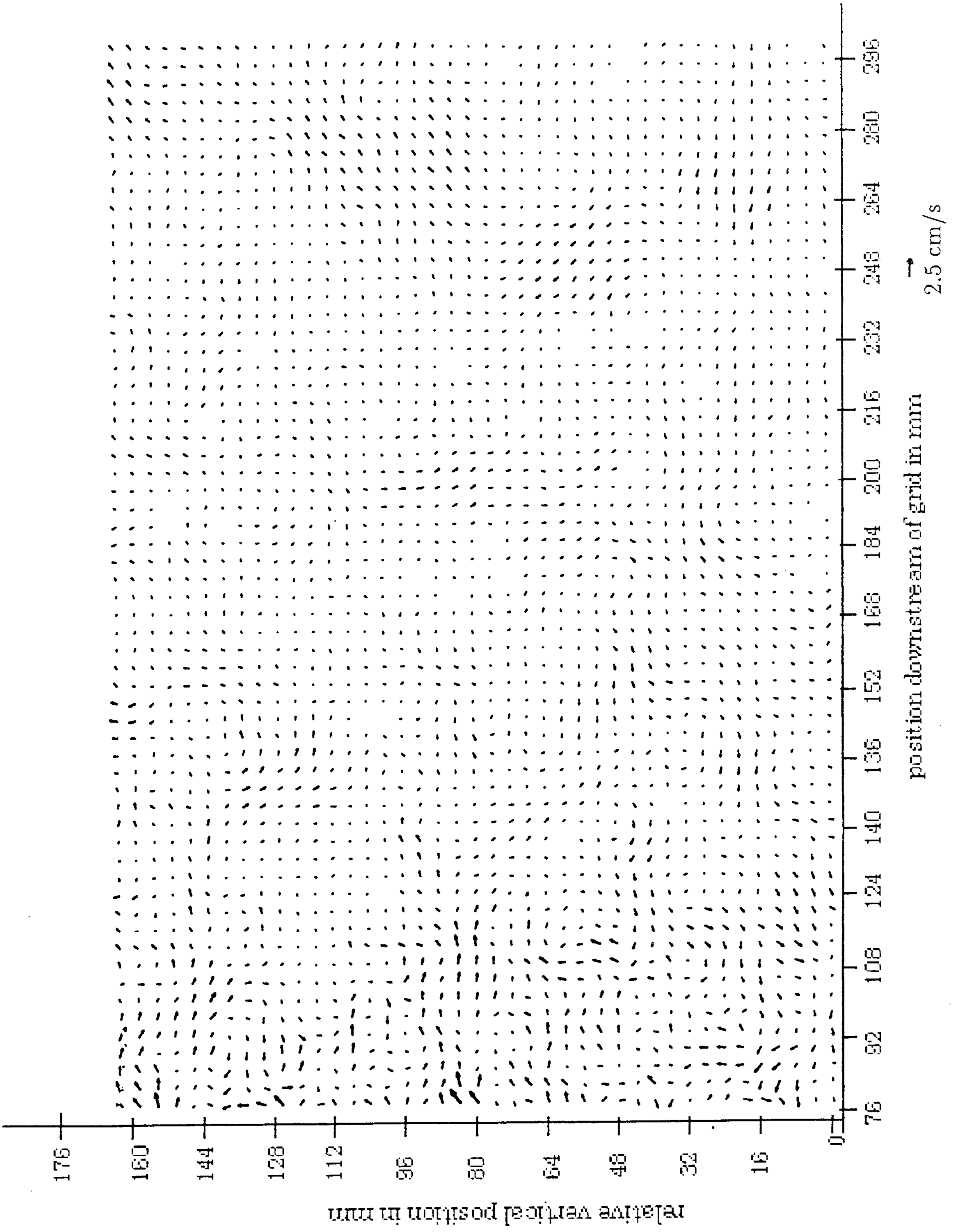

Figure 6.23: PIV measurement of grid turbulence in water, mean velocity of 0.07m/s subtracted. Frame 2, T=230ms.

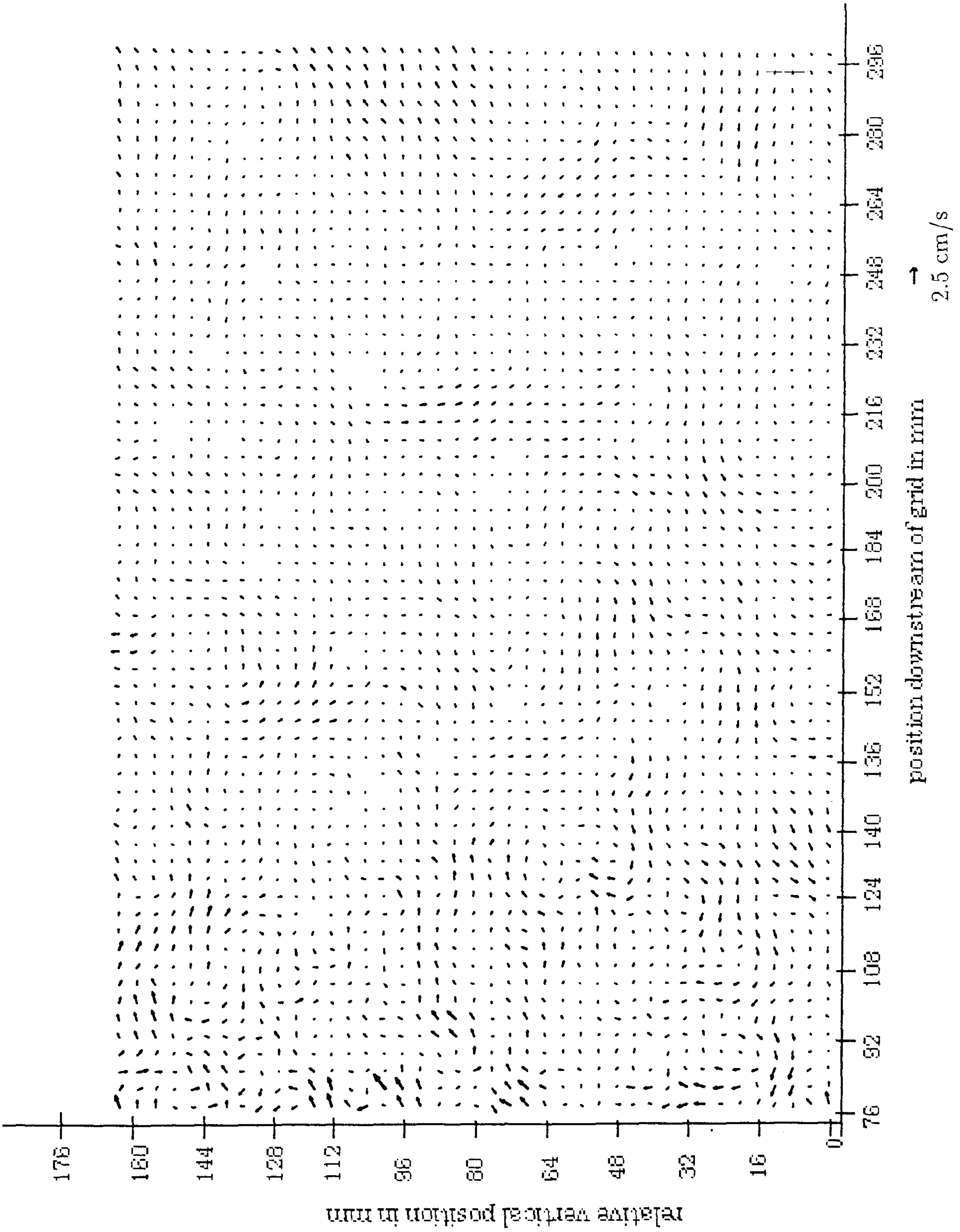

Figure 6.24: PIV measurement of grid turbulence in water, mean velocity of 0.07m/s subtracted. Frame 3, T=460ms.

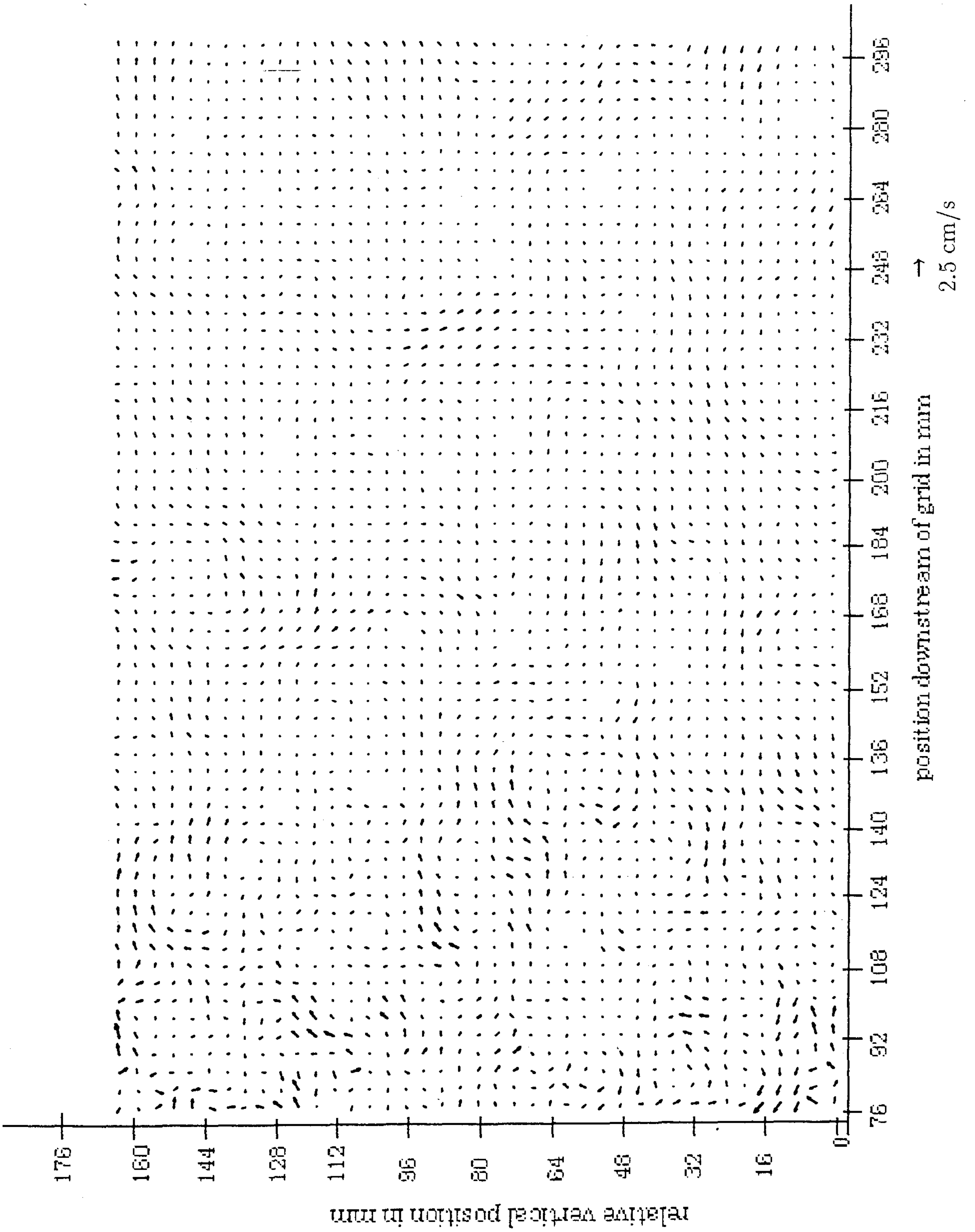

Figure 6.25: PIV measurement of grid turbulence in water, mean velocity of 0.07m/s subtracted. Frame 4, T=690ms.

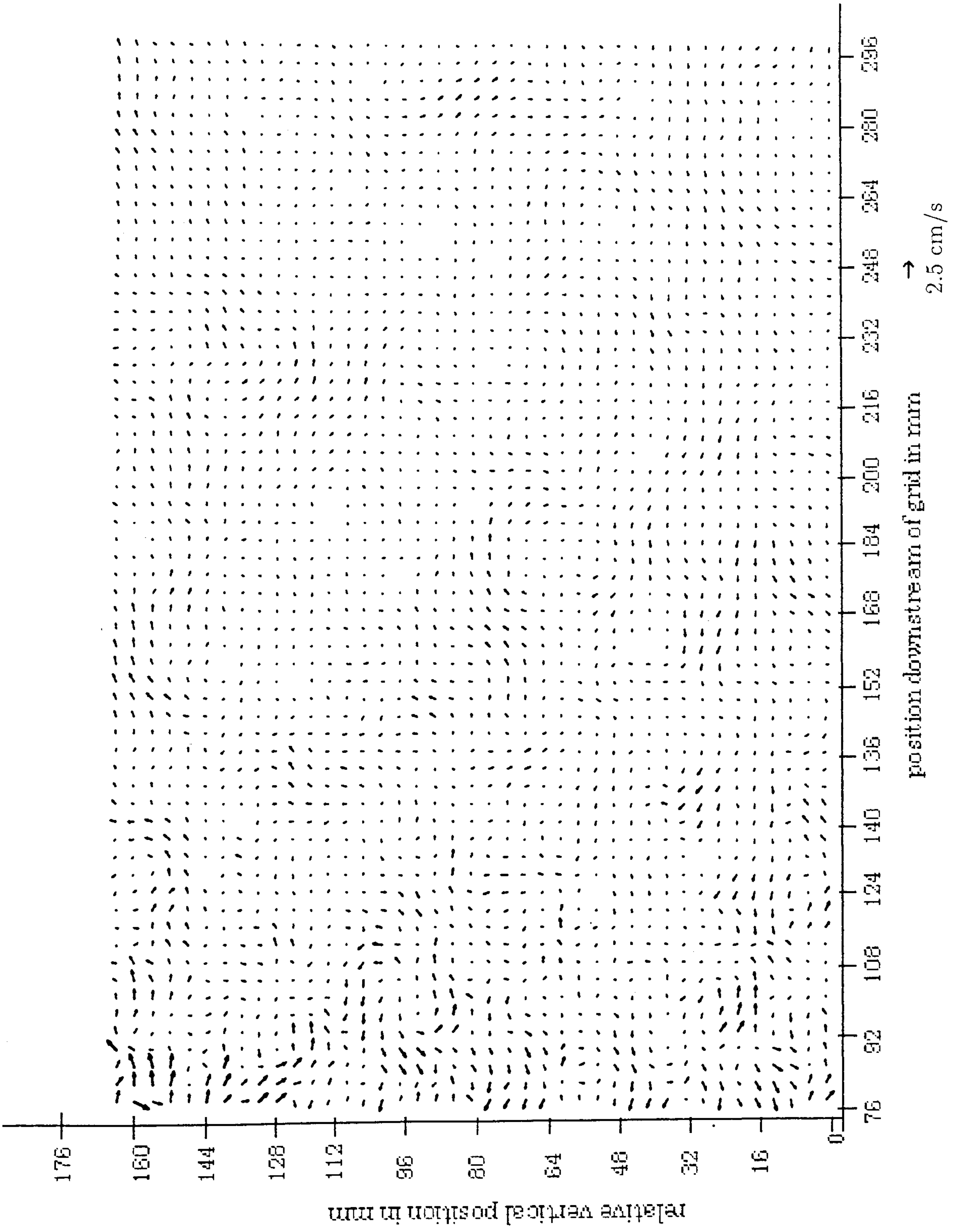

Figure 6.26: PIV measurement of grid turbulence in water, mean velocity of 0.07m/s subtracted. Frame 5, T=920ms.

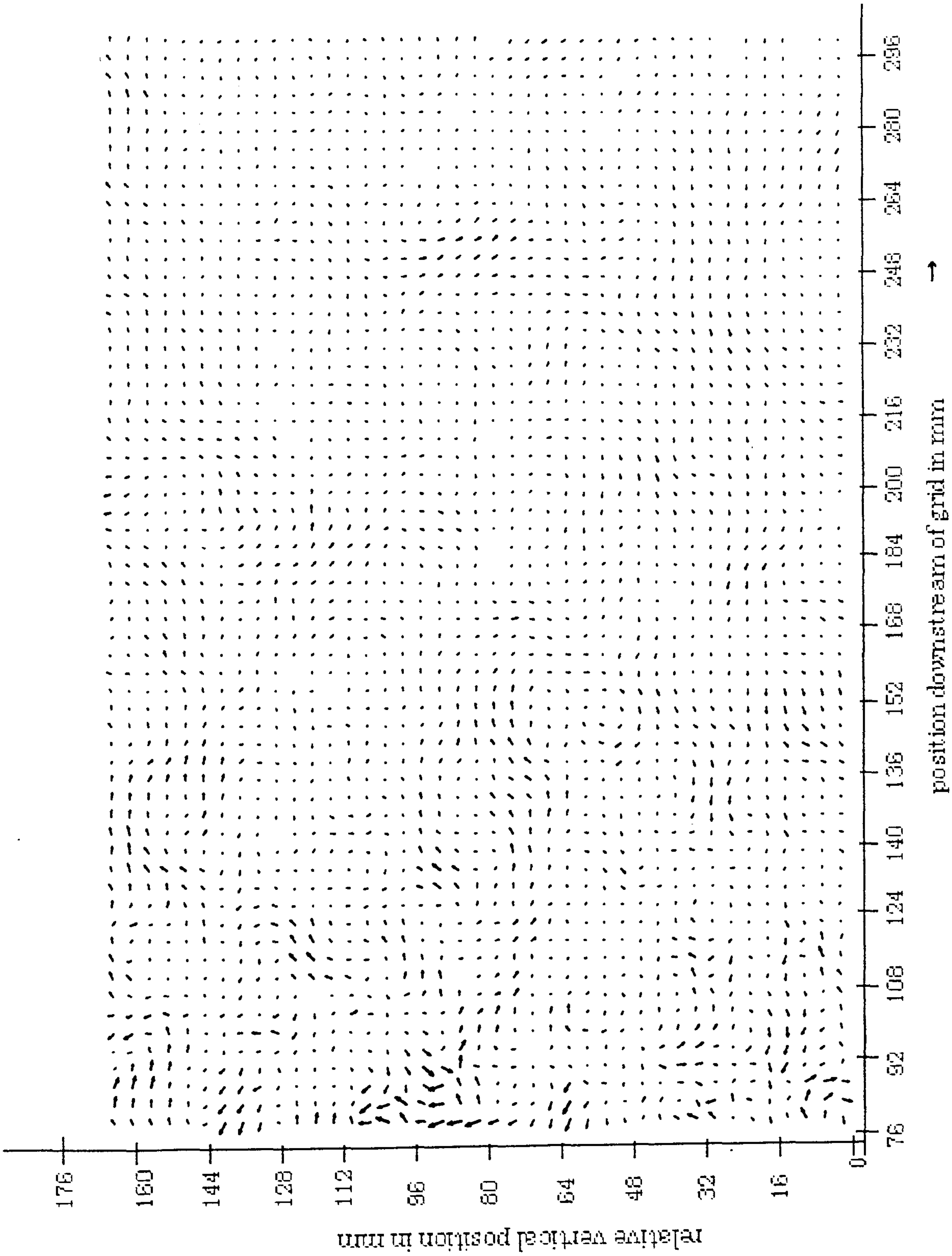

Figure 6.27: PIV measurement of grid turbulence in water, mean velocity of 0.07m/s subtracted. Frame 6, T=1150ms.

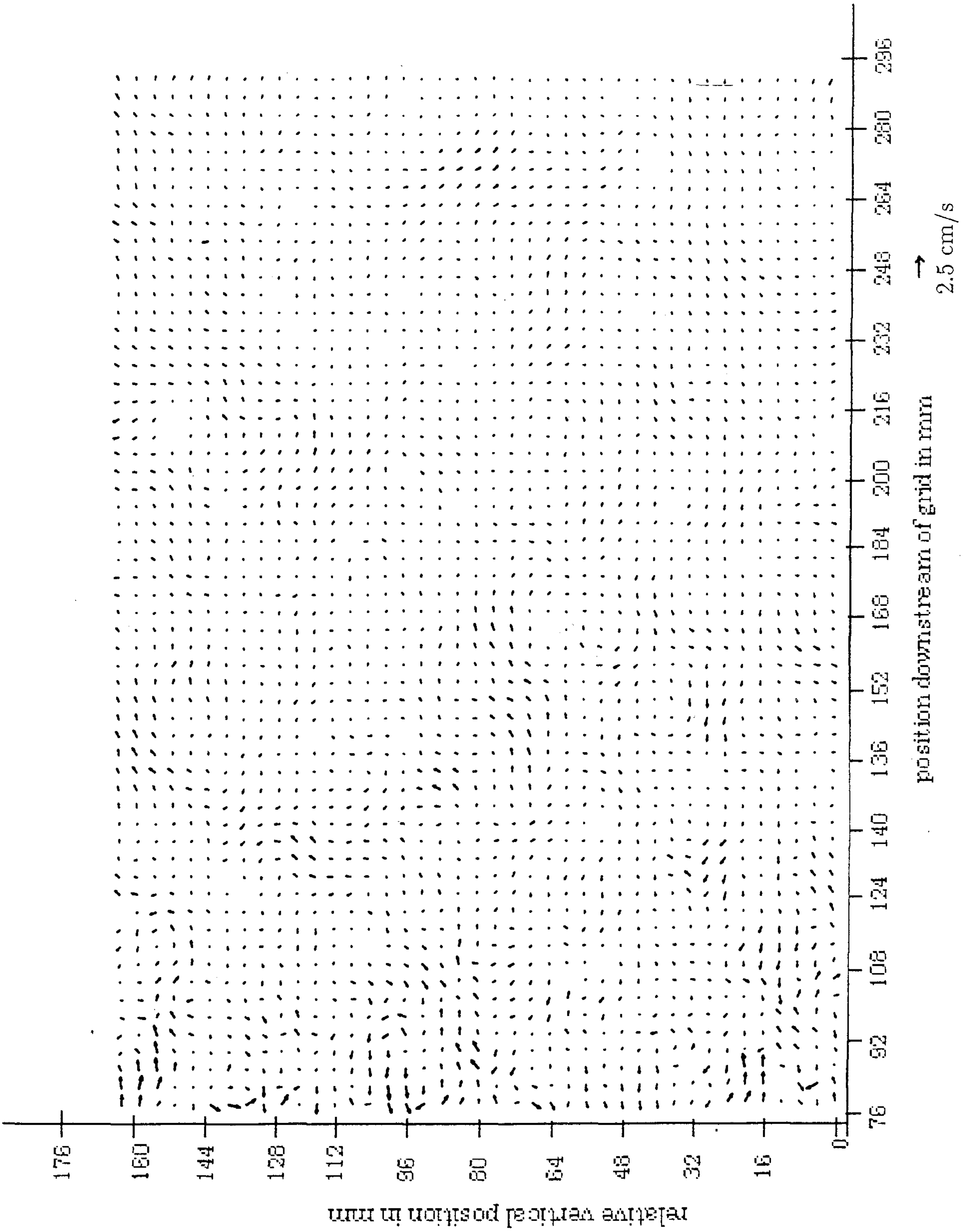

Figure 6.28: PIV measurement of grid turbulence in water, mean velocity of 0.07m/s subtracted. Frame 7, T=1380ms.

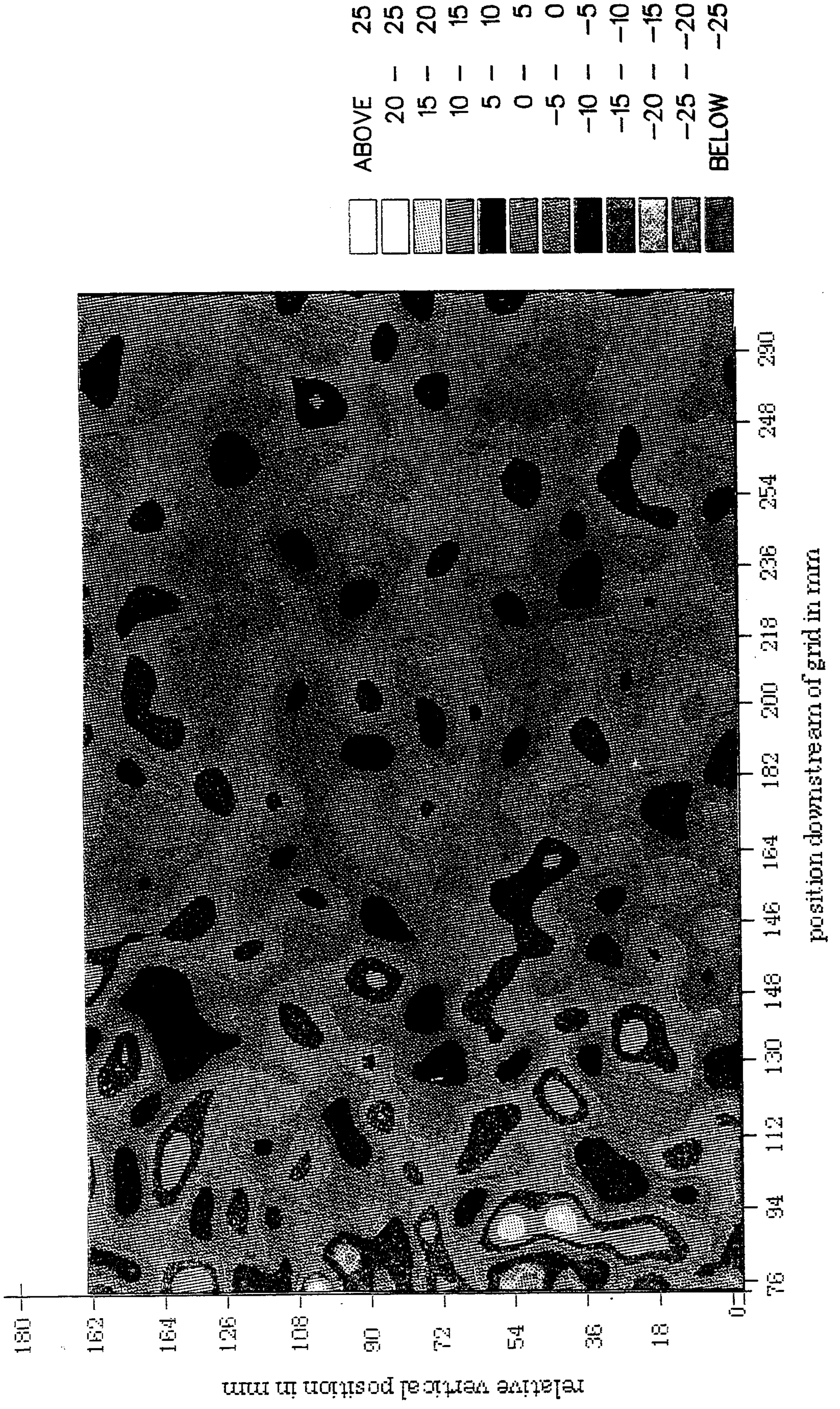

Figure 6.29: Vorticityplot of the flow shown in Figure 6.22. Frame 1, T=0.

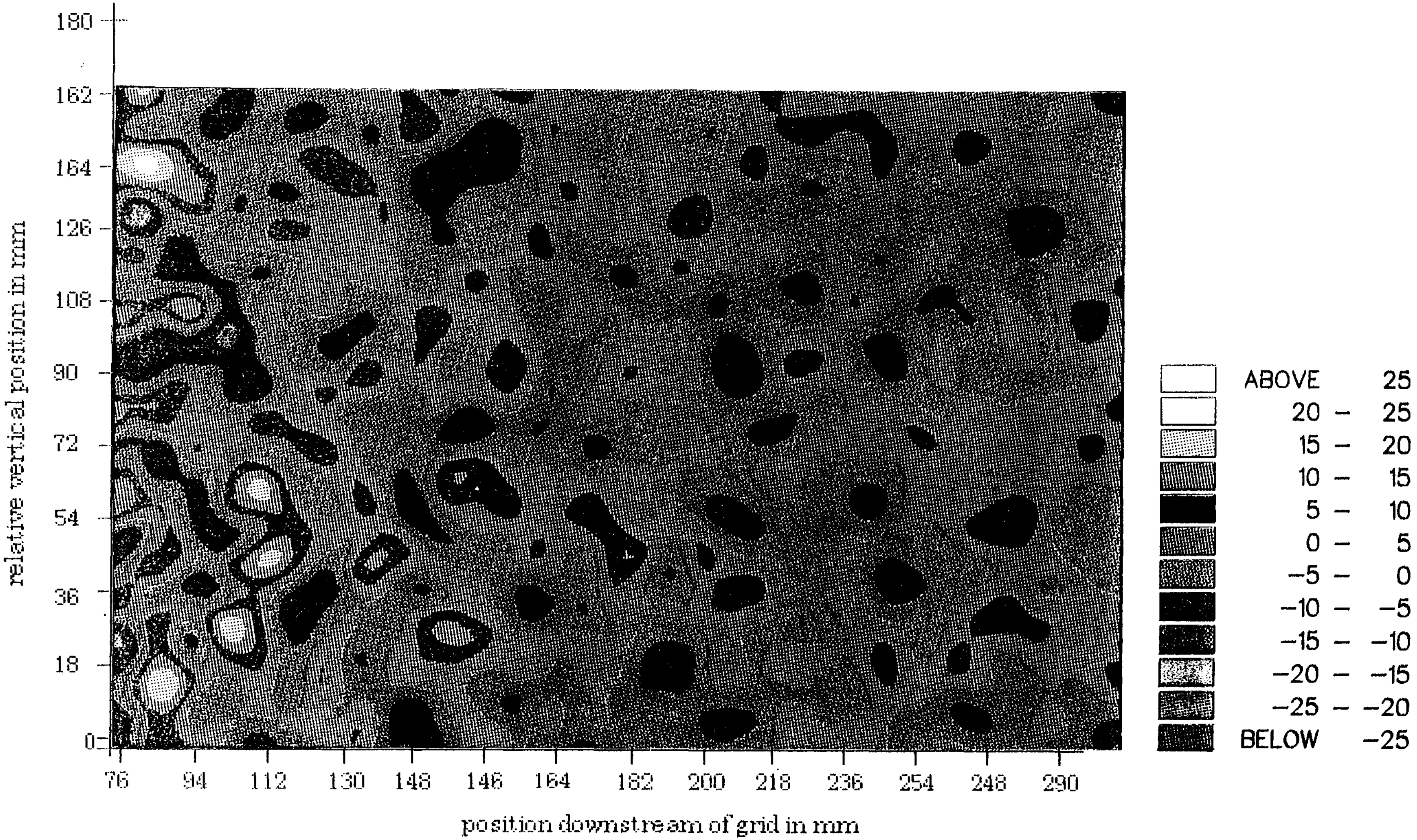

Figure 6.30: Vorticityplot of the flow shown in Figure 6.23. Frame 2, T=230ms.

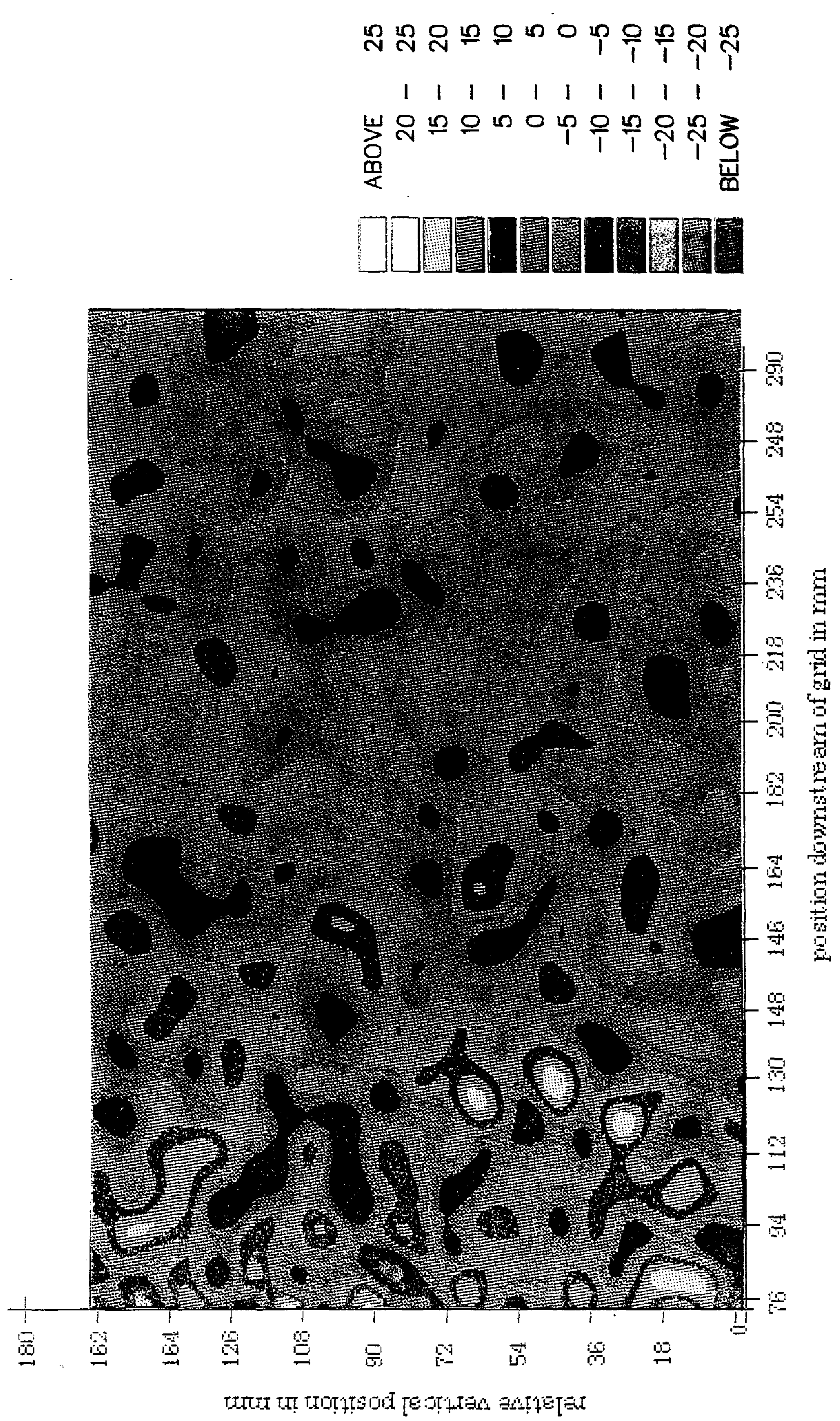

Figure 6.31: Vorticityplot of the flow shown in Figure 6.24. Frame 3, T=460ms.

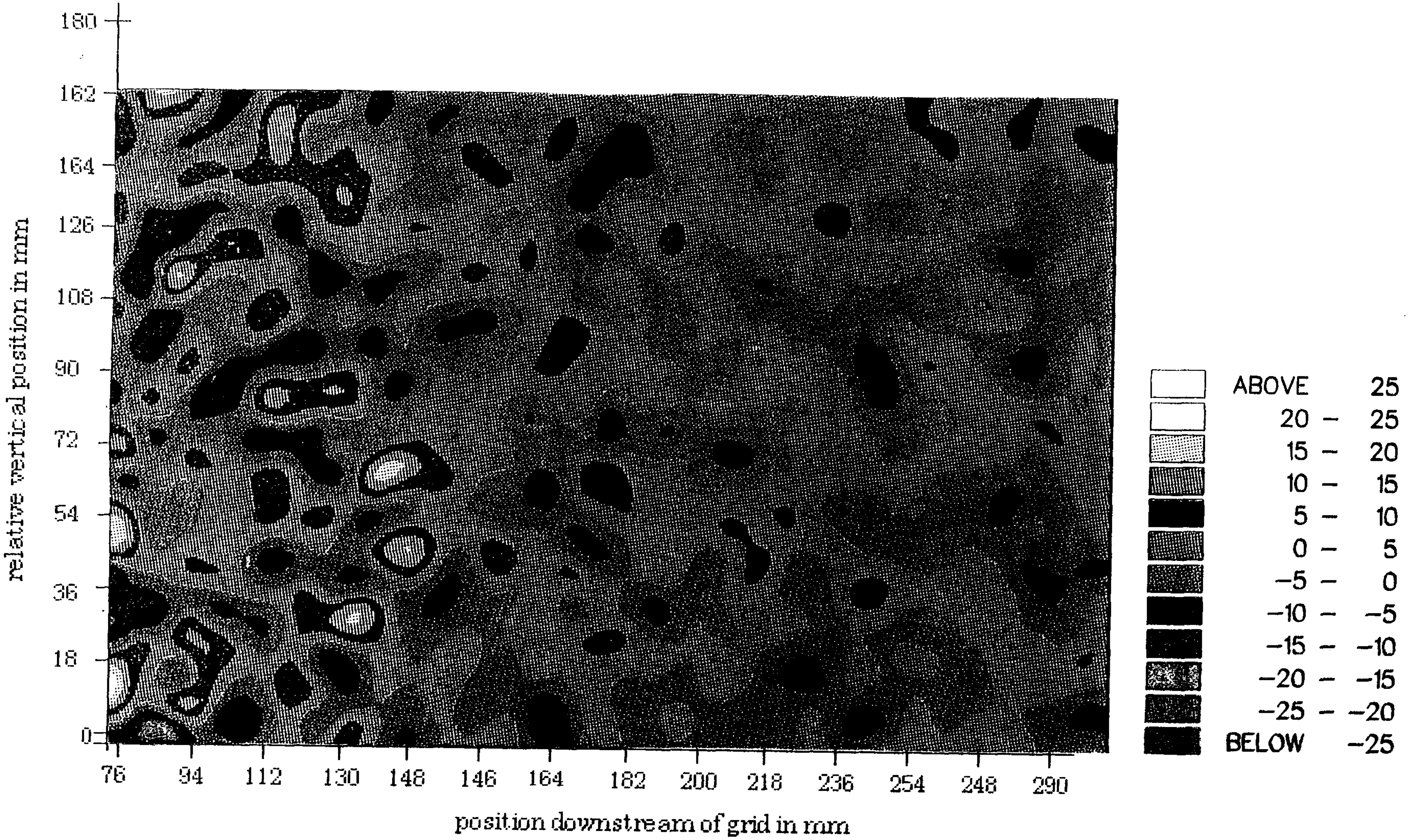

Figure 6.32: Vorticityplot of the flow shown in Figure 6.25. Frame 4, T=690ms.

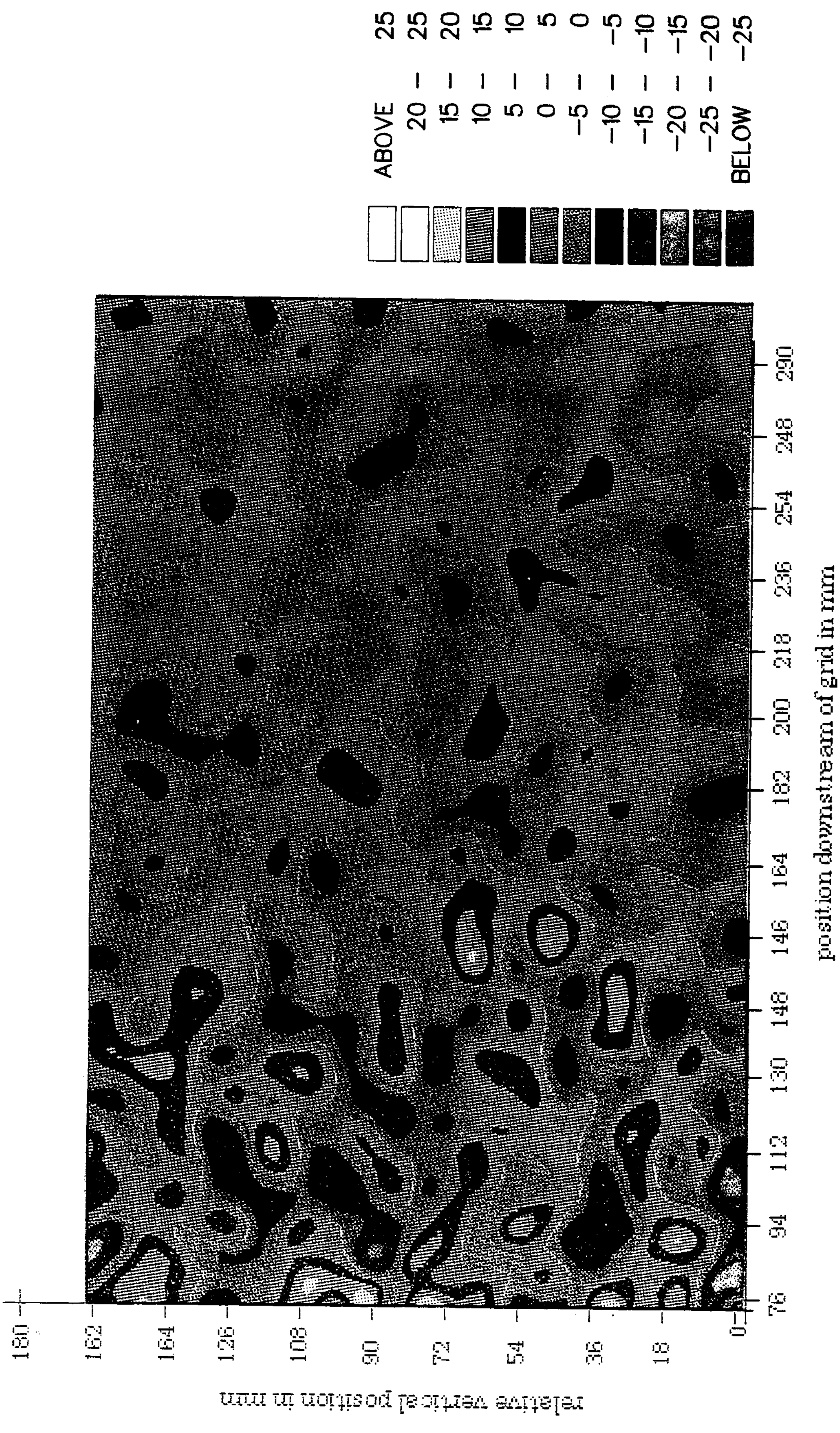

Figure 6.33: Vorticityplot of the flow shown in Figure 6.26. Frame 5, T=920ms.

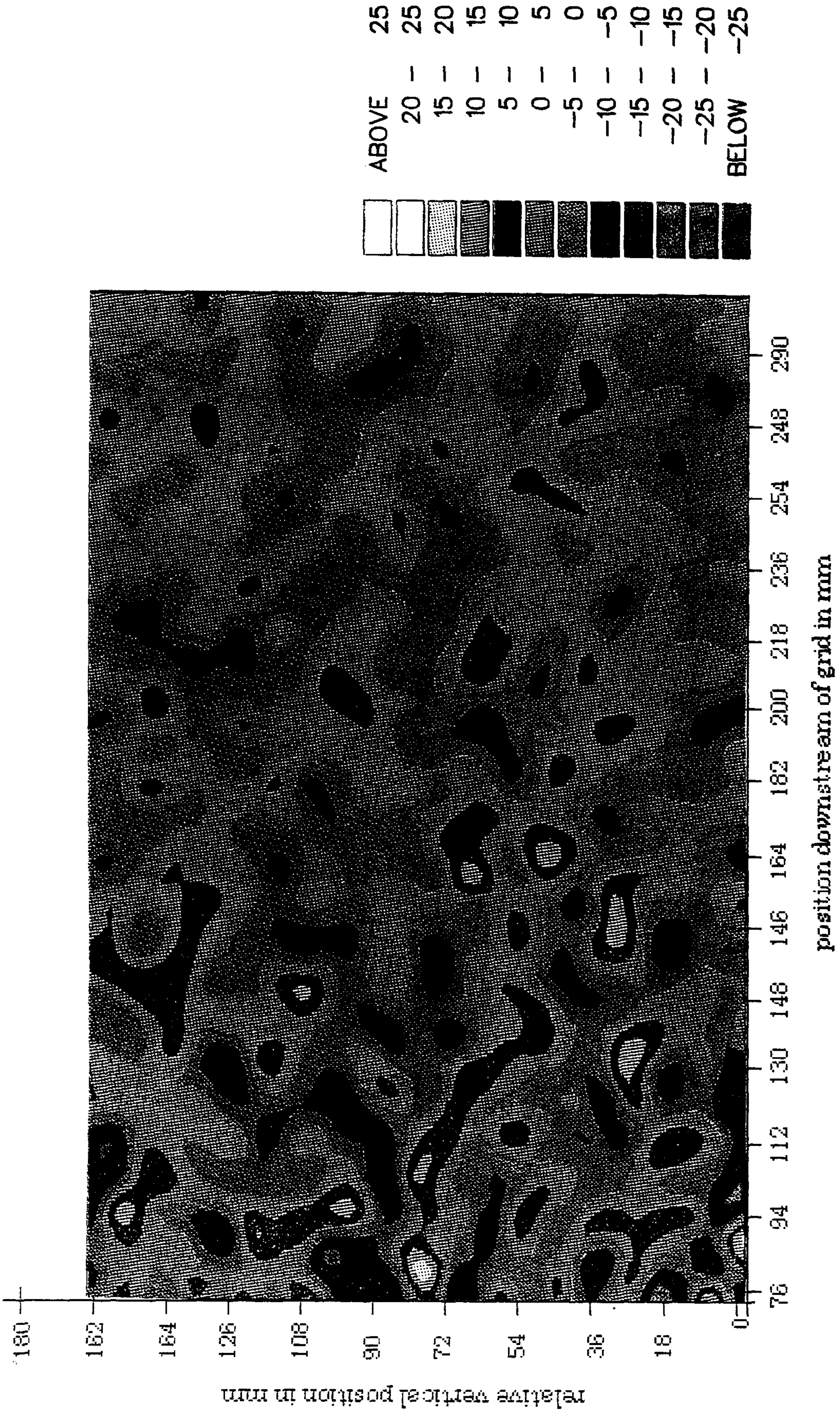

Figure 6.34: Vorticityplot of the flow shown in Figure 6.27. Frame 6, T=1150ms.

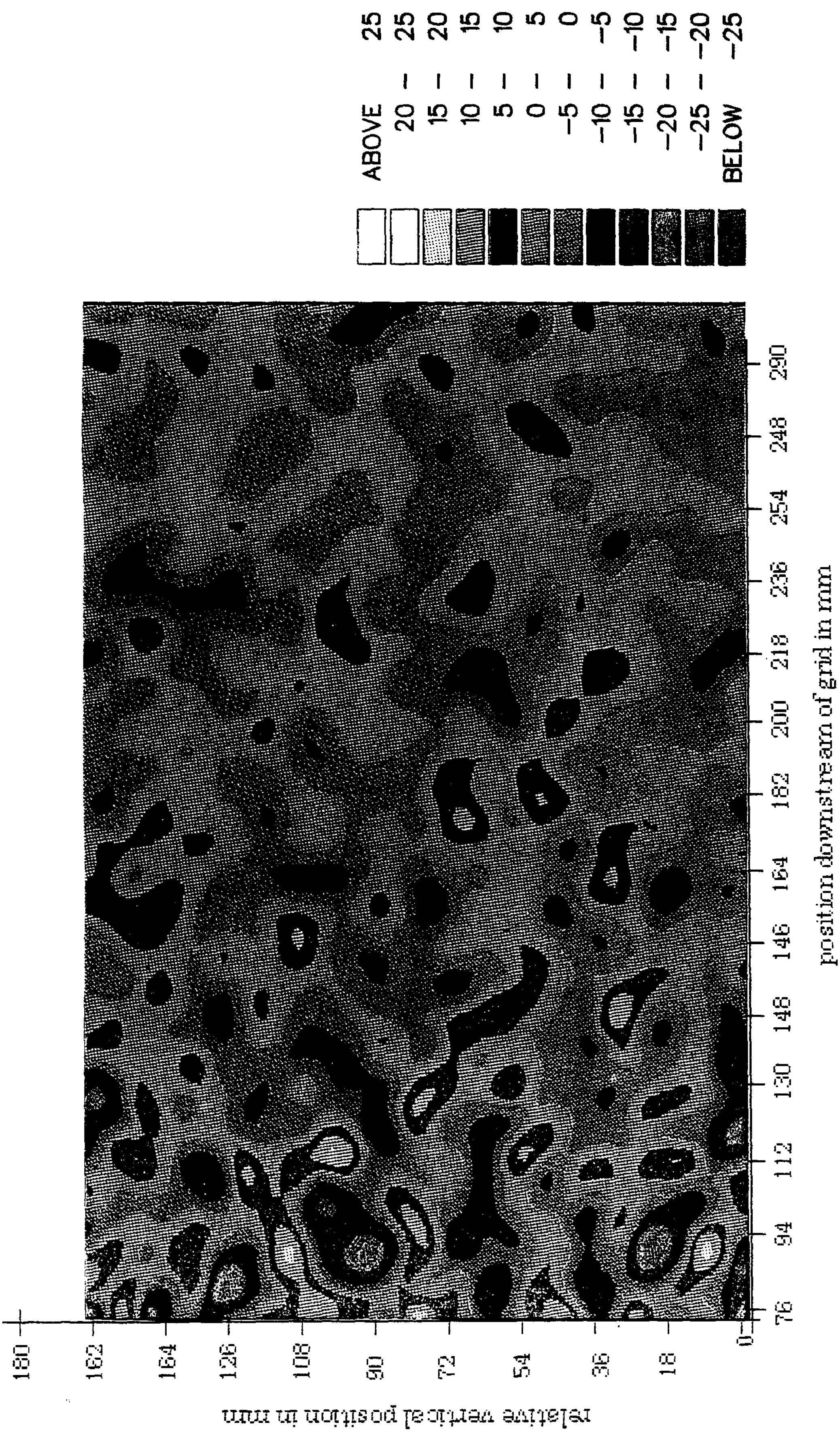

Figure 6.35: Vorticityplot of the flow shown in Figure 6.28. Frame 7, T=1380ms.

Once again it is very clear that PIV is proven to be a very impressive flow vizualisation tool. Furthermore, the vorticety plots from this time-series have been recorded onto videotape, resulting in an animated film of the flow development.

6.2.3 Correlation.

For the calculation of the correlation functions a total number of 10 frames were selected. This provides us with approximately 25100 vector velocity values.
As was mentioned in the preceeding section, it is sufficient to consider the one-dimensional longitudinal and transverse correlation functions $f(r)$ and $g(r)$. These were calculated for each line of the velocity maps, a total of 200 lines, and the general shape of the curve of the functions established.
Figures 6.36 and 6.37 show $f(r)$ and $g(r)$ respectivelyfor grid-generated turbulence, decaying from 6.2%, with a mean velocity of 7cm/s. The curves are in good agreement with what is expected for this type of flow. There is a slight oscillation or periodocity in $g(r)$, which is likely to be caused by the proximity of the turbulence-generating grid. At a distance of $2 \times M$ ($\approx 37mm$) from the grid there is no significant correlation left. With a view to establishing the general form of the curve of the correlation coefficient, we notice the similarity and narrowness of the curves.

6.2.4 Length scales.

As it has been shown, we have found structures of less than 10mm in diameter clearly resolved for the PIV measurement of this particular flow. Similarly to the results for the experiment with grid turbulence in air, the achieved resolution is compared with the turbulent lengthscales for the flow. For the turbulent Reynolds number we find:

$$R_t = \frac{u' l_e}{\nu} = 76.81$$

Using the standard relationships, we find the Taylor's microscale λ and the Kolmogorov microscale η:

$$\lambda \simeq l_e \sqrt{15/R_t} \quad \Rightarrow \lambda \simeq 8.3mm$$

$$\eta \simeq \lambda (225 R_t)^{-1/4} \quad \Rightarrow \eta \simeq 0.7mm$$

Here we have, consistently with previous examples, chosen $l_e = M$, M being the gridspacing of the turbulence generating grid.
For this set of measurements and experimental set-up we find that it should be possible to resolve structures down to a size comparable to Taylors microscale, although it may be just on the limit of the size of individual structures that can be identified. Structures of a size comparable to the Kolmogorov microscale for this flow cannot be resolved.

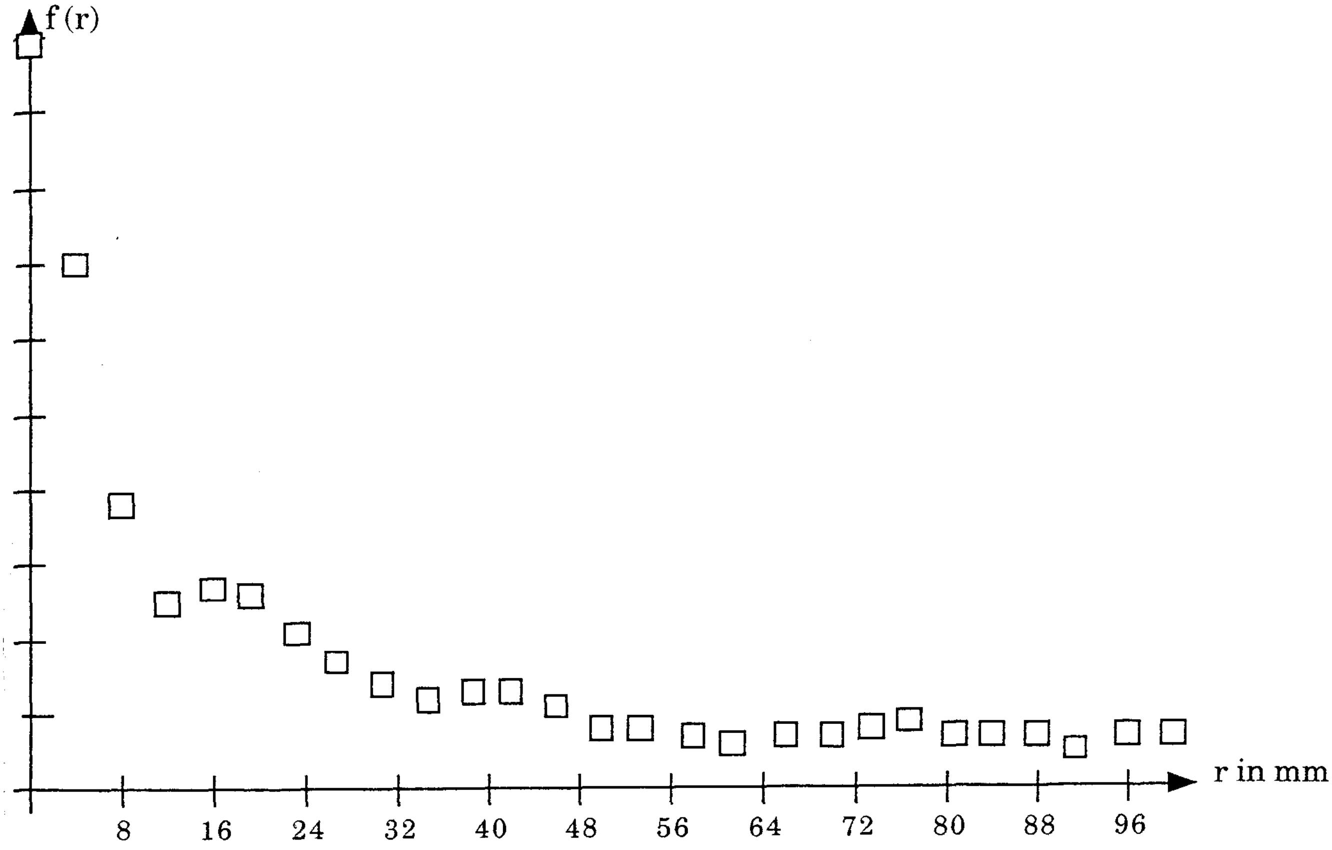

Figure 6.36: The longitudinal correlation function $f(r)$ for grid turbulence in air.

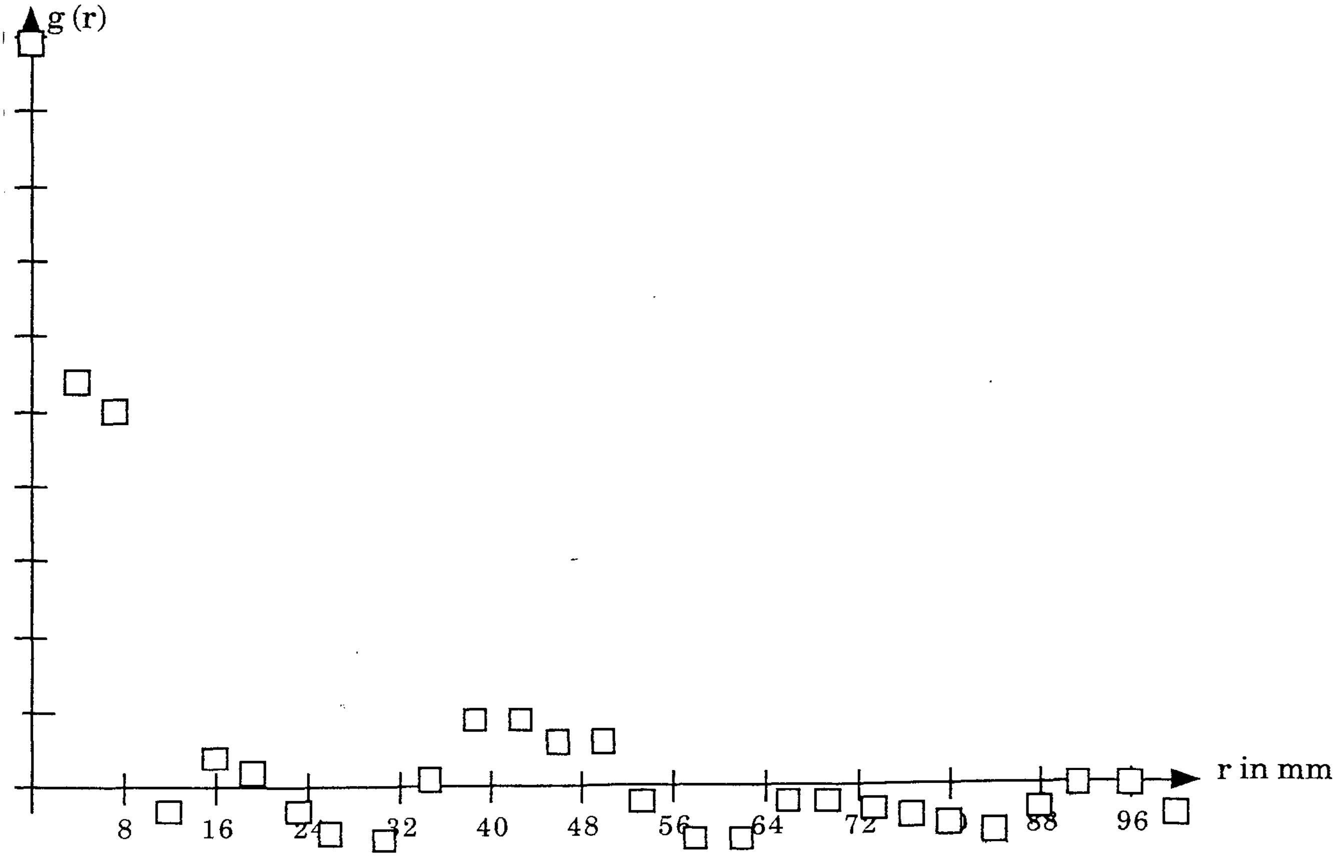

Figure 6.37: The transverse correlation function $g(r)$ for grid turbulence in air.

6.2.5 Coherent structures.

As for the previous example, we find that according to our intuitive "definition" of coherent structures, these are identifiable from the vorticity plots in Figure 6.29 to 6.35. Since we can now follow the temporal development of the flow it should be possible to more directly apply the method put forward by Mumford [62, 63]. Mumford introduces an algorithm that identifies certain structures and follow their development/evolution through the flow. This algorithm should (with slight modifications) be applicable to this type of flow measurement result. However, this is outside the scope of this thesis.

6.2.6 Verification of theoretical results.

As the conclusions from the measurement of grid-generated turbulence in air have suggested, it is important to consider the choice of integral lengthscale for the estimation of the normalized standard error very carefully. Accordingly we have chosen $2 \times M$, where M is the grid spacing of the turbulence generating grid, as a measure of the one-dimensional integral lengthscale L_1. We thus find:

$$L_1 = 37.5mm \quad L_2 = 1406mm^2$$

When considering the curves of the correlation functions $f(r)$ and $g(r)$ in Figure 6.36 and 6.37, we find that for $r = 37mm$, $f(r)$ has dropped to less than 20% of its original value. At this point the value for $g(r)$ is very close to zero, but we have to bear in mind that the curve for $g(r)$ is oscillating. It is, however, clear that for $r = 2 \times M$, $g(r)$ has decorrelated sufficiently for this to be a suitable choice for L_1 even for this dimension.

The overall rms turbulence level for this flow $\frac{\sigma}{\mu}$ was found to be:

$$\frac{\sigma}{\mu} = 0.0624 \simeq 6.2\%$$

It has to be noted, however, that this is calculated over an area of the flow that includes an area in close proximity to the turbulence generating grid.

By observation we must again conclude that the approximation for the curve of the correlation coefficient $K_u(\underline{r})$ must be the same as for the preceeding experimental set up, that is:

$$K_u(\eta, \nu) = e^{-\alpha^2(\eta^2+\nu^2)}$$

This is based on the similarity and narrowness of the curves. As we have seen, the curve for the transverse correlation coefficient $g(r)$ does oscillate slightly about the x-axis, not enough, however, to impose the restriction of a cosine term in the form for the correlation coefficient.

For the agreed approximation of the correlation curve, the simplified results for the error when estimating the mean and mean square value over a finite area $N_1 \times N_2$, were:

$$\boxed{\boldsymbol{K}_u(\boldsymbol{\eta},\boldsymbol{\nu}) = e^{-\alpha^2(\eta^3+\nu^2)}}$$

Mean value estimates

Small sampling areas: $\epsilon^2 = \frac{\sigma_u^2}{\mu_u^2}$

Large sampling areas: $\epsilon^2 = \frac{L_2}{N_1 N_2}\frac{\sigma_u^2}{\mu_u^2}$

Mean square estimates

Small sampling areas: $\epsilon^2 = \frac{2\left(1+\frac{2\mu_u^2}{\sigma_u^2}\right)}{\left(1+\frac{\mu_u^2}{\sigma_u^2}\right)^2}$

Large sampling areas. $\epsilon^2 = \frac{4L_2\left(1+\frac{4\mu_u^2}{\sigma_u^2}\right)}{N_1 N_2\left(1+\frac{\mu_u^2}{\sigma_u^2}\right)^2}$

The method employed when comparing the results from the theoretical predictions of the normalized standard error with the caculations from PIV results, is exactly the same as was described in section 6.1.7, the only difference being in the number of frames selected. For this series of measurements a total of 30 frames were selected, representing one 'run' of the camera, each covering an area of $35.000mm^2$ in the flow plane, resulting in a total area of $1070000mm^2$.
Table 6.3 and Figure 6.38 displays the normalized standard error ϵ, for mean value estimates over the area $N_1 \times N_2$, in a homogeneous near-isotropic turbulent flow regime with a two-dimensional integral lengthscale of $L_2 = 1406mm^2$.

Table 6.3 Mean value estimates for grid turbulence in water.

Sampling area $N_1 \times N_2$ (mm^2)	ϵ estimated from theory	ϵ calculated from PIV results
4438	0.070	0.039
8875	0.049	0.035
17750	0.035	0.034
26625	0.029	0.027
35500	0.025	0.027
44375	0.022	0.025
53250	0.020	0.024
62125	0.019	0.022
71000	0.018	0.023
79875	0.017	0.022
88750	0.016	0.021
97625	0.015	0.018
106500	0.014	0.022
177500	0.011	0.020
Small sampling areas $\epsilon = 0.062$		

Again we find reasonably good agreement between the theoretical predictions for ϵ, and the results calculated from PIV photographs. There results appears to be in agreement, particularly around a value of sampling area of $\approx 30.000mm^2$, corresponding to a frame. For larger sampling areas the value calculated from PIV results is largest, but, except for very small sampling areas, the difference is between 0.5 and 1 % in the value for ϵ.
From the theoretical predictions we find that a sampling area of $30.000mm^2$, corresponding to one analysed frame, results in a normalized standard error of less than 3%.

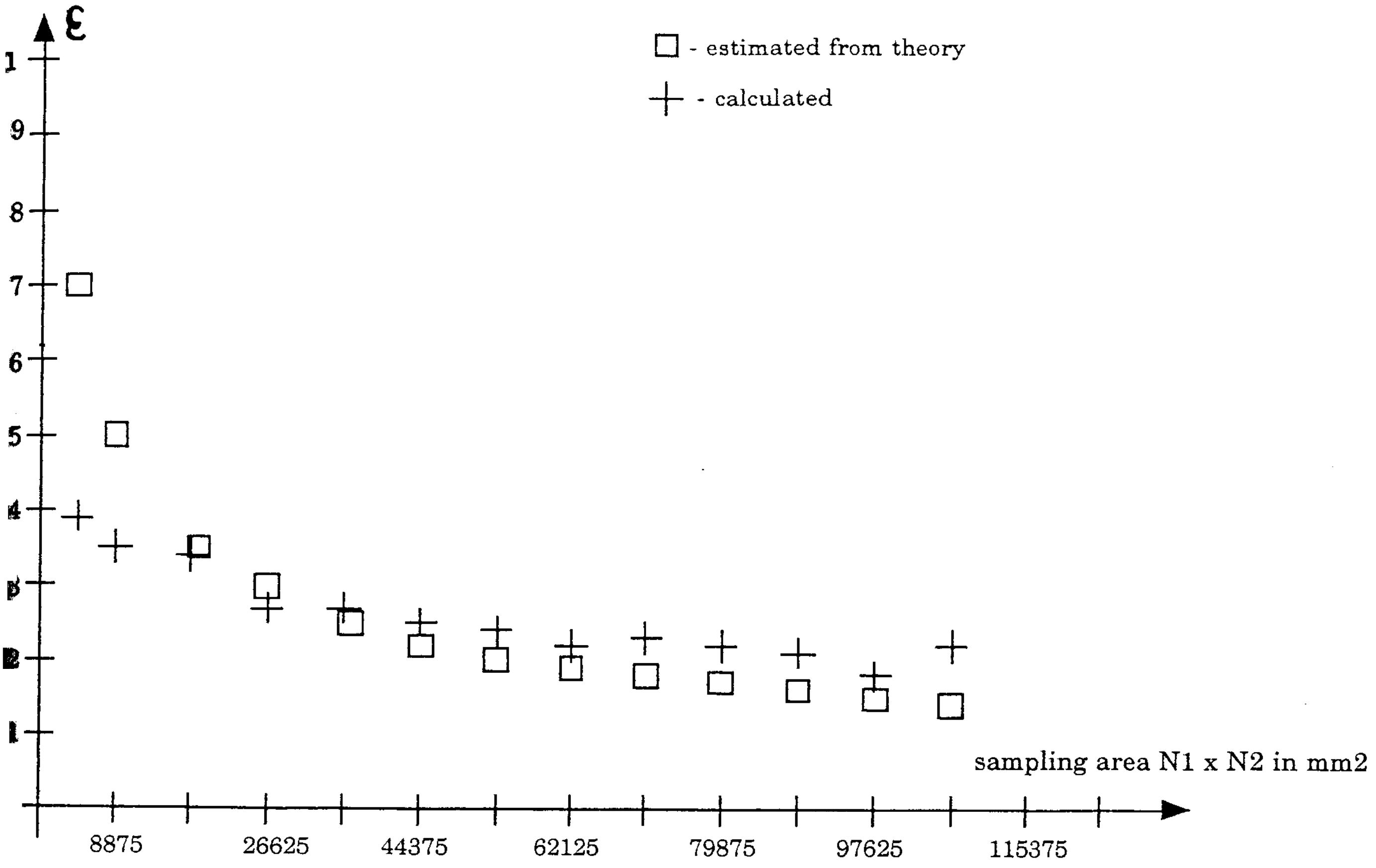

Figure 6.38: Mean value estimates for grid turbulence in water.

Table 6.4 and Figure 6.39 display the normalized standard error ϵ for mean square value estimates over the area $N_1 \times N_2$, for homogeneous near-isotropic grid turbulence in air with a two-dimensional integral lengthscale of $L_2 = 1406mm^2$. As for the results for the mean value estimates we find good agreement between the theoretically predicted values for ϵ, and those calculated from PIV results. The results differ maximally 1-1.5%. Similarly it is the theoretically predicted values that are the smaller. This is the opposite to what was found for the results from the measurements on grid turbulence in air. One of the causes of the larger calculated error could be that the flow was still in the initial phase, and thus not fully developed, when the measurement was performed. The theoretical predictions appear valid, and it is found that to achieve a normalized standard error of less than five percent we should sample over an area in the flow field of approximately $40.000mm^2$. For this experimental set-up that would correspond to slightly more than one frame.

Table 6.4 Mean square value estimates for grid turbulence in water.

Sampling area $N_1 \times N_2$ (mm^2)	ϵ estimated from theory	ϵ calculated from PIV results
8875	0.099	0.071
17750	0.070	0.069
26625	0.057	0.056
35500	0.050	0.053
44379	0.044	0.049
53250	0.040	0.045
62125	0.037	0.044
71000	0.035	0.045
79870	0.033	0.045
88750	0.031	0.045
97625	0.030	0.038
106500	0.029	0.044
177500	0.022	0.040
Small sampling areas $\epsilon = 0.124$		

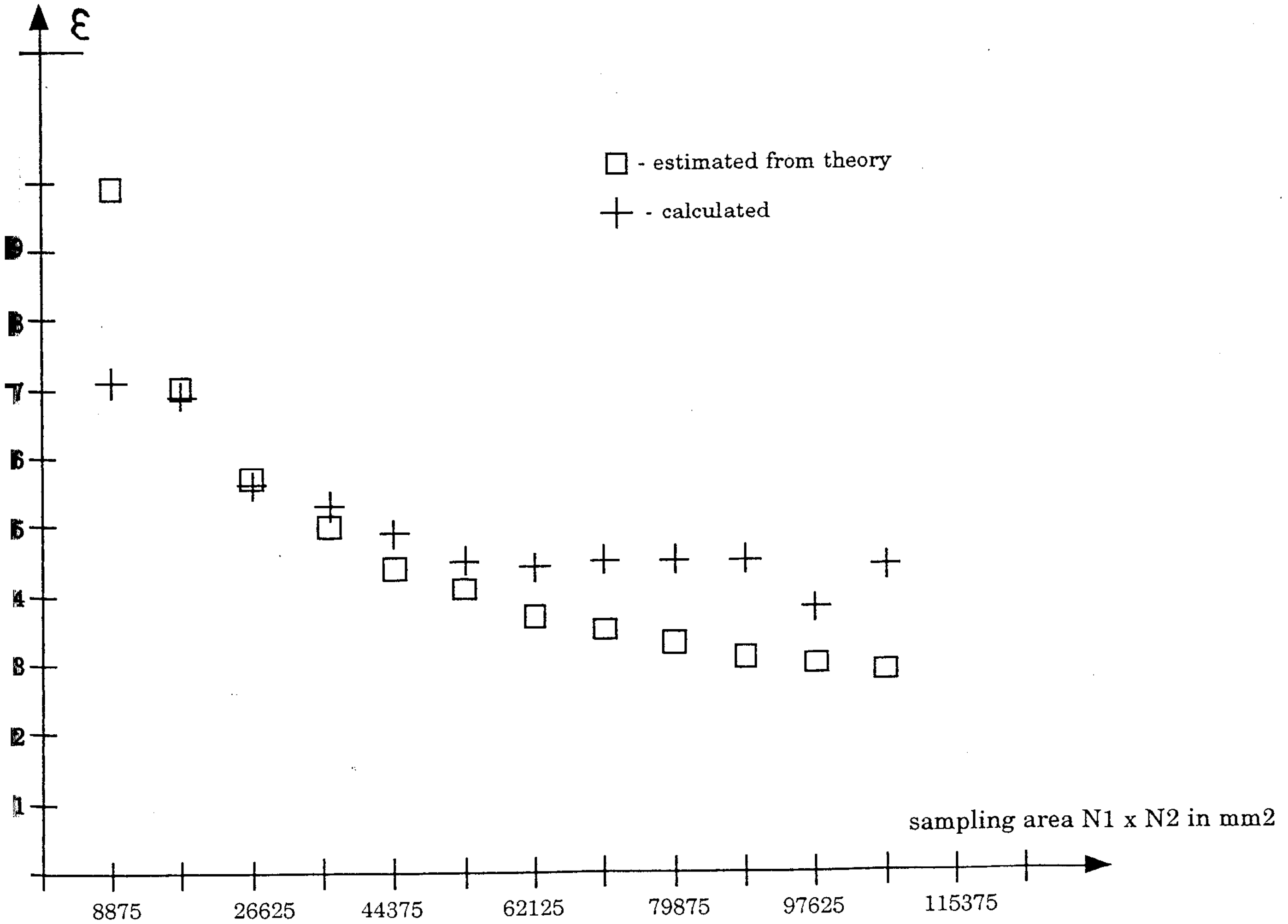

Figure 6.39: Mean square estimates for grid turbulence in water.

6.2.7 Conclusions.

PIV was succesfully applied to homogeneous, near-isotropic grid-generated turbulence in the initial phase, the flow medium being water. The resulting vector velocity and vorticity plots reveals the structure of the developing flow, where individual structures with a diameter of less than $10mm$ is clearly resolved, the size of these structures being comparable with Taylors lengthscale for the given flow. We can thus conclude that the resolution for this series of measurements is satisfactory in accordance with the results from the previous section.

The measurements were performed with a known time separation of the individual frames, and the temporal, as well as the spatial, development of the flow is clearly displayed in the consecutive plots. This is just further proof that PIV can provide views of several important aspects of the flow as well as the quantitative results.

The verification of the theoretical predictions of the error introduced when estimating the mean and mean square values over finite areas were performed on the results.

6.3 Discussion on the verification of theoretical predictions from experimental results.

In chapter 5, we introduced an estimate for the normalized standard error ϵ relative to sampling area, when calculating the maen and mean square values for homogeneous isotropic turbulence. In this chapter we have attempted to verify these predictions using results from PIV measurements of grid-generated turbulence in air and water.

From the derivation and subsequent analysis it is very clear that there are at least two important factors that need to be considered before attempting to use the given simplified forms of the error relative to sampling area. Firstly, it is imperative to ascertain the rms level of turbulence of the flow. This could be known in advance or measured as part of the set-up routine. It is the case that every PIV measurement does require some initial knowledge of the flow parameters, and the measurement of the rms turbulence level could easily be included here.

It is, however, slightly more complicated when it comes to establishing the correct value for the parameter we have termed the integral length scale L_1, L_2. This parameter is dependent on the correlationlength of the flow and also related to the values governing the behaviour of the curve of the correlation coefficient. For the above measurements and calculations, we have limited ourselves to homogeneous and near-isotropic grid-generated turbulence as this embraces the majority of the results from the theoretical predictions. A value of $2 \times M$, where M is the grid spacing of the turbulence-generating grid, was chosen as a suitable measure for L_1, and L_2 the square of this. The fact that this value actually does correspond to a distance where no significant correlation exists is in accordance with what could be concluded from the curve of the correlation coefficients $f(r)$ and $g(r)$. When considering the results presented it must be concluded that the above is a suitable choice for the integral length scale. Generally, as shown in Figure 6.40, it is found that for large sampling areas this choice for L_2 results in a theoretically predicted value for ϵ that differs by a value of less than 1-1$\frac{1}{2}$ % in ϵ from what was found in calculations from PIV results.

We can thus conclude that, given the rms turbulence level is known and a suitable choice for the integral lengthscale L_2 can be found, the theoretical predictions for the normalized standard error relative to sampling area are correct and in accordance with results from actual measurements and can be used when estimating the mean and mean square values from such measurements. For measurements on grid-generated homogeneous near-isotropic turbulence, a value of $2 \times M$ is generally a reasonable approximation to the one-dimensional integral lengthscale L_1, and that L_2 is taken as the square of this.

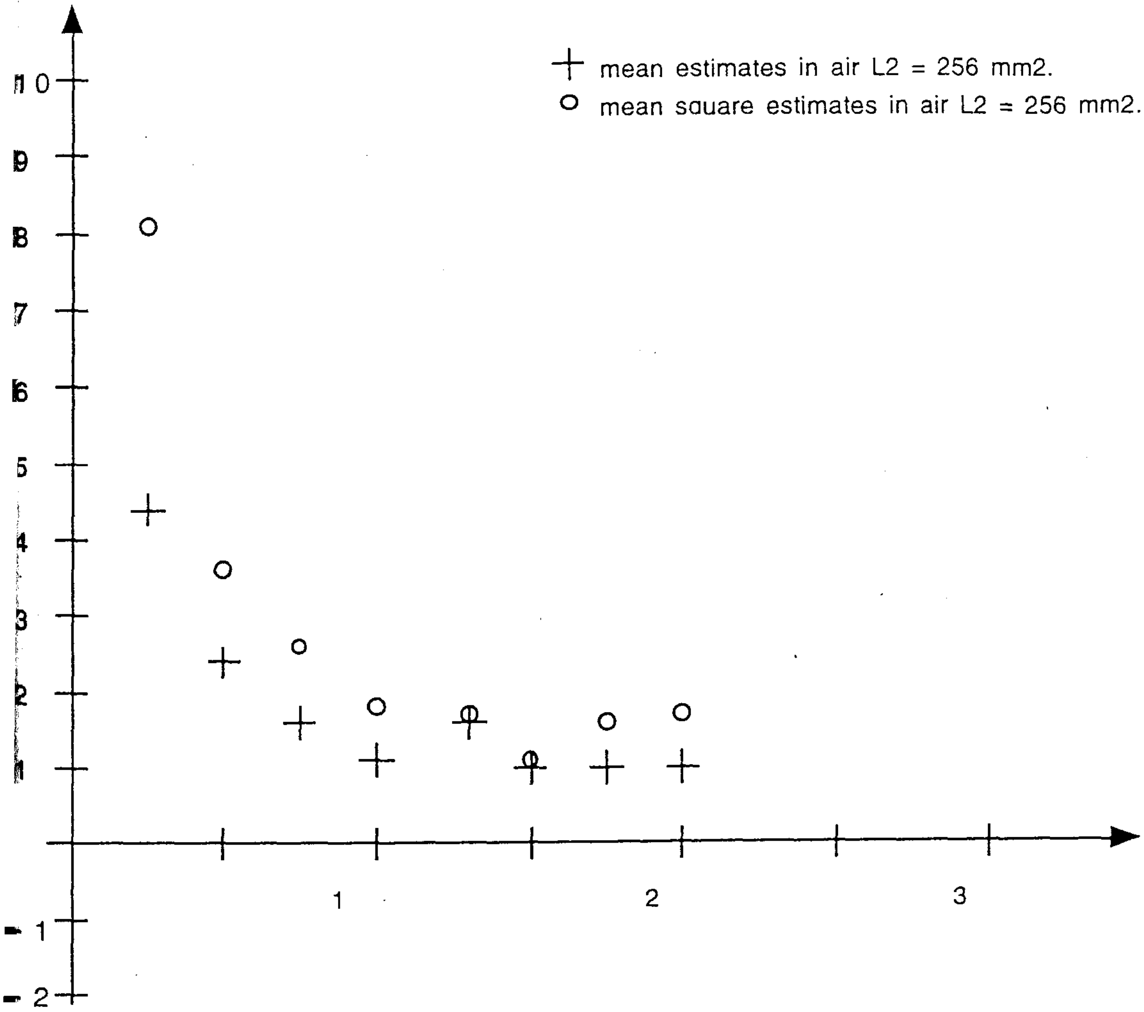

Figure 6.40: $\Delta\epsilon = |\epsilon_t - \epsilon_c|$

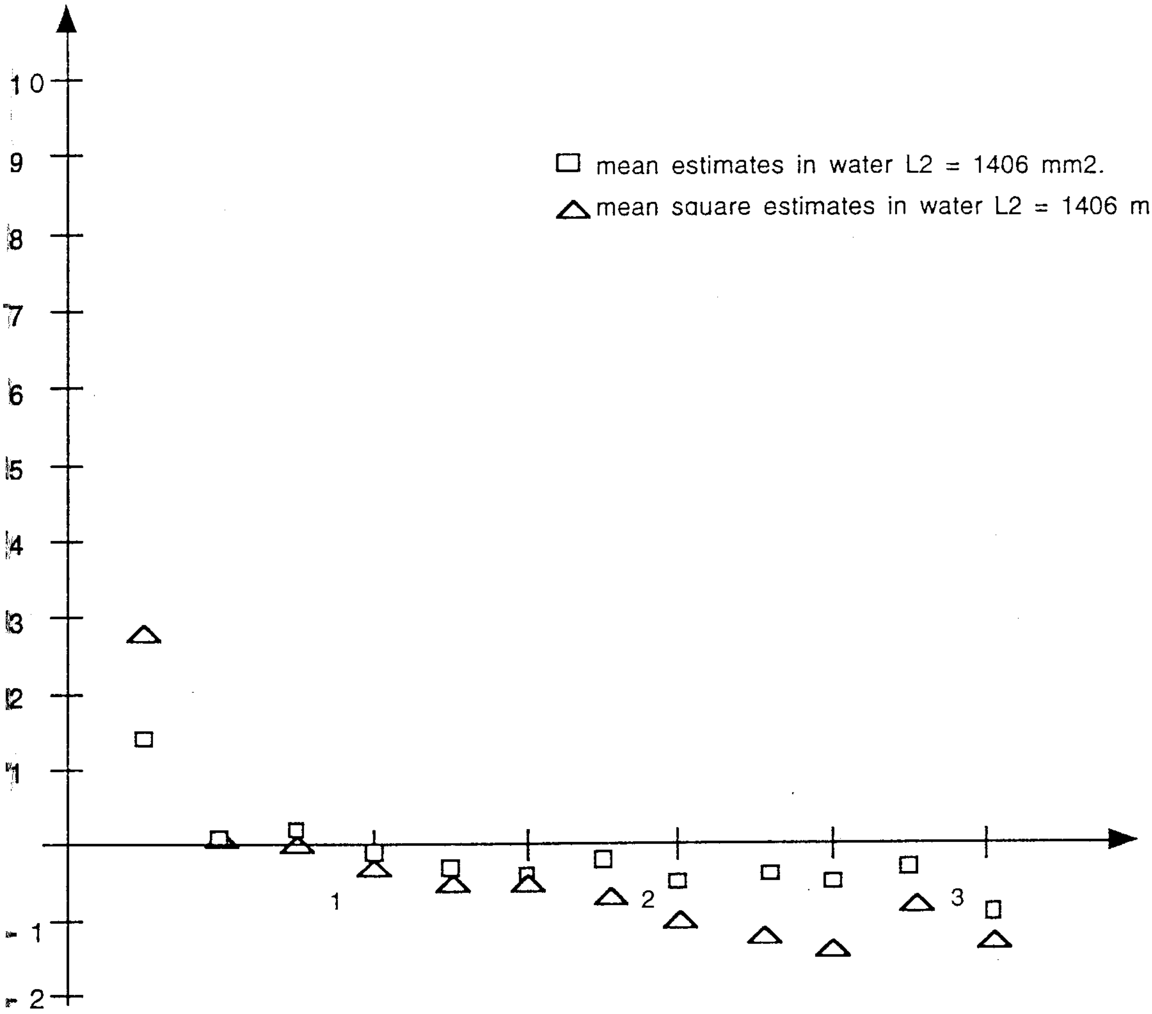

Figure 6.41: $\Delta\epsilon = (\epsilon_t - \epsilon_c)$

Chapter 7

Bibliography

1. Absil L.H.J. Laser Doppler measurements of mean turbulence quantities time-and spatial-correlation coefficients in the wake of a circular cylinder. *Proceedings of the 4th International Symposium on Applications of Laser anemometry to Fluid Mechanics* , Lisbon, 1988.

2. Adrian R.J. Scattering Particle Characteristics and their effect on pulsed laser measurements of fluid flow: speckle velocimetry vs particle image velocimetry. *Applied Optics vol. 23* , 1690-1691, 1984.

3. Adrian R.J. Optical Methods for Measuring Vector Velocity Fields I: Principles. *Lecture Series 1988-06*, von Karman Institute for Fluid Dynamics, 1988.

4. Adrian R.J. Double Exposure, Multiple-Field Particle Image Velocimetry for Turbulent Probability Density. *Optics and Lasers in Engineering vol.9*, 211-228, 1988.

5. Adrian R.J. Statistical properties of particle image velocimetry measurements in turbulent flows. *Laser Anemometry in Fluid Mechanics*, Instituto Superior Técnico, Lisbon, Portugal, 1988.

6. Adrian R.J. Engineering Applications of Particle Image Velocimeters. *L.I.A. vol. 68*, ICALEO, 1989.

7. Adrian R.J. and Yao C.S. Application of pulsed laser technique to liquid and gaseous flows and the scattering power of seed materials. *Proc. of the 2nd International Symposium on Applications of Laser Anemometry to Fluid Mechanics*, Lisbon, 1984.

8. Adrian R.J. and Yao C.S. Development of Pulsed Laser Velocimetry (PLV) for Measurement of Turbulent Flow. *Proc. Symposium on Turbulence, ed. X.B. Reed et.al.*, Missouri, 1984.

9. Arnold W., Hinsch D. and Mach D. Turbulence level measurement by speckle velocimetry. *Applied Optics vol.25, no.3*, 1986.

10. Arroyo M.P. et. al. Particle Image Velocimetry in Rayleigh-Bernard Convection: Photograohs with a high number of exposures. *Optics an Lasers in Engineering vol.9*, 295-317, 1988.

11. Batchelor G.K. An introduction to Fluid Dynamics. *Cambridge University Press*, 1970.

12. Batchelor G.K. The theory of homogeneous turbulence. Cambridge Science Classics,1986.

13. Batchelor G.K. and Townsend A.A. Decay of vorticity in isotropic turbulence. *Proc. Roy. Soc. A, 190*, 534-550, 1946.

14. Batchelor G.K. and Townsend A.A. Decay of isotropic turbulence in the initial period. *Proc. Roy. Soc. A, 193*, 539-558, 1948.

15. Bearman W.D. at.al. Particle Image Velocimetry applied to three-dimensional wake flows. *IMechE Symp. on Flow Mapping using Laset Techniques*, London, 1991.

16. Bendat J.S. and Piersol A.G. Measurement and analysis of randam data. *John Wiley and sons*, 1968.

17. Bruce T., Easson W.J., Elgaard C., Greated C.A. And McCluskey D.R. Applications of an automated PIV and post-processing system. *The EuroMech Colloquium 279*, Delft, The Netherlands, 1991.

18. Collicot S.H. Transition from Particle Image Velocimetry to Laser Speckle Velocimetry with increasing seeding density. *Proc. of the 6th International Symposium on Applications of Laser Techniques to Fluid Mechanics*, Lisbon, 1992.

19. Corrsin S. Turbulence: Experimental Methods. *Handbuch der Physik vol. II* , pp 524-555, Springer Verlag, 1963.

20. Coupland J.M. and Pickering C.J.D. Particle Image Velocimetry: Estimation of Measurement Confidence at Low Seeding Densities. *Optics and Lasers in Engineering vol.9*, 201-210, 1988.

21. Dryden H.L. A Review of the Statistical Theory of Turbulence. *Quat. Appl. Math. 1, 7*, 1943.

22. Dudderar T.D., Meynart R. and Simpkins P.G. Full-Field Laser Metrology for Fluid Velocity Measurement. *Optics and Lasers in Engineering vol.9*, 163-199, 1988.

23. Durrani T.S. and Greated C.A. Laser Systems in Flow Measurement. *Plenum*, New York, 1977.

24. Easson W.J. (ed.) Particle Image Velocimetry - A Practical Course. *UnivEd Technologies Ltd*, Scotland, 1993.

25. Economikos L et.al. Towards full field measurements of instantaneous visualizations of coherent structures in turbulent shear flows. *Experimental Heat Transfer, Fluid Mechanics, and Thernodynamics, ed. R.K.Shan et.al.*, Elsevier, 1988.

26. Edwards R.V. Some practical considerations of the resolution and accuracy of Particle Image Velocimetry *Private Communication.*

27. Edwards R.V. Is Laser Anemometry Perfectable? *Private Communication.*

28. Frenkel F.N., Klebanoff P.S. and Huang T.T. Grid turbulence in air and water. *Phys. Fluids* , 22(9), 1979.

29. Grant I. and Smith G.H. Modern developments in Particle Image Velocimetry. *Optics and Lasers in Engineering vol.9*, 245-264, 1988.

30. Grant I., Owens E.H. and Smith G.H. The Effect of Flow Turbulence and Interrogating Beam Profile on Particle Image Velocimetry Fringes. *Optics and Lasers in Engineering 11*, 115-128, 1989.

31. Grant I. and Owens E.H. Confidence interval estimates in PIV measurements of turbulent flows *Applied Optics vol.29, no.10* , 1400-1405, 1990.

32. Gray C. The development of particle image velocimetry for water wave studies. *Ph.D. Thesis*, Univ. of Edinburgh, 1989.

33. Gray.C and Greated C.A. The Application of Particle Image Velocimetry to the Study of Water Waves. *Optics and Lasers in Engineering vol.9*, 265-276, 1988.

34. Gray C. et.al. An analysis of the scanning beam PIV illumination system. *Meas. Sci. and Technology, vol.2, no.8*, 717-724, 1991

35. Guezennec Y.G. and Kiritsis N. Statistical Investigation of Errors in Particle Image Velocimetry. *Proc. Int. Soc. Optical Eng. vol 140, 4*, 128-138, 1990.

36. Guezennec Y.G. and Kiritsis N. Statistical investigation of errors in particle image velocimetry. *Experiments in Fluids, 10*, 138-146, 1990.

37. Hayes I.D. and Turner J.T. High speed on-line whole field processing of complex flows. *Proc. of the 6th International Symposium on Applications of Laser Techniques to Fluid Mechanics*, Lisbon, 1992.

38. Hecht E. and Zajac A. Optics. *Addison-Wesley*, 1973.

39. Hinze J.O. Turbulence. *McGraw-Hill*, 1965.

40. Hinze J.O. Turbulent fluid and particle interaction. *Progress in Heat and Mass Transfer, vol 6*, 433-452, 1972.

41. Hunter J.C. and Collins M.W. The processing of data from optical whole field measurement methods and large eddy simulation predictions to investigate coherent structures in fluid flow. *International Journal of Optoelectronics vol.5, no. 5* , 405-438, 1990.

42. Hunt J.C.R., Wray A.A. and Moin P. Eddies, Streams and Convergenze Zones in Turbulent Flows. *Proc. of Center for Turbulence Research Summer Program*, 1988.

43. Hunter J.C. et.al. The Large Eddy Structure of Turbulent Flows. *Heat and Technology vol.4, no. 1* , 1986.

44. Hussain A.K.M.F. Coherent structures-reality or myth. *Phys. Fluids vol.26, no. 10*, 1983.

45. Hussain A.K.M.F. Coherent structures and turbulence. *J. Fluid Mech. vol. 174*, 303-356, 1986.

46. Höcker R. and Kompenhans J. Application of Particle Image Velocimetry to Transonic Flows. *Proc. of the 5th International Symposium on Applications of Laser Anemometry to Fluid Mechanics* , Lisbon, 1990.

47. Keane R.D. and Adrian R.J. Optimization of Particle Image Velocimeters. *L.I.A. vol. 68* , ICALEO, 1989.

48. Keane R.D. and Adrian R.J. Optimization of Particle Image Velocimeters. Part I: Double Pulsed Systems. *Proc. of the 5th International Symposium on Application of Laser Techniques to Fluid Mechanics*, Lisbon, 1990.

49. Keane R.D. and Adrian R.J. Optimization of Particle Image Velocimeters. Part II: Multiple Pulsed Systems. *Meas. Sci. Technology. 2*, 963-974, 1991.

50. Kompenhans J. and Reichmuth J. 2-D Flow Field Measurements in Wind Tunnels by Means of Particle Image Velocimetry. *Presented at the 6th International Congress on Applications of Lasers and Electr-Optics*, San Diego, 1987.

51. Kompenhans J. and Höcker R. Investigation of turbulent flows by means of Particle Image Velocimetry. *5th International Symposium on Flow Visualization*, Prague, 1989.

52. Kuo A. Y.-S and Corrsin S. Experiments on internal intermittency and fine structure distribution functions in fully turbulent fluid. *J. Fluid. Mech. vol 50 II*, 285-319, 1971.

53. Landreth C.C. and Adrian R.J. Measurement and Refinement of Velocity Data Using High Image Density Analysis in Particle Image Velocimetry. *Proc. of the 4th International Symposium on the Application of Laser Anemometry to Fluid Mechanics*, Lisbon, 1988.

54. Liu Z.-C., Landreth C.C., Adrian R.J. and Hanratty T.J. High resolution measurement of turbulent structure in a channel with particle image velocimetry. *Experiments in Fluids 10* , 301-312, 1991.

55. Lourenco L.M. and Krothapalli A. Application of PIDV to the study of the temporal evolution of the flow past a circular cylinder. *Proceedings of the 3rd International Symposium on the Application of Laser Anemometry to Fluid Mechanics ed. D.F. Durao*, Instituto Superior Technico, Lisbon, 1986.

56. Lourenco L. and Krothpalli A. The role of photographic parameters in laser Speckle or particle image displacement velocimetry. *Experiments in Fluids vol.5* , 29-32, 1987.

57. McCluskey D.R. and Elgaard C. PIV investigations of rope dispersal and turbulence. *Scottish Fluid Dynamics Annual Meeting* , Edinburgh, 1990

58. McCluskey D.R. and Elgaard C. PIV investigations of turbulence and rope dispersal. *IMechE Symposium on Flow Field Diagnostics*, London, 1991.

59. McCluskey D.R. Report on An Investigation of Rope Dispersal. *Reprt Univ. of edinburgh*, 1991.

60. McCluskey D.R., Elgaard C., Easson W.J. and Greated C.A. The application of PIV to turbulent two-phase flows. *Flow visualization and image analysis ed. F.T.M. Nieuwstadt*, 1992.

61. McWilliams J.C. The Coherent Vortices of Two-dimensional and Geostrophic Turbulence. *Turbulence and Coherent Structures, ed. O.Metais and M.Lesiur*, Kluwer, 1989.

62. Mumford J.C. The structure of the large eddies in fully developed turbulent shear flows. Part 1. The plane jet. *J. Fluid Mech. vol. 118*, 241-268, 1981.

63. Mumford J.C. The structure of the large eddies in fully developed turbulent shear flows. Part 2. The plane wake. *J. Fluid Mech. vol. 137*, 447-456, 1983.

64. Perkins R.J., Ghosh S. and Phillips J.C. The Interaction Between Particles and Coherent Structures in a Plane Turbulent Jet. *Advances in Turbulence 3, ed. A.V. Johansson and P.H.Alfredsson*, Springer, Berlin, 1991.
65. Pickering C.J.D. and Halliwell N.A. Laser speckle photography and particle image velocimetry: photographic film noise. *Applied Optics vol.23, no.17* , 2961-2969, 1984.
66. Pickering C.J.D. and Halliwell N.A. Laseer Speckle Photography: Preprocessing of Fringe Pattern Data to Improve Dynamic Range. *The Journal of Photographic Science vol. 33*, 1985.
67. Prasad A.K. and Adrian R.J. Stereoscopic Particle Image Velocimetry Applied to Liquid Flows. *Proc. of the 6th International Symposium on Applications of Laser Techniques to Fluid Mechanics*, Lisbon, 1992.
68. Quinn P.A. et.al. A critical analysis of the Particle Image Velocimetry Technique as applied to Water waves. *Applied Scientific Research* , 1991.
69. Reuss D.L. et.al. Instantaneous Planar Measurements of Velocity and Large-Scale Vorticity and Strain Rate in an Engine Using Particle-Image Velocimetry. *SAE Technical Paper Series* , Detroit, 1989.
70. Reuss D.L. et.al. Velocity, Vorticity, and Strain-Rate Ahead of a Flame measured in an Engine Using Particle Image Velocimetry. *SAE Technical Paper Series*, Detroit, 1990.
71. Roberts J.B. and Surry D. Coherence of Grid-Generated Turbulence. *Journal of the Engineering Mechanics Division*, 1973.
72. Skyner D.J., Gray C. And Greated C.A. A comparison of time-stepping numerical predictions with whole field measurements in breaking waves. *Water wave kinematics ed. A.Tornu and O.T. Gudmestadt, Kluwer Academic Publishers*, 491-508, 1990.
73. Taylor G.I. Statistical Theory of Turbulence, Part I. *Proc. of the Royal Society A*, 421-44, 1935.
74. Taylor G.I. The Statistical Theory of Isotropic Turbulence. *Journal of the Aeronautical Sciences vol. 4*, 311-5, 1937.
75. Tennekes H. and Lumley J.L. A first course in turbulence. *MIT press*, 1973
76. Townsend A.A. The structure of turbulent shear flow. *Cambridge University Press*, 1976.
77. Tritton D.J. Physical Fluid Dynamics. *Van Nostrand Reinhold*, 1977.

78. Utami T. and Ueno T. Visualization and picture processing of turbulent flow. *Experiments in Fluids 2*, 25-32, 1984.

79. Utami T. and Ueno T. Experimental study on the coherent structures of turbulent open-channel flow using visualization and picture processing. *J.Fluid Mech. vol.174*, 399-440, 1987.

80. Vincent A. and Meneguzzi M. The spatial structure of homogeneous turbulence at Reynolds Numbers around 1000. *Turbulence and Coherent Structures ed. Mé tais O. and Lesieur M.* pp 191-201, Kluwer Academic Publishers, 1989.

81. Vincent A. and Meneguzzi M. The spatial structure and statistical properties of homogeneous turbulence. *J. Fluid. Mech. vol 225*, pp 1-20, 1990.

82. von Karman T. The fundamentals of the statistical theory of turbulence. *Journal of Aeronautical Science vol.4, no.4*, 1937.

83. Westerweel J. Digital Particle Image Velocimetry. Theory and application. *Ph.D. Thesis*, Delft University Press, 1993.

84. Westerweel J., Elgaard C. and Nieuwstadt F.T.M. Application of digital Particle Image Velocimetry to turbulent flows. *The EuroMech Colloquium 279* , Delft, The Netherlands, 1992.

85. Westerweel J. and Nieuwstadt F.T.M. Performance tests on 3-dimensional velocity measurements with a two-camera digital particle-image velocimeter. *4th Int. Conf. on Laser Anemometry* , Ohio, 1991.

86. Westerweel J. Flö r J.B. and Nieuwstadt F.T.M. Measurement of dynamics of coherent flow structures using particle image velocimetry. *Applications od Laser Techniques in Fluid Mechanics, ed. R.J. Adrian et.al.*, Springer, Berlin, 1992.

87. Westerweel J. et.al. Measurements with particle image velocimetry on fully developed turbulent pipe flow at low Reynolds number. *Proc. of the 6th International Symposium on Applications of Laser Techniques to Fluid Mechanics*, Lisbon, 1992.

Chapter 8

Appendix A

Report on methods to resolve directional ambiguity in PIV measurements.

Report on methods to resolve directional ambiguity in PIV measurements.

Charlotte Elgaard

December 1990

1 Introduction

Directional ambiguity is a fundamental problem inherent in the basic PIV and speckle technique. In the standard double pulsed technique there is no facility for determining the order of the images on the film. This results in an ambiguity in the velocity measurement of π, i. e. between $\vec{V}$ and $-\vec{V}$. If furthermore an analysis technique is employed where the two components of velocity is determined individually, e. g. the orthogonally compressed image technique, the ambiguity then exists for both components leading to a four-fold problem, i. e. between (u, v), $(u, -v)$, $(-u, v)$ and $(-u, -v)$. Until this dilemma has been resolved it is necessary, when the velocity information from a PIV negative is evaluated, to rely heavily on a-priori knowledge about the flow. This can often turn into guesswork even for just slightly complex flows.

This report lists and comments on the various existing and proposed methods for resolving the above problem. These methods have been divided into two major groups; Image Shifting and Particle Image Labelling.

The shift must be chosen with a priori knowledge about the flow in mind. The minimum shift required to remove the ambiguity is:

$$V_{shift} = V_{min} + V'_{max}$$

(Shift taken in +ve direction). Another limitation is, that if we require all the velocities in the range of interest to be measurable we must have:

$$V_{shift} + V'_{max} = (2V'_{max} + V_{min}) \leq V_{max}$$

The shifting velocity is usually chosen as small as possible.

2.3 Advantages and disadvantages.

There are several advantages with the image shifting technique, apart from the removal of the directional ambiguity.
Image shifting improves the dynamic range of the system. By introducing a shift it is possible to measure areas of very low velocity, that is velocities that would normally be smaller than V_{min}. Also if we have a flow with fluctuations around a mean, a negative shift can be introduced to reduce the mean, and allow the small scale structure to be investigated, either by larger magnification or longer time between exposures. A negative shift can also be used to compress the max. velocity in a flow, if this exceeds the maximum measurable, in a way such that this becomes measurable.
Image shifting can be employed in both the PIV (low seeding density), and the speckle (high seeding density) mode. Image shifting does not influence which method should be used to interrogate the negative.

Points to mention on the negative side are.
The image shifting will introduce an additional error into the velocity measurement. The size of this error depends on the chosen image shifting method.
To be able to choose the correct image shifting velocity V_{shift}, a certain amount of a priori knowledge about the flow under investigation is necessary. Similarly it is necessary , in order to obtain analysable PIV negatives from a flow, to have information about the range of velocities present in the flow.In addition to this the upper and lower bounds on this range, $-V'_{max}$, V'_{max} together with information about the resolution of the recording system and analysis system is required when image shifting is introduced. If these values are not given, or possible to estimate, it will be necessary to repeat the measurements, until they can be estimated, this may pose a problem with unsteady and complex flows.
The image shift may eliminate or enhance problems with nonlinearity in the scanning beam illumination system, depending on whether -ve or +ve V_{shift} is used.

2.5 Image shifting by rotating or oscillating mirror.

This method resembles the frequency shifting technique applied in LDA.
In this case the shift is introduced by recording the images through a rotating mirror. The mirror is positioned between the flow and the camera, which is mounted at a 90° viewing angle, the mirror is placed at an 45° angle to both the illuminated plane and the camera, see fig. 2.

FIG. 2.

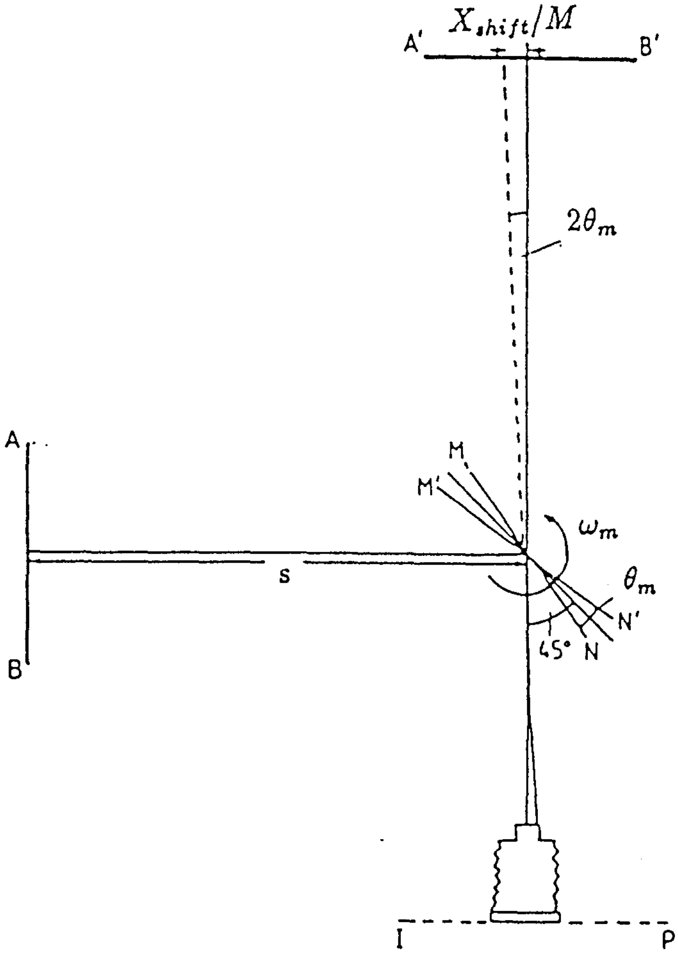

Fig. 2. (copied from ref. 1.) Experimental arrangement for the rotating mirror method. A'B' is the plane of the virtual objects as seen by the camera. MN is the mirror plane at first exposure, M'N' the mirror plane at second exposure, after the mirror has moved through an angle θ_m.

The distance between the mirror axis and the flowplane is usually given for any particular set up. Let ω_1 and ω_2 be the angular velocities in the direction of the mean and normal flow respectively. To obtain the required shift velocity in the two directions, we must have:

$$V_{s1} = 2\omega_1 s$$

$$V_{s2} = 2\omega_2 s$$

Also, we must have that:

$$\omega_m{}^2 = \omega_1{}^2 + \omega_2{}^2 = \frac{1}{4s^2}(V_{s1}{}^2 + V_{s2}{}^2)$$

and that the angle of inclination, α, can be found from:

$$\alpha = \tan^{-1}(\frac{\omega_2}{\omega_1}) = tan^{-1}(\frac{V_{s2}}{V_{s1}})$$

So for a given set up, and required 2-D shift, the velocity ω_m, and angle of inclination α can be calculated from the above.
This method is limited to shifts of up to 10 m/s c. f. ref.1-3. one possible error lies in the correct determination of the velocity of the mirror and hence the shift velocity, it should be possible to limit this error to 1% .
If the series of exposures is not taken with the mirror around the 45° position, loss of focus and errors will be introduced. Again this is a mechanical system, and it is external to the original system. It might however be possible to join the mirror onto the camera system.
The system is not entirely easy and simple to set up, but can easily be moved and used for different set ups.

References:

1. Grant, I. ; Smith, G. H. and Owens, E. H. :"A Directionally sensitive Particle Image Velocimeter",J. Phys. E. 21 (1988) 1190-1195.
2. Landreth, C. C. ; Adrian, R. J. and Yao, C. S. :"Double pulsed velocimeter with directional resolution for complex flows", Experiments in Fluids 6, 119-128(1988).
3. Adrian, R. J. :"Image shifting technique to resolve directional ambiguity in double-pulsed velocimetry", Applied Optics vol. 25 3855-3853(1988).
4. Gaulthier, V. and Riethmuller, M. L. :"Application of PIDV to complex flows: resolution of directional ambiguity", Von Karman Inst. for Fluid Dynamics lecture series 1988.

2.6.2 The image shifting system.

For this method a uniaxial birefringent crystal is placed in front of the camera lens. The plate is cut with its surface normal aligned parallel to the crystal's principal plane, and at an oblique angle θ to the crystal's optic axis, see fig. 5.

FIG. 5.

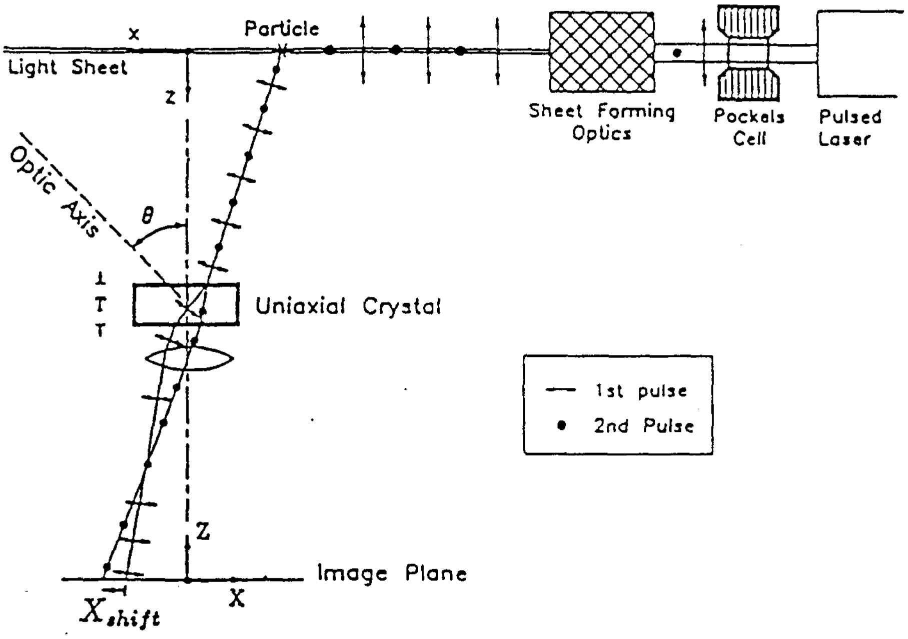

Fig. 5. (copied from ref. 1.) Experimental arrangement for electrooptical image shifting.

If the light scattered from the seeding particles in the flow is controlled in such a way that the first and second exposures consists of two linearly, but mutually orthogonally polarized pulses, we then have that the two particle images recorded on the film for any one seeding particle will be displaced by the true displacement X, plus a shift introduced by the crystal X_{shift}.
There exists standard methods to achieve the required linearly polarized light from one single laser, e. g. Pockels cells. Or alternatively, two orthogonally polarized laser could be employed.

2.6.3 Advantages and disadvantages.

The crystal will have to be cut with the angle θ between the optic axis and the surface normal, chosen in such a way as to ensure that the shift, X_{shift}, is as uniform as possible across the field of interest. Adrian quotes a value of $\theta = 53.38°$,

2.7 Other image shifting methods.

I. It has been suggested that it might be possible to move the film in the camera by a known amount between exposures. This would most likely entail using a special camera, but the image shifting device would then be an integrated part of the whole PIV system. This system would only give a one-dimensional shift, but the camera could be turned through 90° to give a shift in the y-direction if this was required.

II. It may be possible to use a spinning glass plate in front of the camera as an image shifting device. If the plate was turned at an angle θ between exposures, and this angle was assumed to be small, a shift in the filmplane of magnitude $X_{shift} = M d \omega_g t(1 - \frac{1}{n})$ would be introduced, where:
M = Magnification
d = Thickness of glass plate
ω_g = Constant angular velocity of glass
n = Refractive index of glass.
The light is assumed to propagate through air before hitting the plate.

This method would probably only work for small velocities around 1 m/s. Again it would be essential that the angle θ was small, and that the series of exposures are taken symmetrically around the direction of normal incidence. There might also be spurious reflections/refractions in the glass, which could lower the quality of the images on the film, but there should be negligible loss of intensity from traversing the plate.

III. Finally it has been suggested that a piezoelectric device could be used to translate the camera lens. Piezoelectric crystals expands along one axis and contracts along another when subjected to an electric field. This only gives small movements, but more is not required, and crystal oscillators are very stable.

3.3– Particle labelling by holographic image separation.

It is possible to record two separate holograms on one holographic plate. If the two images are recorded with mutually orthogonal reference beams, it will be possible to separate the two images on reconstruction, and thus determine the order of these.

Image plane holography is used as opposed to conventional Fresnel holography. With Fresnel holography it is necessary to use a reference beam for reconstruction, which is identical to the one used when recording the images. In image plane holography, the holographic film/plate is placed in the actual plane where the images are formed, and if the reference beam used for recording is correctly collimated, there is not the same restriction on the reference beam on reconstruction as for Fresnel holograms.

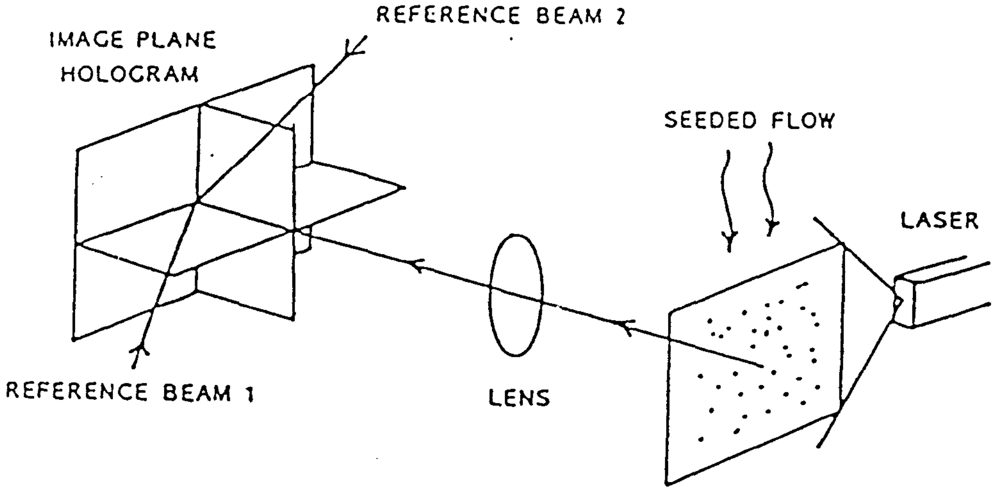

Fig. 6. (copied from ref. 1.) Experimental arrangement for the holographic image separation method.

The set up is as in fig. 6, here the planes defined by the object beam and first and second reference beams are mutually orthogonal. The first exposure is taken with reference beam 1, and the second with reference beam 2. The subsequent reconstruction with beam 1 and 2 respectively will give the required separation of the images. That is, if the hologram is reconstructed using beam 1, the images from the first exposure will be reconstructed, and if reference beam 2 is used, the images from the second exposure will be reconstructed. The velocity information can thus be evaluated by cross-correlation techniques.

3.4 Particle image labelling by different colours.

Here the particle images are labelled by using different colours for different exposures. This can be achieved in various ways. If a scanning beam system is used, it should be possible to coat the faces of the scanning mirror so that they would reflect only light of a certain wavelength. Consequetive faces could be differently coated to achieve the desired effect. The perhaps simplest way of getting different colours for different exposures would be to employ two lasers of different wavelengths. One laser whose output consists of different wavelengths(within a narrow band), can be used with an etalon, or simply a spinning filter in front. The resulting PIV negative can be separated into two colour fields by filtering, and the velocity information found by cross-correlation.

3.4.1 Advantages and disadvantages.

One of the main disadvantages with this method must be with the analysis method. That is, that the negative will have to be postprocessed split into two different fields, and as before mentioned cross-correlated, for which an automatic analysissystem yet has to be developed. If it is possible to analyse colour negatives in the standard way this may be performed and the direction inferred from the negative, although this could turn out to be very cumbersome. This technique can be used for both speckle and PIV.

Again, if the scanning beam system is employed, care must be taken to phase it correctly. There is a possibility of problems arising from lack of light intensity if the output from a single laser is used, and the resolution of the colour film may also have to be considered.

Multiple exposures are only limited by the number of wavelengths available. The different wavelenghts must of course be separated enough for the film to record them as different. This method would be transferable.